Hybrid system : from nanoparticles to gels

Zhihua Zhao

Zhihua Zhao. Hybrid system : from nanoparticles to gels. Coordination chemistry. Université Paul Sabatier - Toulouse III, 2017. English. NNT : 2017TOU30118 . tel-01887630

THÈSE

En vue de l'obtention du

DOCTORAT DE L'UNIVERSITÉ DE TOULOUSE

Délivré par :

Université Toulouse 3 Paul Sabatier (UT3 Paul Sabatier)

Si vous êtes en cotutelle internationale, remplissez ce champs en notant : Cotutelle internationale avec "nom de l'établissement", sinon effacer ce texte pour qu'il n'apparaisse pas à l'impression

---

Présentée et soutenue par :
Zhihua Zhao

le vendredi 15 septembre 2017

Titre :

Systèmes hybrides: de la nanoparticule aux gels

École doctorale et discipline ou spécialité :
ED SDM : Chimie organométallique de coordination - CO 043

Unité de recherche :
Laboratoire de Chimie de Coordination, LCC-CNRS, UPR 8241 & Laboratoire des IMRCP, UMR 5623

Directeur/trice(s) de Thèse :
Dr. Myrtil Kahn
Dr. Christophe Mingotaud

Jury :

Corinne Chanéac, Professeur, Université Pierre et Marie Curie, Paris (Rapportrice)
Rabah Boukherroub, Directeur de Recherche, Université de Lille, Lille (Rapporteur)
Fabienne Gauffre, Directeur de Recherche, Université de Rennes 1, Rennes (Examinatrice)
Romuald Poteau, Professeur, INSA Toulouse, Toulouse (Examinateur)
Myrtil Kahn, Directeur de Recherche, Université de Toulouse
Christophe Mingotaud, Directeur de Recherche, Université de Toulouse

Acknowledgements

I would like to thank all the members of my jury: Prof. Corinne Chanéac, Dr. Rabah Boukherroub, Dr. Fabienne Gauffre and Prof. Romuald Poteau for accepting to read the manuscript and examine my Ph.D work.

I would like to give my deep appreciation to my supervisors Dr. Myrtil Kahn and Dr. Christophe Mingotaud for giving me the opportunity to study in Toulouse, and for their endless guidance, patience, support and encouragement. Their rigorous academic attitude, innovative thinking, and profound knowledge of chemistry have left me a deep impression and will benefit me in my whole lifetime. I also would like to thank their kind-hearted help when I face some difficulties in my life beyond the research. And, I would like to thank Dr. Jean-Daniel Marty and Dr. Clément Roux, who also participate in this work and help me a lot during all these three years.

I would like to thank Dr. Pierre Fau who helped me a lot to measure the electronic properties. I would also like to thank Dr. Yannick Coppel for NMR experiments and fruitful discussions, many thanks for your patience to teach me even I had never used NMR before I came here. I also would like to thank Dr. Juliette Fitremann for her help to analyze the rheological and mechanical properties; Dr. Christine Lepetit for the molecular simulations and valuable discussions; Pierre Lecante for the WAXS experiments; Pierre Alphonse for the BET measurements; Jérome Esvan for the XPS measurements; Laure Vendier for the PXRD measurements; Vincent Collière for the high resolution electronic microscopy characterization; Stéphanie Seyrac for TGA characterization; Stéphane Gineste for the help to synthesize the ligand with azobenzene group; and all the others who indeed help me finish my PhD work.

All current and former Equipe T members in LCC and Equipe IDeAS members in IMRCP, Yohan Champouret, Pauline Loxq, Emillie Tailhades, Justyna Jonca, Jérémy Cure, Glenna Drisko, Zhiqin Zheng, Hala Assi, Guillaume Garnide, Ségolene

Palussière, Maxime Puyo, Xuming Zhang, Florian Wodlei, Baptiste Amouroux, Cherles-Louis Serpentini, Dr. Anne-Francoise Mingotaud, Dr. Christophe Coudret, and Dr. Katia Fajerwerg for their fruitful discussions and friendship.

Thanks to the help from some of my friends in Toulouse: Jinhui Wang, Chongwei Zhu, Longai Lang, Qian Liao, Lin Yang, Changlong Wang, Chen Zhang, Jieru Qiu, Liang Chen, Fan Li and Yin Zhang who have brought me a lot of fun during the 3 years.

Many thanks to all LCC and IMRCP employees for their kind-hearted help.

China Scholarship Council (CSC) and CNRS are also acknowledged for financial support.

The last but not the least, my greatest appreciation are dedicated to my parents Quangen Zhao and Hong Yue, my sister Xinmei, and my lovely daughter Sixuan and my wife Xiaoqi, who sacrificed much during these 3 years.

Systémes hybrides : de la nanoparticule aux gels

Zhihua Zhao

15/09/2017

Dedicated to my wife, Xiaoqi, and to my daughter, Sixuan.

Chapitre I - Revue bibliographique et objectifs de la thèse

Chapitre II – Analyse statistique d'objets anisotropes

Chapitre III – Une vision nouvelle sur la croissance de nanoparticules anisotropes de ZnO

Chapitre IV – Une vision nouvelle sur la croissance de nanoparticules anisotropes de ZnO

Partie expérimentale

Chapitre I

Revue bibliographique et objectifs de la thèse

Résumé

Dans ce chapitre introductif, nous nous attachons à présenter une introduction aux nanosciences en nous focalisant sur les nanoparticules d'oxydes métalliques qui sont au cœur de ce travail de thèse. Nous présentons les différentes méthodes de préparation de ces nanoparticules d'oxydes métallique en détaillant plus précisément l'approche « sol-gel » et l'approche organométallique. Cette dernière est en effet la méthode que nous avons utilisée tout au long de ce travail. Les travaux antérieurs à ce travail sont ensuite présentés afin de bien identifier les objectifs de cette thèse.

Contenu

Introduction

In this chapter, firstly I will discuss some basic concepts about the different kinds of nanoparticles (NPs). Then the discussion will be shifted to the metal oxide NPs and the versatile synthesis methods to get them, especially the organometallic chemistry strategy. The past published work in our group will then be shown in this chapter, and among them, the importance of the ligand effect on the different properties will be emphasized. At last, the project objectives of my thesis will be derivatized from those discussions.

I. 1. Nanoparticles

I. 1. 1 General Introduction of Nanoscience

Nanoscience involve studying and working with matter on an ultra-small scale. One nanometer is one-millionth of a millimeter, and a single human hair is around 80000 nanometers in width. Nanoscience encompass a range of techniques rather than a single discipline, and stretch across the whole spectrum of science, touching medicine, physics, engineering and chemistry [1]. They have huge application potential in different fileds such as new energy production, healthcare, communication and information technologies, environment protection and the preparation of new materials with better mechanical properties. Therefore, it becomes more and more important to develop in-depth study to better understand this discipline. In fact, the actual investment for nanomaterials and nanostructures occupies 49% in the investment for the study of nanoscience [2]. Now, in order to improve the national competitive ability in the scientific and technological fields, the motivation for the study of nanomaterials and nanostructures becomes mainly National Strategy Requirements. Furthermore, the study of nanomaterials and nanostructures is of vital importance for establishing new methods, new technologies and new principles, thereby potentially leading to breakthroughs in great scientific problems [3]. At the same time, the nanomaterial market is also a native power for the development of nanomaterials and nanostructures. Recently there has been substantial interest in the preparation and characterization of materials consisting of particles with dimensions in the metal oxide nanocrystalline materials [4]. One factor driving the current interest in nanoparticle research is the perceived need for further miniaturization of both optical and electronic devices [5,6].

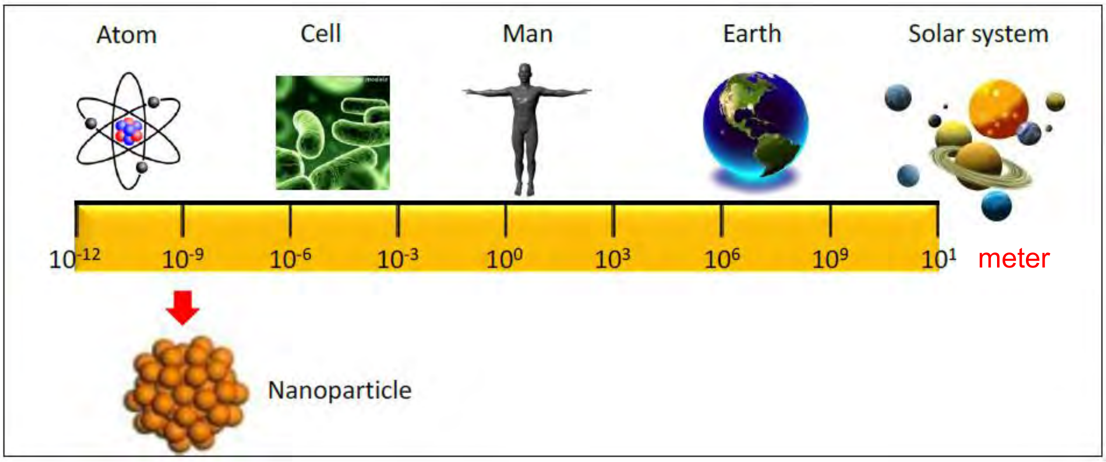

Figure I. 1. Diagram illustrating the scale of nanomaterials [7].

I. 1. 2 Meal Oxide Nanoparticles

Metal oxides play a significant role in the various areas of chemistry, physics, and materials science. Metallic elements can form a large diversity of oxide compounds, which can adopt a vast number of structural geometries with electronic structures that can exhibit metallic, semiconductor, or insulator character [8]. In technological applications, metal oxide nanoparticles are used in the fabrication of microelectronic circuits, sensors, piezoelectric devices, fuel cells, coatings for the passivation of surfaces against corrosion, and as catalysts [8]. For example, among them, a lot of works about zinc oxide, tin oxide and iron oxide nanoparticles have been done due to their interesting properties paving the ways for fascinating applications.

Zinc oxide is a material with great potential for a variety of practical applications, such as piezoelectric transducers, optical waveguides, surface acoustic wave devices, varistors, phosphors, transparent conductive oxides, chemical and gas sensors, spin functional devices, and UV-light emitters [9-12]. Its wide bandgap (≈3.37 eV at room temperature) makes ZnO a promising material for photonic applications in the UV or blue spectral range, while the high exciton-binding energy (60 meV) allows efficient excitonic emission even at room temperature. In addition, ZnO doped with transition metals shows great promise for spintronic applications. It has also been suggested that ZnO exhibits sensitivity to various gas species, namely ethanol (C_2H_5OH), acetylene (C_2H_2), and carbon monoxide (CO), which makes it suitable for sensing applications [13-15]. Moreover, its piezoelectric property (originating from its non-centrosymmetric structure) makes it suitable for electromechanical sensor or actuator applications [16-18]. Also, ZnO is biocompatible which makes it suitable for biomedical applications [19-21]. Consequently, there is considerable interest in studying ZnO in the form of powders, single crystals, thin films, or nanostructures [22].

Tin oxide is another important metal oxide semiconductor, which is considered to be technologically important materials and has been investigated for a wide range of applications such as high energy density rechargeable lithium batteries [23], storage of solar energy [24], gas sensors [25], electrocatalysis [26] and photocatalysis [27]. This diversity in the application is a function of the size, morphology, phase, and crystallinity of the nanocrystals. Various geometrical morphologies of tin oxide have been produced, for example, spherical particles [28], networks of ribbons [29], hollow microspheres [30], sheets [31], flowers [32] and belts [33]. SnO_2 sensor response is because of the physical and chemical changes on its surface due to the adsorption of a chemical stimulant and the sensitivity can be fine-tuned by reducing the size up to nano dimensions, varying the crystal structure and morphology and/or adding dopants (typically noble metals and other metal oxides) to create nanocomposite materials [34].

Iron oxide is also a kind of important metal oxide material, which has served humans for centuries, for example, the application of small iron oxide nanoparticles as a contrast agent for *in vivo* diagnostics has been practiced for nearly half century [35]. In the past decade, the synthesis of magnetic iron oxide nanoparticles has been intensively developed not only for its fundamental scientific interest but also for its many technological applications, such as targeted drug delivery, magnetic resonance imaging (MRI), magnetic hyperthermia and thermoablation, bioseparation, and biosensing [36]. Eight iron oxides are known [37], among these iron oxides, hematite (α-Fe_2O_3), magnetite (Fe_3O_4) and maghemite (γ-Fe_2O_3) are very promising and popular candidates due to their polymorphism involving temperature-induced phase transition. Each of these three iron oxides has unique biochemical, magnetic, catalytic, and other properties which provide suitability for specific technical and biomedical applications.

I. 2. Synthesis of Metal Oxide Nanoparticles

In the past decades, a number of specific methods have been developed to prepare metal oxide nanoparticles, some examples about the broadly used methods will be discussed as follow: (1) Coprecipitation methods: This involves dissolving a salt precursor (chloride, nitrate, etc.) in water (or other solvent) to precipitate the hydroxide form with the help of a base. Very often, control of size and chemical homogeneity in the case of mixed-metal oxides is difficult to achieve [38]. (2) Microemulsion technique: Microemulsion or direct/inverse micelles represent an approach based on the formation of micro-/nano-reaction vessels under a ternary mixture containing water, a surfactant, and oil. Metal precursors on water precede precipitation as hydroxides within the aqueous droplets, typically leading to monodispersed materials with size limited by the surfactant-hydroxide contact [39]. (3) Solvothermal methods: In this case, metal complexes are decomposed thermically either by boiling in an inert atmosphere or by using an autoclave with the help of pressure. A suitable surfactant agent is usually added to the reaction media to control particle size growth and limit agglomeration [40]. (4) Template/surface derivatized methods: Template techniques are common to some of the previously mentioned methods and use two types of tools: soft templates (surfactants [41]) and hard templates (porous solids as carbon [42] or silica [43]). Template- and surface-mediated nanoparticle precursors have been used to synthesize self-assembly systems [44]. (5) Chemical vapor deposition (CVD) and pulsed laser deposition (PLD) [45]. The main advantages of those 2 methodologies are that they produce uniform and pure nanoparticles and films, however, the disadvantage of these methods is that they require a careful initial setting up of the experimental parameters [46]. Besides the above mentioned methods, there are other two important methods, which are sol-gel route and organometallic method for which detailed introduction will be described in the following.

I. 3. Sol-gel route towards Metal Oxide Nanoparticles

The sol-gel method prepares metal oxides *via* hydrolysis of precursors, usually metal alcoxides in alcoholic solution, resulting in the corresponding hydroxides. Condensation of molecules by giving off water leads to the formation of a network of the metal hydroxide: hydroxyl species undergo polymerization by condensation and form a dense porous gel. Appropriate drying and calcination lead to ultrafine porous oxides [47].

The sol-gel route offers some particular advantages, centered on the ability to produce a solid-state material from a chemically homogeneous precursor. By ensuring atomic level mixing of reagents, one should be able to produce complex inorganic materials such as ternary and quaternary oxides. Furthermore, sol-gel chemistry should enable greater control over particle morphology and size. In reality, producing a homogeneous precursor at room temperature does not ensure homogeneity throughout a reaction and many sol-gel routes have therefore been designed to combat or control phase segregation during synthesis. In fact, some of the most interesting advances in the sol-gel field in recent years have come from gels that have some degree of ordering and structure [48].

However, the sol-gel process is mainly restricted in aqueous condition, which brought some major limitations forward when it came to the preparation of their nanoscale counterparts. Aqueous sol-gel chemistry is rather complex, mainly due to the high reactivity of the metal oxide precursors and the double role of water as ligand and solvent. In many cases, the three reaction types (hydrolysis, condensation, and aggregation) occur almost simultaneously (and are difficult to control individually), so slight changes in experimental conditions result in altered particle morphologies, a serious issue regarding the reproducibility of a synthesis protocol. Furthermore, the as-synthesized metal oxides are often amorphous, and it is difficult to retain full control over the crystallization process during any additional annealing step. All these parameters might be controlled well enough for the preparation of bulk metal oxides, however, they represent a big challenge in the case of nanoparticle synthesis [49].

Therefore, it is of importance to develop nonaqueous sol-gel processes in organic solvents under exclusion of water, which are able to overcome some of the limitations. The advantages of nonaqueous sol-gel processes are closely related to the manifold role of the organic components in the reaction mixture. They not only act as the oxygen-supplying agent for the metal oxide but also strongly influence particle size, shape, surface and assembly properties, and, in selected cases, even composition and crystal structure. Furthermore, in contrast to aqueous systems with nearly indefinable composition, the characterization of the organic compounds in organic media can easily be performed with standard techniques like nuclear magnetic resonance (NMR) spectroscopy or gas chromatography-mass spectrometry (GC-MS). By retro-synthetical analysis, it is possible to correlate the processes leading to these organic species to the growth mechanisms of the oxide nanoparticles, offering a powerful tool toward the development of a rational synthesis strategy for a broad family of inorganic nanomaterials [49].

I. 4. Organometallic Method towards Metal Oxide NPs

There are many precursors for making metal oxide nanoparticles, and all the compounds could be classified as two categories: (a) inorganic metal salts including metal nitrate, metal chloride, metal acetate and so on; (b) organic metal compound, such as metal isopropoxide, or some other organometallic complex like alkyl metal. As with all synthesis procedures, each of the precursors described above has its characteristic scope and limitations. Many rely on the reactions of low-energy reagents at high temperatures, especially for those about inorganic metal salts, and for the other extreme, so called organometallic method, is a pathway involving the reaction of intrinsically higher energy organometallic complex at lower temperature.

In the literature, some results about the metal oxide nanoparticles prepared by organometallic pathway have been reported. For instance, Steigerwald et al. reported a new synthesis of TiO_2 nanocrystals that is based on the gentle oxidation of Bis(cyclooctatetraene)titanium ($Ti(COT)_2$), which is a very reactive organometallic complex [50]. Lewiński and co-workers [51-58] developed an organometallic method to prepare ZnO nanoparticles using diethylzinc ($ZnEt_2$) and its derived organometallic complex as precursor. For example, they used the $ZnEt_2$ as the precursor and carboxyl acid as stabilized ligand to obtain ZnO nanocrystals (Figure I. 2) and at last they successfully prepared photoactive Langmuir-Blodgett, freely suspended and free standing films of carboxylate ligand [54].

Figure I. 2. One-pot synthesis procedure for the preparation of ZnO nanocrystals coated by the carboxylate ligands [55].

Sabastian Polarz and co-workers [59-83] developed another organometallic precursor (alkylzincalkoxides with heterocubane architecture) to ZnO materials. A large variety of the tetrameric compounds $[RZnOR']_4$ had been prepared from the reaction of ZnR_2 with the respective alcohol in high yield, and then were reacted to ZnO either by thermal reaction or the reaction with water (Figure I. 3).

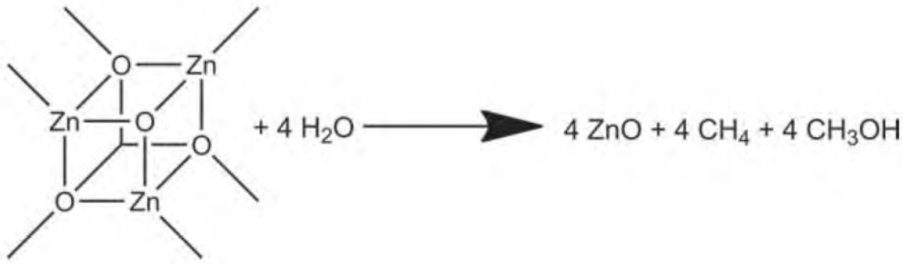

Figure I. 3. The reaction of a Zn_4O_4 heterocubane with water to yield ZnO [68].

Another work reported by Charlotte K. Williams is about the ZnO nanocrystals prepared by hydrolysis of zinc clusters, which obtained by the reaction of $ZnEt_2$ and phosphinate ligands. They found that the ligand is sequestered to a stable zinc cluster during the majority of the synthesis and only becomes coordinated to the nanoparticle surface, this interesting finding provide an understanding of the role of well-defined molecular precursors during the synthesis of small nanoparticles [84].

In fact, a lot of organometallic precursors have been chosen as the precursor to prepare metal oxide nanoparticles. Compared to the other method such as aqueous sol-gel process, this process has some advantages, for instance, normally the organometallic species could be dissolved in organic solvent, and thus the kinetic of the chemical reaction could be monitored by the chemical characterization tools like NMR spectra, furthermore, many of them have high energy, which could make the release of the metal atom in a relatively mild condition, for example, when mixed with the stabilizing ligands, some organometallic complex is very easy to be hydrolyzed just by simply expose to the air, and finally well-defined metal oxide NPs were obtained. However, there are also some disadvantages like relatively high price, and sometimes the organometallic complex is too reactive for the formation of the nanoparticles.

I. 5. The works of our group in LCC

I. 5.1. General introduction

In our group, we also use the highly energetic organometallic complexes, which are sensitive to both air and water, as the precursor, and the metal oxide nanoparticles could be obtained by direct hydrolysis or by another strategy, which involves two steps: the first step is hydrogenolysis of the organometallic complex in solution to get metal NPs, and then use some methods to oxidize the metal NPs to obtain metal oxide NPs. The shape and size of these nanoparticles can be controlled by the different parameters of the system (such as the nature of the organometallic precursor, the ligands or surfactants present, the solvent used and so on) [85].

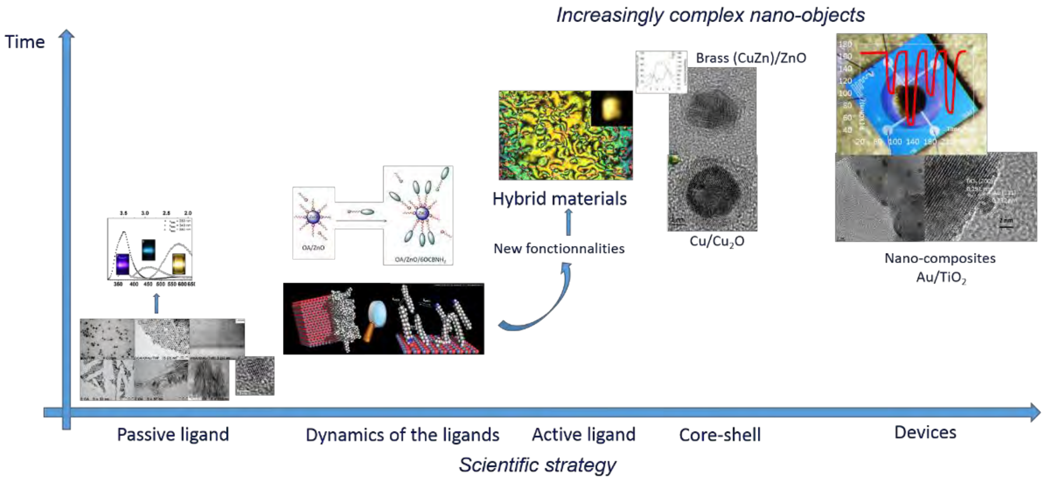

Figure I. 4. Schematic illustration for the scientific strategy in our group.

There is a strong correlation between the size and shape and properties of those NPs, and in our group, we use the NMR spectroscopy to monitor the dynamics of the stabilizing ligands like alkyl amine and (or) alkyl acids [94]. Some stabilizing ligands with special functional groups were synthesized and used either by direct coordination on the surface of the NPs or by an interesting method called ligand exchange, then the organic-inorganic hybrid materials with new functionalities like liquid crystal property could be prepared [98]. We also prepared some more complex nano-objects which have two or more metal species, and used them to make devices for the application of electronics like gas sensors [99]. In summary, the scientific strategy in our group could be depicted in figure I. 4, and several kinds of metal oxide NPs prepared in our group will be shown in the following content.

I. 5.2. The effect of stabilizing ligands on the prepared NPs

The first example is about the synthesis of ZnO NPs, which have been prepared by hydrolysis of $[Zn(C_6H_{11})_2]$ ($[ZnCy_2]$) in the presence of different kind of stabilizing ligands (figure I.5) [86-101]. Interestingly, when the synthesis was performed in solvent and the alkyl amine or (and) alkyl acid was (were) chosen as ligands, the isotropic ZnO nanoparticles could be obtained, however, when the synthesis was performed without any solvent, the anisotropic nanoparticles could be prepared just by exposure to the air (figure I.6). The size and shape of the ZnO NPs could strongly affect the properties like optical property [108] and gas sensitivities [110].

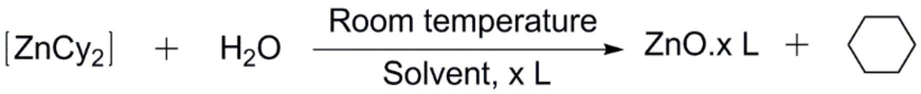

Figure I. 5. Schematic illustration for the preparation process of ZnO nanoparticles using pioneered by Kahn et al. [87].

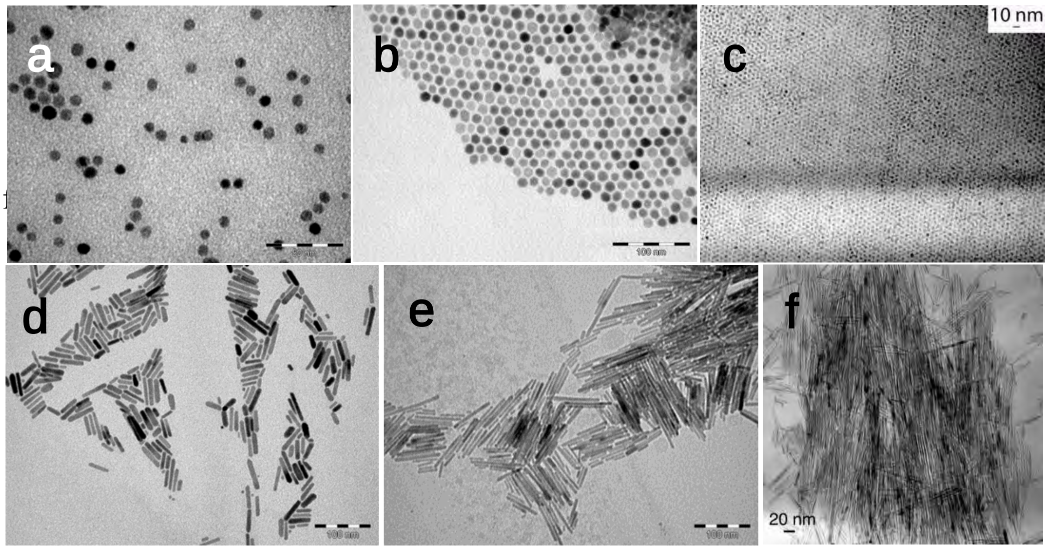

Figure I. 6. Representative TEM images of the ZnO nanoparticles prepared by the process depicted in figure I. 5: the isotropic ZnO NPs stabilized by 1 eq. OA (a), 1 eq. DDA and 1 eq. OlAc (b), 1 eq. HDA and 1 eq. OlAc (c) in THF; the anisotropic ZnO NPs stabilized by 5 eq. OA (d), 2 eq. OA (e), and 1 eq. OA (f) in the absence of solvents.

Furthermore, there is also correlation between the solubility and the stabilizing ligands. For example, if commercially available amino-PEG oligomers were used as the ligands, metal and metal oxide NPs including ZnO NPs could be obtained by hydrolysis of the organometallic complex, and those NPs could be solubilized in many non-polar and polar solvent including water [77, 89].

The stabilizing ligands are also very important for the self-organization property of the colloidal ZnO nanoparticles. For example, after gradually changing the concentration of the ZnO colloidal solution by evaporation of the solvent, no organization phenomenon could be monitored if long-alkyl-chain amines or carboxylic acids are used as stabilizing ligands, some superlattices of organized ZnO nanoparticles could be observed by TEM and SEM as well as by DLS when binary mixtures of long-alkyl-chain amines or carboxylic acids are used [114]. The coordination mode of the ligands at the surface of ZnO nanoparticles was fully characterized by different NMR technologies, which suggest that at least three different modes of interaction of the amines at the surface of the NPs. The first mode corresponded to a strong interaction between a small amount of amine and the NPs. The second mode corresponded to a weak interaction between the amines and the surface of the ZnO NPs. The third, and weakest mode of the interaction corresponded to the formation of a second ligand shell by the amine around the NPs that held together through van der Waals interactions [94, 115].

There are also some effects of the stabilizing ligands on the optical properties of the ZnO nanoparticles. For example, ZnO NPs were firstly prepared using alkyl-chain amine as the stabilizing ligand, after that, alkyl-chain thiol was added through a ligand exchange pathway. Interestingly, the emission wavelength of the ZnO NPs was not affected by the type of ligand at the surface of the NPs, however, the emission was reduced significantly after only 0.2 equiv. (with respect to the amine ligand) of thiol ligand was added [103]. Another work finished in our group is about the photocontrol of luminescent of ZnO NPs through an organic molecular switch, dithienylethene (DTE). It is very interesting that both isomeric forms of the DTE switch could quench the emission of ZnO NPs, and the efficiency of the closed isomer was ten times higher than the open one [112]. The above works did in our group pave the way to the application for optical sensors.

The second kind of metal oxide NPs prepared in our group is tin oxide NPs. We used the organometallic compound $[Sn(NMe_2)_2]_2$ as the precursor because of the relative thermodynamic weakness of the Sn-N bond, and tin/tin oxide nanoparticles could be obtained after a decomposition reaction by thermolysis in the organic solvent with water, and after an oxidation process, pure SnO_2 nanoparticles could be obtained [118-122]. Furthermore, when the alkyl amine like HDA (hexadecylamine, $CH_3(CH_2)_{15}NH_2$) was chosen as the stabilizing ligand, the particles with special morphology like octahedra could be obtained, PXRD confirmed the $Sn_3O_2(OH)_2$ structure prepared at room temperature, and SnO_2 structure could be prepared at last after calcination at 450 °C [123]. The above prepared nano- or micro- particles are very sensitive to reducing gases like CO, therefore those materials had been developed to high sensitive gas sensors [123].

The third example in our group is about the iron oxide NPs, organometallic compound $[Fe\{N(SiMe_3)_2\}_2]_2$ was chosen as the precursor and ultra-small iron oxide NPs could be obtained by a hydrolysis reaction in the organic solvent. In fact, the crystalline phase of the NPs could be adjusted by different oxidation process, for instance, exposed to the air or pure oxygen. And, the size of the iron oxide NPs was different if the alkyl amine with different length of alkyl chain was used as the stabilizing ligand [124]. Furthermore, polyacrylic acid (PAA) was used to trigger the iron oxide NPs to aggregate, which was water-biocompatible, and those prepared aggregates could be used in the field of magnetic resonance imaging[124-127].

In summary, the stabilizing ligands play a crucial role throughout the preparation of the material, and they can also have strong effects on the physical and chemical properties of the final nanoobjects. In fact, some stabilizing ligands can also play another role, for instance, as a functional part in the NPs hybrid materials.

I. 5.3. Hybrid materials

In the past decades, the hybrid materials attract more and more attention since they could combine different properties from different compositions in the matrix. In our group, the main efforts had been made to design hybrid materials based on metal oxide nanoparticles. The organic part in those hybrid materials could be introduced either by direct coordination on the surface of the NPs as the stabilizing ligands or by a simple ligand exchange process. For example, long alkyl amine was evidenced to be a good stabilizing ligand for the ZnO NPs, so some other kinds of stabilizing ligands with amine group could be synthesized and used to play the same role, therefore interesting functional group with specific properties like liquid crystalline property could be introduced in those designed ligands and at last become a part of the well-tailored hybrid materials [97]. In our group, some works about ZnO NPs liquid crystalline hybrid materials had been published [7, 95-101]. The first example [96] published is about $6OCBNH_2$/ZnO/OA hybrid material, which was prepared by a ligand exchange process between an amine-containing mesogenic liquid crystalline, $6OCBNH_2$ and octylamine (OA)-protected ZnO NPs (Figure I. 7).

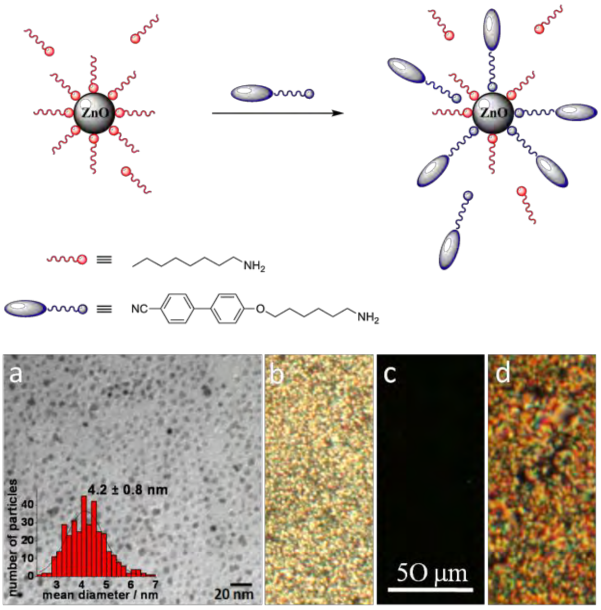

Figure I. 7. Schematic diagram of the proposed ligand exchange mechanism occurring in solution. TEM micrograph (a) and POM images of the hybrid (b) at 80 °C, (c) 140 °C and (d) cooling down to 84 °C [98].

The prepared hybrid material present mesomorphic behavior even for a high content of inorganic material. In combination with promising luminescent properties, it may be exploited for electro-optical applications.

The liquid crystal macromolecules could also be directly used as the stabilizing agents for the synthesis of ZnO NPs in solution [100-101]. Interactions between [Zn(Cy)$_2$] and the branched structure (through amine groups) were evidenced both by experiments in solution and by solid state ^{13}C-NMR studies in the LC state. Under isotropic conditions, hydrolysis of the [Zn(Cy)$_2$] precursor led to isotropic NPs. More precisely, the pure branched LC and hyperbranched LC are isotropic at 30 °C and 45 °C, respectively. When the experiments were performed in the nematic phase state of the LC compound (*i.e.* at lower temperatures), anisotropic ZnO structures, were obtained. As shown in Figure I. 8, either nano-worm-like or nano-wires structures were grown in branched LC and hyperbranched LC. They have an average width of 2.5(0.2) nm and 2.7(0.4) nm, respectively. Polydispersed lengths vary from a few nanometers up to around 100 nm when the branched LC was used, while lengths from around 10 to 200 nm were obtained when the hyperbranched LC was used. Thus, a direct correlation between the structural characteristics of the LC and the morphology of the nanostructures, was demonstrated. The new LC/NPs composites present, at the same time, LC properties and optical properties originating from ZnO [98].

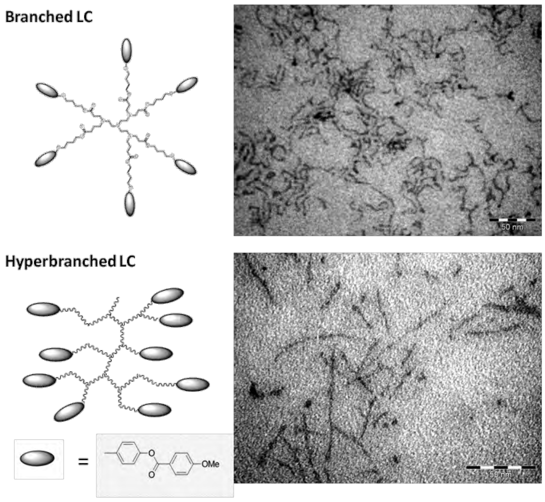

Figure I. 8. TEM micrographs of ZnO NPs synthesized under various conditions: (A) in branched LC at 30°C (scale: 200 nm) or at 5°C (scale: 50 nm) (B) in hyperbranched LC at 45°C (scale: 50 nm) or at 5°C (scale: 50 nm) [98].

All of the above synthesizes had been done in the presence of solvents, and we recently found that a kind of ZnO NPs/liquid crystal hybrid materials could also be prepared in the absence of solvents. A mixture of hexadecylamine (HDA) and $[ZnCy_2]$ (in a ratio of 2 equivalents of amine per zinc precursor) was chosen without additional solvent, whereas both are solids at room temperature, admixture of $[ZnCy_2]$ and HDA (in the 1:2 molar ratio) under an inert atmosphere rapidly leads to a liquid phase due to an acid-base reaction. After hydrolysis the mixture for 3 days, ZnO NPs hybrid materials with liquid crystal and luminescent properties could be obtained. More interestingly, the reaction temperature could strongly affect the anisotropy of the resulted NPs in the hybrid matrix [107].

I. 6. Project objectives

The initial objective of this project is to control and understand the growth process of ZnO NPs prepared through the simple organometallic pathway developed in our group, especially the anisotropic growth in the absence of any solvent. To reach this goal, an interesting 2-D plot analysis was developed. The formation of gels was evidenced and link between the gelification process and the size and shape of the NPs highligthened. Finally, new strategy toward processable and reshapable metal oxide hybrid materials was developped paving the way to a new generation of sensors.

References

[1]. A. Henglein, *Chem. Rev.* **1989**, 89, 1861–1873.

[2]. S. Suresh, Nanosci. Nanotechno. **2013**, 3, 62-74.

[3]. M. L. Steigerwald, L. E. Brus, *Acc. Chem. Res.* **1990**, 23, 183-188.

[4]. M. G. Bawendi, M. L. Steigerwald, L. E. Brus, *Annu. Rev. Phy. Chem.* **1990**, 41, 477-496.

[5]. A. P. Alivisatos, *J. Phys. Chem.* **1996**, 100, 13226-13239.

[6]. J. A. Stroscio, D. M. Eigler, *Science* **1991**, 254, 1319-1326.

[7]. S. Saliba, Université de Toulouse **2011**.

[8]. M. Fernández-García, J. A. Rodriguez, Metal oxide nanoparticles, *Encyclopedia of Inorganic and Bioinorganic Chemistry* **2011**.

[9]. H. C. Ong, T. G. Du, *J. Cryst. Growth* **2004**, 265, 471-175.

[10]. R. B. Lauer, *J. Phys. Chem. Solids* **1973**, 34, 249-253.

[11]. Z. Feng, R. Jia, B. Dou, H. Li, Z. Jin, X. Liu, F. Li, W. Zhang, C. Wu, *Sol. Energy* **2015**, 115, 770-776.

[12]. S. Pearton, F. Ren, *Int. Mater. Rev.* **2014**, 59, 61-83.

[13]. M.C. Carotta, A. Cervi, V. di Natale, S. Gherardi, A. Giberti, V. Guidi, D. Puzzovio, B. Vendemiati, G. Martinelli, M. Sacerdoti, D. Calestani, A. Zappettini, M. Zha, L. Zanotti, *Sens. Actuators B* **2009**, 137, 164-169.

[14]. Y. Zhang, J. Xu, Q. Xiang, H. Li, Q. Pan, P. Xu, *J. Phys. Chem. C* **2009**, 113, 3430-3435.

[15]. J. Xu, Q. Pan, Y. Shun, Z. Tian, *Sens. Actuators B* **2000**, 66, 277-279.

[16]. S. C. Minne, S. R. Manalis, and C. F. Quate, *Appl. Phys. Lett.* **1995**, 67, 3918.

[17]. X, Wen, Y. Fang, Q. Pang, C. Yang, J. Wang, W. Ge, K. S. Wong, S. Yang, *J. Phys. Chem. B* **2005**, 109, 15303–15308.

[18]. T. Shibata, K. Unno, E. Makino, Y. Ito, S. Shimada, *Sens. Actuators A* **2002**, 102, 106-113.

[19]. M. Ul-Islam, W. A. Khattak, M. W. Ullah, A. Kahn, J. K. Park, *Cellulose* **2014**,

21, 433-447.

[20]. J. Zhou, N. S. Xu, Z. L. Wang, *Adv. Mater.* **2006**, 18, 2432-2335.

[21]. H. Xiong, Y. Xu, Q. Ren, Y. Xia, *J. Am. Chem. Soc.* **2008**, 130, 7522–7523.

[22]. A. B. Djurisic, Y. H. Leung, *Small* **2006**, 2, 944-961.

[23]. Y. Idota, T. Kubota, A. Matsufuji, Y. Maekawa, T. Miyasaka, *Science* **1997**, 276, 1395-1397.

[24]. G. Hodes, L. Thompson, J. DuBow, K. Rajeshwar, *J. Am. Chem. Soc.* **1983**, 105, 324–330.

[25]. A. Kolmakov, Y. Zhang, G. Cheng, M. Moskovts, *Adv. Mater.* **2003**, 15, 997-1000.

[26]. W. Du, Q. Wang, D. Saxner, N. A. Deskins, D. Su, J. E. Krzanowski, A. I. Frenkel, X. Teng, *J. Am. Chem. Soc.* **2011**, 133, 15172–15183.

[27]. G. Wang, W. Lu, J. Li, J. Choi, Y. Jeong, S.Y. Choi, J.B. Park, M. K. Ryu, K. Lee, *Small* **2006**, 2, 1436-1439.

[28]. R. Demir-Cakan, Y. Hu, M. Antonietti, J. Maier, M. Titirici, *Chem. Mater.* **2008**, 20, 1227.

[29]. Z. Wang, Z. Pan, *Adv. Mater.* **2002**, 14, 1029.

[30]. H. Yang, J. Qian, Z. Chen, X. Ai, Y. Cao, *J. Phys. Chem. C.* **2007**, 111, 14067.

[31]. J. Liu, Y. Wan, F. Meng, X. Huang, J. Liu, *J. Mater. Chem.* **2012**, 22, 2885.

[32]. A. Chen, X. Penng, K. Koczkur, B. Miller, *Chem. Commun.* **2004**, 1964.

[33]. S. Sun, G. Meng, Y. Wang, T. Gao, M. Zhang, Y. Tian, X. Peng, L. Zhang, *Appl. Phys. A*, **2003**, 76, 287.

[34]. D. Mohanta, M. Ahmaruzzaman, *RSC Adv.* **2016**, 6, 110996-111015.

[35]. W. Wu, Q. He, C. Jiang, *Nanoscale Res. Lett.* **2008**, 3, 397.

[36]. N. Lee, T. Hyeon, *Chem. Soc. Rev.* **2012**, 41, 2575.

[37]. W. Wu, Z. Wu, T. Yu, C. Jiang, W. S. Kim, Sci. Technol. *Adv. Mater.* **2015**, 16, 023501.

[38]. K. S. Suslick, S. B. Choe, A. A. Cichowlas, and M. W. Geenstaff, *Nature*, **1991**, 353, 414.

[39]. V. Uskokovick and M. Drofenik, *Surf. Rev. Lett.*, **2005**, 12, 239.

[40]. M. Rajamathi, R. Seshadri, *Curr. Opin. Solid State Mater. Sci.* **2002**, 6, 337-345.

[41]. N. R. Jana, L. Gearheart, C. J. Murphy. *Adv. Mater.* **2001**, 13, 1389.

[42]. M. A. Correa-Duarte, N. Sobal, L. M. Liz-Marzán, M. Giersig, *Adv. Mater.* **2004**, 16, 2179-2184.

[43]. T. A. Crowley, K. J. Ziegler, D. M. Lyons, D. Erts, H. Olin, M. A. Morris, J. D. Holmes, *Chem. Mater.* **2003**, 15, 3518-2522.

[44]. Y. Yin, Y. Lu, B. Gates, Y. Xia, *J. Am. Chem. Soc.* **2001**, 123, 8718–8729.

[45]. J. Ohring, 'The Material Science of Thin Films', Academic Press, San Diego, **1992**.

[46]. M. Fernández-García, J. A. Rodriguez, **2011**. Metal Oxide Nanoparticles. *Encyclopedia of Inorganic and Bioinorganic Chemistry*.

[47]. L. V. Interrante and M. J. Hampen-Smith, 'Chemistry of Advanced Materials: An Overview', While-VCH, New York, **1998**.

[48]. A. E. Danks, S. R. Hall, and Z. Schnepp, *Mater. Horizon.* **2016**, 3, 91-112.

[49]. M. Niederberger, *Acc. Chem. Res.* **2007**, 40, 793-800.

[50]. J. Tang, F. Redl, Y. Zhu, T. Siegrist, L. E. Brus, and M. L. Steigerwald, *Nano Lett.* **2005**, 5(3), 543-548.

[51]. A. Grala, M. Wolska-Pietkiewicz, W. Danowski, Z. Wróbel, J. Grzonka, and J. Lewiński, *Chem. Commun.* **2016**, 52, 7340.

[52]. M. V. Pavliuk, A. M. Cieślak, M. Abdellah, A. Budinská, S. Pullen, K. Sokolowski, D. L. A. Fernandes, J. Szlachetko, E. L. Bastos, S. Ott, L. Hammarström, T. Edvinsson, J. Lewiński, and J. Sá, *Sustainable Energy Fuels* **2017**, 1, 69-73.

[53]. P. Krupiński, A. Kornowicz, K. Sokolowski, A. M. Cieślak, and J. Lewiński, *Chem. Eur. J.* **2016**, 22, 7817-7823.

[54]. J. Paczesny, M. Wolska-Pietkiewicz, I. Binkiewicz, Z. Wróbel, M. Wadowska, K. Matuła, I. Dzięcielewski, D. Pociecha, J. S. Koziorowska, J. Lewiński, and R. Hołyst, *Chem. Eur. J.* **2015**, 21, 16941-16947.

[55]. J. Paczesny, M. Wolska-Pietkiewicz, I. Binkiewicz, M. Wadowska, Z. Wróbel,

K. Matuła, W. Nogala, J. Lewiński, and R. Hołyst, *ACS Appl. Mater. Interfaces* **2016**, 8, 13532-13541.

[56]. K. Sokołowski, I. Justyniak, W. Bury, J. Grzonka, Z. Kaszkur, Ł. Mąkolski, M. Dutkiewicz, A. Lewalska, E. Krajewska, D. Kubicki, K. Wójcik, K. J. Kurzydłowski, and J. Lewiński, *Chem. Eur. J.* **2015**, 21, 5488-5495.

[57]. A. M. Cieślak, M.V. Pavliuk, L. D'Amario, M. Abdellah, K. Sokołowski, U. Rybinska, D.L.A. Fernandes, M.K. Leszczyński, F. Mamedov, A.M. El-Zhory, J. Föhlinger, A. Budinská, M. Wolska-Pietkiewicz, L. Hammarström, J. Lewiński, J. Sá, *Nano Energy* **2016**, 30, 187.

[58]. D. Prochowicz, K. Sokołowski, J. Lewiński, *Coordin. Chem. Rev.* **2014**, 270-271, 112-126.

[59]. S. Polarz, A. Orlov, A. Hoffmann, M. R. Wagner, C. Rauch, R. Kirste, W. Gehlhoff, Y. Aksu, M. Driess, M. W. E. van den Berg, M. Lehmann, *Chem. Mater.* **2009**, 21, 3889.

[60]. D. Lehr, M. Luka, M. R. Wagner, M. Buelger, A. Hoffmann, S. Polarz, *Chem. Mater.* **2012**, 24, 1771– 1778.

[61]. C. Lizandara-Pueyo, M. C. Morant-Minana, M. Wessig, M. Krumm, S. Mecking and S. Polarz, *RSC Adv.* **2012**, 2, 5298–5306.

[62]. M. A. Dreher, M. Krumm, C. Lizandara-Pueyo, and S. Polarz, *Dalton Trans.* **2010**, 39, 2232-2238.

[63]. S. Dilger, C. Lizandara-Pueyo, M. Krumm, and S. Polarz, *Adv. Mater.* **2012**, 24, 543–548.

[64]. M. Gerigk, J. Bahner, T. Kollek, S. Helfrich, R. Rosenberg, H. Cölfen, S. Polarz, *Part. Part. Syst. Charact.* **2017**, 34, 1600215.

[65]. K. Hagedorn, W. Li, Q. Liang, S. Dilger, M. Noebels, M. R. Wagner, J. S. Reparaz, A. Dollinger, J. Schmedt auf der Günne, T. Dekorsy, L. Schmidt-Mende and S. Polarz, *Adv. Funct. Mater.* **2016**, 26, 3424–3437.

[66]. V. Ischenko1, S. Polarz1, D. Grote, V. Stavarache, K. Fink, and M. Driess, *Adv. Funct. Mater.* **2015**, 15, 1945–1954.

[67]. C. Lizandara-Pueyo, S. Dilger, M. R. Wagner, M. Gerigk, A. Hoffmann, and

S. Polarz, *CrystEngComm*, **2014**, 16, 1525-1531.

[68]. C. Lizandara-Pueyo, S. Siroky, M. R. Wagner, A. Hoffmann, J. S. Reparaz, M. Lehmann, S. Polarz1, *Adv. Funct. Mater.* **2011**, 21, 295–304.

[69]. S. Polarz , F. Neues , M. W. E. van den Berg , W. Grünert , and L. Khodeir, *J. Am. Chem. Soc.* **2005**, 127, 12028–12034.

[70]. C. L. Pueyo, S. Siroky, S. Landsmann, M. W. E. van den Berg, M. R. Wagner, J. S. Reparaz, A. Hoffmann, and S. Polarz, *Chem. Mater.* **2010**, 22, 4263–4270.

[71]. M. Krumm, C. L. Pueyo, and S. Polarz, *Chem. Mater.*, **2010**, 22, 5129–5136.

[72]. S. Dilger, M. Wessig, M. R. Wagner, J. S. Reparaz, C. M. Sotomayor Torres, L. Qijun, T. Dekorsy, and S. Polarz, *Cryst. Growth Des.* **2014**, 14, 4593–4601.

[73]. M. Gerigk, P. Ehrenreich, M. R. Wagner, I. Wimmer, J. S. Reparaz, C. M. Sotomayor Torres, L. Schmidt-Mende, and S. Polarz, *Nanoscale*, **2015**, 7, 16969-16982.

[74]. C. Lizandara-Pueyo, M. W. E. van den Berg, A. De Toni, T. Goes, S. Polarz, *J. Am. Chem. Soc.* **2008**, 130, 16601–16610.

[75]. S. Polarz, A. V. Orlov, M. W. E. van den Berg, and M. Driess, *Angew. Chem. Int. Ed.* **2005**, 44, 7892–7896.

[76]. S. Polarz, A. Roy, M. Merz, S. Halm, D. Schröder, L. Schneider, G. Bacher, F. E. Kruis, and M. Driess, *Small* **2005**, 1, 540–552.

[77]. S. Polarz, J. Strunk, V. Ischenko, M. W. E. van den Berg, O. Hinrichsen, M. Muhler, and M. Driess, *Angew. Chem. Int. Ed.* **2006**, 45, 2965–2969.

[78]. S. Polarz, A. Roy, M. Lehmann, M. Driess, F. E. Kruis, A. Hoffmann, and P. Zimmer, *Adv. Funct. Mater.* **2007**, 17, 1385–1391.

[79]. S. Polarz, R. Regenspurger, and J. Hartmann, *Angew. Chem. Int. Ed.* **2007**, 46, 2426–2430.

[80]. S. Polarz, Andrey V. Orlov, F. Schüth and A.-H. Lu, *Chem. Eur. J.* **2007**, 13, 592–597.

[81]. M. Krumm, F. Pawlitzek, J. Weickert, L. Schmidt-Mende, and S. Polarz, *ACS Appl. Mater. Interfaces*, **2012**, 4, 6522–6529.

[82]. S. Polarz, C. L. Pueyo, M. Krumm, *Inorg. Chim. Acta* **2010**, 363, 4148-4157.

[83]. M. Voggenreiter, P. Vöpel, B. Smarsly, S. Polarz, *Z. Anorg. Allg. Chem.* **2017**, 643, 93-100.

[84]. S. D. Pike, E. R. White, M. S. P. Shaffer, and C. K. Williams, *Nat. Commun.* **2016**, 7, 13008.

[85]. M. L. Kahn, A. Glaria, C. Pages, M. Monge, L. S. Macary, A. Maisonnat and B. Chaudret, *J. Mater. Chem.* **2009**, 19, 4044-4060.

[86]. F. Rataboul, C. Nayral, M. J. Casanove, A. Maisonnat, B. Chaudret, *J. Organomet. Chem.* **2002**, 643, 307.

[87]. M. Monge, M. L. Kahn, A. Maisonnat and B. Chaudret, *Angew. Chem. Int. Ed.* **2003**, 42, 5321–5324.

[88]. A. Glaria, M. L. Kahn, P. Lecante, B. Barbara and B. Chaudret, *ChemPhysChem* **2008**, 9, 776–780.

[89]. M. L. Kahn, T. Cardinal, B. Bousquet, M. Monge, V. Jubera and B. Chaudret, *ChemPhysChem* **2006**, 7, 2392–2397.

[90]. J. Rubio-Garcia, A. Dazzazi, Y. Coppel, P. Mascalchi, L. Salomé, A. Bouhaouss, M. L. Kahn and F. Gauffre, *J. Mater. Chem.* **2012**, 22, 14538–14545.

[91]. M. L. Kahn, M. Monge, V. Collière, F. Senocq, A. Maisonnat, and B. Chaudret, *Adv. Funct. Mater.* **2005**, 15, 458–468.

[92]. M. L. Kahn, M. Monge, E. Snoeck, A. Maisonnat, and B. Chaudret, *Small* **2005**, 1, 221–224.

[93]. Y. Champouret, Y. Coppel, and M. L. Kahn, *J. Am. Chem. Soc.* **2016**, 138, 16322-16328.

[94]. Y. Coppel, G. Spataro, C. Pagès, B. Chaudret, A. Maisonnat, and M. L. Kahn, *Chem. Eur. J.* **2012**, 18, 5384 – 5393.

[95]. S. Saliba, C. V. Serrano, J. Keilitz, M. L. Kahn, C. Mingotaud, R. Haag, and Jean-Daniel Marty, *Chem. Mater.* **2010**, 22, 6301–6309.

[96]. S. Saliba, P. Davidson, M. Impéror-Clercd C. Mingotaud, M. L. Kahn and Jean-Daniel Marty, *J. Mater. Chem.* **2011**, 21, 18191.

[97]. S. Saliba, Y. Coppel, P. Davidson, C. Mingotaud, B. Chaudret, M. L. Kahn and Jean-Daniel Marty, *J. Mater. Chem.* **2011**, 21, 6821.

[98]. S. Saliba, C. Mingotaud, M. L. Kahn and Jean-Daniel Marty, *Nanoscale* **2013**, 5, 6641.

[99]. J. Jońca, J. Harmel, L. Joanny, A. Ryzhikov, M. L. Kahn, P. Fau, B. Chaudret, K. Fajerwerg, *Sens. Actuators B* **2017**, 249, 357-363.

[100]. S. Saliba, Y. Coppel, Marie-France Achard, C. Mingotaud, Jean-Daniel Marty, and M. L. Kahn, *Angew. Chem.* **2011**, 123, 12238 –12241.

[101]. S. Saliba, Y. Coppel, C. Mingotaud, Jean-Daniel Marty, and M. L. Kahn, *Chem. Eur. J.* **2012**, 18, 8084 – 8091.

[102]. Z. Zhao, Z. Zheng, C. Roux, C. Delmas, Jean-Daniel Marty, M. L. Kahn, and Christophe Mingotaud, *Chem. Eur. J.* **2016**, 22, 12424 – 12429.

[103]. G. Spataro, A. Dazzazi, S. Fortuny, Y. Champouret, Y. Coppel, J. Rubio-Garcia, A. Bouhaouss, F. Gauffre, and M. L. Kahn, *Eur. J. Inorg. Chem.* **2016**, 2056–2062.

[104]. A. Glaria, M. L. Kahn, T. Cardinal, F. Senocq, V. Juberab, and B. Chaudret, *New J. Chem.* **2008**, 32, 662-669.

[105]. A. Dazzazi, Y. Coppel, M. In, C. Chassenieux, P. Mascalchi, L. Salomé, A. Bouhaouss, M. L. Kahn and F. Gauffre, *J. Mater. Chem. C* **2013**, 1, 2158–2165.

[106]. J. Rubio-Garcia, Y. Coppel, P. Lecante, C. Mingotaud, B. Chaudret, F. Gauffre and M. L. Kahn, *Chem. Commun.* **2011**, 47, 988–990.

[107]. Z. Zheng, R. Butynska, C. V. Serrano, Jean-Daniel Marty, C. Mingotaud, and M. L. Kahn, *Chem. Eur. J.* **2016**, 22, 15614 – 15618.

[108]. M. L. Kahn, T. Cardinal, B. Bousquet, M. Monge, V. Jubera, and B. Chaudret, *ChemPhysChem* **2006**, 7, 2392 – 2397.

[109]. C. Amiens, B. Chaudret, D. Ciuculescu-Pradines, V. Collière, K. Fajerwerg, P. Fau, M. L. Kahn, A. Maisonnat, K. Soulanticac and K. Philippot, *New J. Chem.* **2013**, 37, 3374-3401.

[110]. A. Ryzhikov, J. Jońca, M. L. Kahn, K. Fajerwerg, B. Chaudret, A. Chapelle, P. Ménini, C. H. Shim, A. Gaudon, P. Fau, *J. Nanopart. Res.* **2015**, 17, 280.

[111]. J. Carrey1, H. Carrère, M. L. Kahn, B. Chaudret, X. Marie and M. Respaud, *Semicond. Sci. Technol.* **2008**, 23, 025003.

[112]. J. Massaad, Y. Coppel, M. Sliwa, M. L. Kahn, C. Coudret and F. Gauffre, *Phys. Chem. Chem. Phys.* **2014**, 16, 22775.

[113]. F. Güell, P. R. Martínez-Alanis, S. Khachadorian, J. Rubio-García, A. Franke, A. Hoffmann, and G. Santana, *Phys. Status Solidi B* **2016**, 253 (5), 883–888.

[114]. C. Pagès, Y. Coppel, M. L. Kahn, André Maisonnat, and B. Chaudret, *ChemPhysChem* **2009**, 10, 2334 – 2344.

[115]. Y. Coppel, G. Spataro, V. Collière, B. Chaudret, C. Mingotaud, A. Maisonnat, and M. L. Kahn, *Eur. J. Inorg. Chem.* **2012**, 2691–2699.

[116]. L. S. Macary, M. L. Kahn, C. Estournès, P. Fau, D. Trémouilles, M. Bafleur, P. Renaud, and B. Chaudret, *Adv. Funct. Mater.* **2009**, 19, 1775–1783.

[117]. J. Rubio-Garcia, A. Dazzazi, Y. Coppel, P. Mascalchi, L. Salomé, A. Bouhaouss, M. L. Kahn and F. Gauffre, *J. Mater. Chem.* **2012**, 22, 14538–14545.

[118]. C. Nayral, T. Ould-Ely, A. Maisonnat, B. Chaudret, P. Fau, L. Lescouzères, and A. Peyre-Lavigne, *Adv. Mater.* **1999**, 11, 61-63.

[119]. C. Nayral, E. Viala, V. Collière, P. Fau, F. Senocq, A. Maisonnat, B. Chaudret, *Appl. Surf. Sci.* **2000**, 164, 219-226.

[120]. P. Fau, M. Sauvan, S. Trautweiler, C. Nayral, L. Erades, A. Maisonnat, B. Chaudret, *Sens. Actuators B* **2001**, 78, 1-3, 83-88.

[121]. J.M. Ducéré, A. Hemeryck, A. Estève, M. D. Rouhani, G. Landa, P. Ménini, C. Tropis, A. Maisonnat, P. Fau, B. Chaudret, *J. Comput. Chem* **2011**, 33, 247–258.

[122]. C. Nayral, E. Viala, P. Fau, F. Senocq, J.-C. Jumas, A. Maisonnat, and B. Chaudret, *Chem. Eur. J.* **2000**, 6, 4082–4090.

[123]. J. Jońca, A. Ryzhikov, M. L. Kahn, K. Fajerwerg, A. Chapelle, P. Menini, P. Fau, *Chem. Eur. J.* **2016**, 22, 10127.

[124]. G. Casterou, V. Collière, P. Lecante, Y. Coppel, P.-A.Eliat, F. Gauffre, and M. L. Kahn, *Chem. Eur. J.* **2015**, 21, 18855–18861.

[125]. A. Glaria, M. L. Kahn, P. Lecante, B. Barbara, and B. Chaudret, *ChemPhysChem* **2008**, 9, 776–780.

[126]. A. Glaria, M. L. Kahn, A. Falqui, P. Lecante, V. Collière, M. Respaud, and B. Chaudret, *ChemPhysChem* **2008**, 9, 2035–2041.

[127]. A. Glaria, M. L. Kahn, B. Chaudret, P. Lecante, M.-J. Casanove, B. Barbara, *Mater. Chem. and Phys.* **2011**, 129, 605-610.

Chapitre II

Analyse statistique d’objets anisotropes

Résumé

L'analyse de la taille des nanoparticules à travers une simple représentation 2D est proposée afin d'extraire la corrélation entre la longueur et la largeur d'une collection ou d'un mélange de particules anisotropes. Par rapport aux statistiques habituelles portant sur une analyse statistique de la longueur et indépendamment de la largeur, cette approche simple montre facilement les différents types de nanoparticules et leur anisotropie. Pour chaque classe de nano-objets, la relation entre la largeur et la longueur (c'est-à-dire les corrélations fortes ou faibles entre ces deux paramètres) peut suggérer des informations concernant les processus de croissance et de nucléation. Cette approche permet de suivre l'effet sur la forme et sur la répartition en taille des processus physiques et/ou chimiques tels que la maturation. Diverses images de microscopie électronique à transmission provenant de la bibliographie ou de nos propres travaux sont utilisées à titre d'exemple pour démontrer l'efficacité et la simplicité d'une telle analyse.

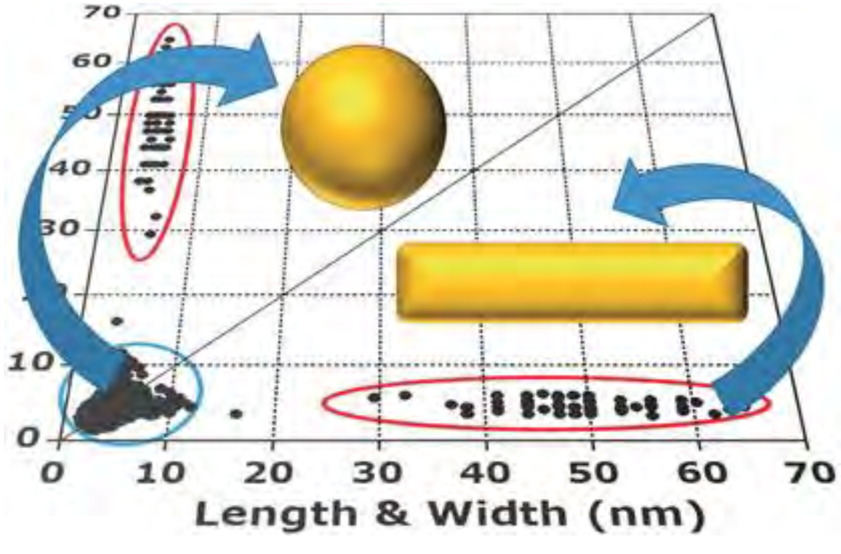

Contenu

Introduction

Whichever the chemical composition and the method used to synthetize the NPs may be, full characterization of the size and shape of the nano-objects should be achieved. Based on microscopy techniques such as transmission electron microscopy (TEM), atomic force microscopy…, images of the NPs are nowadays easily obtained and can be fully analyzed using popular software such as Image J. [1]

When the nanoparticles are anisotropic and have, for example, the shape of nanorods, the analysis of their size is often simply done by calculating an average value of their diameters and a distribution in their lengths. The main hypothesis made when performing such analysis is that width and length of the nanoparticles are totally un-correlated. Recently, some papers have shown that some correlations do exist between the minor axis and major axis in gold nanorods. [2] Such results limit the validity of the "usual" analysis performed on anisotropic particles.

Therefore, in this chapter, we propose a new and simple way to study the sizes of the NPs by creating a 2D size plot. This tool allows one to obtain qualitative and quantitative information concerning the length-width correlation. TEM pictures have been extracted from papers in the literature, purely selected on the quality of the TEM images and not on the composition of the NPs or the process for their synthesis. Other examples of TEM images have been chosen within the various studies on NPs performed in our teams. 2D size analyses have then been made and highlight that indeed more information can be gained from such a procedure than the "usual" statistical distribution of widths and lengths.

II.1. Principle and multivariate analysis

Following the example of 2D NMR with two-dimensional spectra pointing out the coupling between nuclei, [3] we propose to analyze a given set of NPs using a 2D plot to extract information on the correlation between widths and lengths of anisotropic objects. Each particle is characterized by two sizes, noted D_1 and D_2, measured on perpendicular axes. These two sizes generally correspond to the length and width of the nano-objects. For each particle and on a same graph, we plot D_1 as a function of D_2 and also D_2 as a function of D_1 (see Figure II.1).

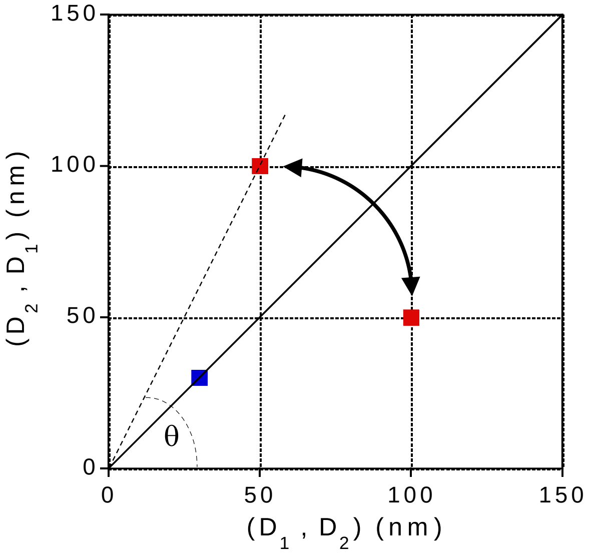

Figure II. 1. Schematic 2D size plot for two nanoparticles: an isotropic one (blue square) with a size ($D_1 = D_2$) around 40 nm; one nanorod with a length of 100 nm (D_1) and a width of 50 nm (D_2) associated to two points (red squares) on either side of the median (see double arrow).

In such a plot, any isotropic nanoparticle (case $D_1 = D_2$) will correspond to one diagonal point, lying on the median of the axes (see Figure II.1). On the contrary, anisotropic particles will be associated to two points (one for $x = D_1$ and $y = D_2$ and the second one for $x = D_2$ and $y = D_1$), lying symmetrically on both sides of the median. In fact, the aspect ratio, AR, of the particle (i.e. the ratio between its length and its width) is equal to the tangent of angle θ (see Figure II.1) defined by the x-axis and the line going through the origin of the graph and the upper point associated to the particle. θ close to 90° corresponds to large aspect ratio while θ close to 45° means aspect ratio near unity. Using this 2D size graph, it is therefore straightforward to distinguish groups of particles depending on their anisotropy.

Figure II.2 reports such a 2D plot for a real mixture of nanoparticles: points in the red ellipse are associated to nanorods (average AR = 10.9 ± 2.5 corresponding to an average θ angle of ca 85°) whereas the ones in the blue circle are related to smaller nanoparticles which could be considered isotropic (average AR = 1.25 ± 0.04 corresponding to an average θ angle close to 51°). For this and the following image analysis, Image J software was used manually or with a macro in order to extract width and length of nano-objects in various micrographs. The macro is based on the PSA macro, available at http://code.google.com/p/psa-macro. Overlapping nanoparticles are automatically rejected for the statistical analysis. The results were adjusted to account for the overestimation of particle size when fitting square or rectangular shapes with ellipses, according to Igathinathane et al. [4] The software leads to a table listing for each particle of two perpendicular dimensions D_1 and D_2. No ordering of these values is needed since this table is doubled by listing D_2 as a function of D_1. Plots of D_1 as a function of D_2 and D_2 as a function of D_1 are combined in the 2D size plot analyzed in this chapter.

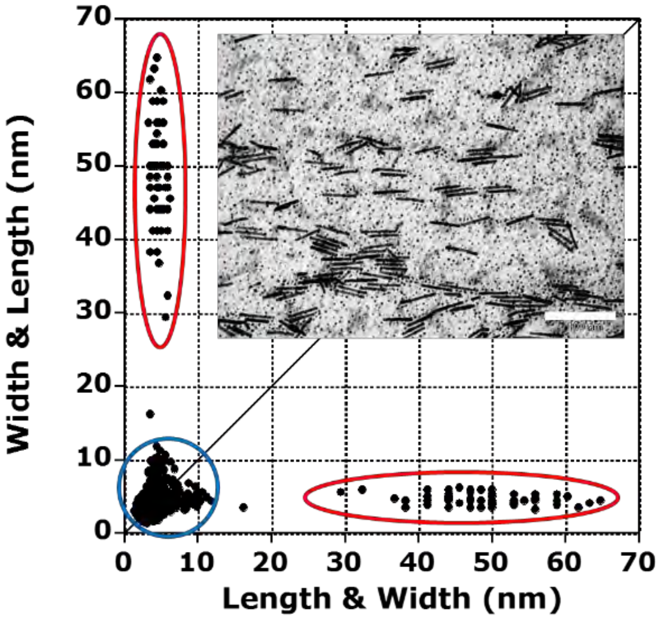

Figure II.2. 2D size plot of the TEM picture (bar length: 100 nm) of Co nanoparticles and nanorods.[5] The synthesis of this mixture was based on the procedure described in reference 6.

Besides the obvious advantage of the 2D plot to suggest various groups of NPs, characterizing the correlation between width and length of samples mainly constituted by nanorods could be highly enlightening. As an example, 2D size plots of various nanorod systems are given in Figure II.3. In Figure II.3A, corresponding to CdSe/CdS anisotropic NPs, length and width are both constant and present a polydispersity somewhat equivalent for both axes: the point cloud has a somewhat round shape. The average aspect ratio AR is close to 1.9 ± 0.3 corresponding to a θ angle of 62°. On the contrary, Figure II.3B corresponds to a distribution of size of ZnO NPs where the width is more or less constant (ca 10-11 nm) and the length of the nanorods is totally independent on the width and is spread over the 15-65 nm range. The average aspect ratio AR is close to 9.4 ± 2.9 corresponding to a θ angle close to 84°, demonstrating the large average anisotropy of the NPs. This case corresponds therefore to a total de-correlation between the two axes of the particles.

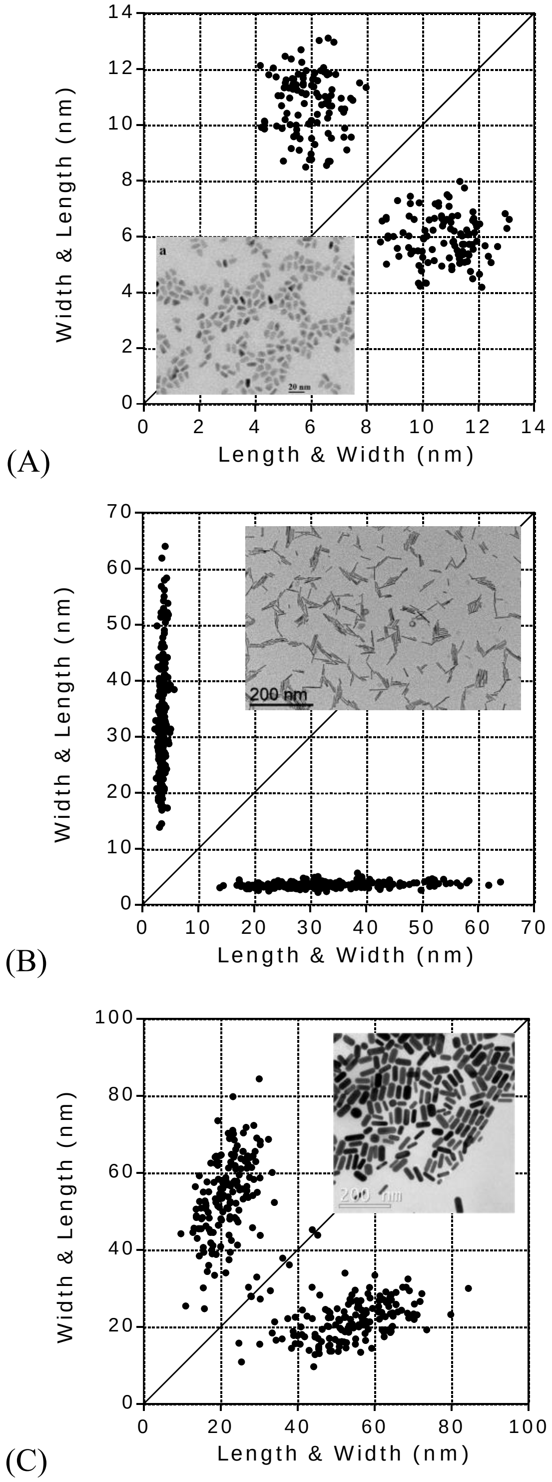

Figure II.3. 2D size plots of the TEM pictures: (A) bullet shaped CdSe/CdS nanoparticles. The micrograph was extracted from Figure 5a in reference 7; (B). ZnO nanorods. The synthesis of these NPs is given in the main part of this chapter; (C). Au nanorods. The micrograph was extracted from Figure 8 in reference 8.

Finally, the Figure II.3C shows an average variation of the width with the length, a partial correlation which can roughly be described by a linear dependency of length on width. Indeed, the data points from the clouds far from the diagonal domain suggest the relationship:

$$\text{Width (nm)} = 7.6 + 0.2574 * \text{length (nm)}.$$

Figure II.3 demonstrates therefore that the distribution in (width, length) and thus the correlation between both parameters could be strongly different from one sample to the other. In order to get a more quantitative analysis of these 2D plots, extraction of statistical parameters like average length and width and corresponding standard deviations should be performed. Nevertheless, this analysis is hampered by the presence of different sub-populations (such as the two in the red and blue ellipses in Figure II.2) that could necessitate tedious procedures to separate them, especially when these populations overlap each other.

In order to numerically identify the previous different sub-populations and to obtain their own statistical parameters, a multivariate analysis has been performed. This was done on the assumption that those clouds are issued from Gaussian probability densities and give us information about the average characteristics of those sub-populations (number, orientation, average length and width, corresponding standard deviation and correlation). Additionally, when a limited number of NPs can be counted, such an approach can also lead to improved accuracy for statistical analysis by helping to discard minor sub-population that are not representative of the samples. The multivariate analysis has been performed with the *mixmod* software (http://mixmod.org) using R package (http://www.r-project.org/). Apart from the Gaussian character of the probability densities, no assumption about the orientation, shape and volume of the different sub-populations was made during calculation. The number of sub-populations that composed the point clouds was fixed by the user or chosen numerically. Each sub-population was then characterized by the mean of the two studied variables (*i.e.* short and long axis lengths) as well as the corresponding standard deviations. Additionally, the correlation parameter ρ between both variables was calculated. The correlation is equal to zero when the two variables are totally independent and equal to 1 when they are affinely related to each other.

Applying such a procedure and as expected from the visual aspect of the plots, the NPs of Figure II.3A and II.3B show no statistical correlation between their length and width: the correlation parameter ρ is found close to zero (respectively 0.05 and 0.09). However, in Figure II.3C, the expected partial correlation is confirmed by the value of the correlation parameter ρ close to 0.33. Therefore, qualitatively and quantitatively, the correlation between length and width may strongly differ from one type of NPs to another. Importantly, this correlation may be a footprint of the nucleation-growth process occurring during the nanoparticle synthesis or of physical or chemical procedures used after synthesis. That is why 2D plots are of special interest to describe the modifications of structures occurring through time during growing or aging process.

II.2. Applications of the 2D plot analysis

The next examples will illustrate this point with the shape analysis of ZnO nanoparticles which were prepared through the following procedure: in the glove box, 92.68 mg of dodecylamine (DDA, 2 equivalents) was added in a small vial to 57.9 mg of zinc precursor $[Zn(C_6H_{11})_2]$. After complete mixing, the vial was taken out of the glove box and exposed to the air. After various reaction times, part of the sample was analyzed by TEM. Samples for TEM studies were prepared by slow evaporation of droplets of colloidal solution deposited on carbon-coated copper grids.

Figure II.4 shows the TEM pictures and corresponding 2D plots of ZnO NPs obtained by hydrolysis of an organometallic precursor as a function of the reaction time (from 2 to 80 hours). The point clouds obtained at 2 and 4 h are centered on the median ($\theta = 45°$). The 2D plots show clearly that the point clouds became rounder at 4 h than they were at 2 h. This corresponds to the presence of quasi isotropic nanoparticles, the average size of which evolves from ca 3.4 ± 1.7 to 5.3 ± 2.7 nm. The growth of ZnO NPs clearly starts by a nucleation step where pristine isotropic nanoparticles are formed.

During the first hours, these pristine nanoparticles are maturing and their mean size increases. Statistical analysis of these 2D plots confirms this qualitative examination. Satisfactory results are obtained with only one sub-population with an increase of the correlation parameter ρ up to ca 0.54 (see Figure II.5).

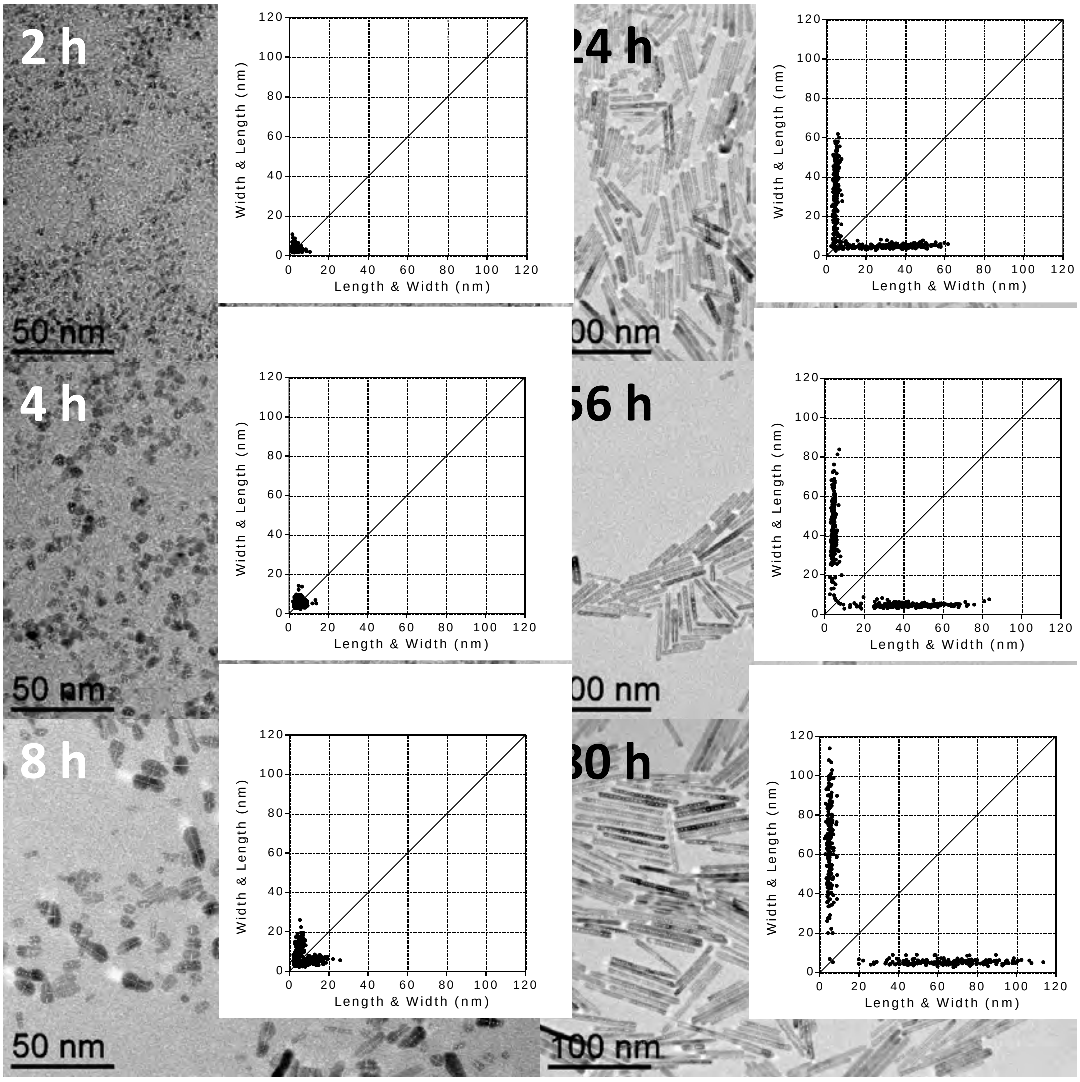

Figure II.4. 2D size plots and TEM pictures of ZnO/2DDA NPs versus hydrolysis time (from 2 to 80 hours).

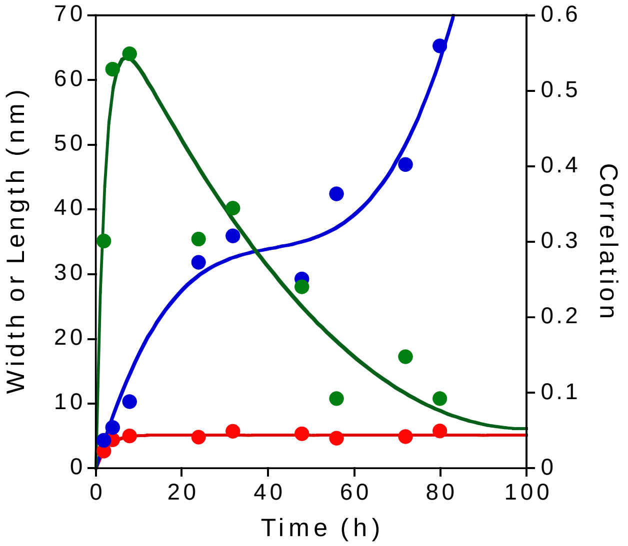

Figure II.5. Mean width (red), mean length (blue) and corresponding correlation (green) issued from a multivariate analysis (with a single Gaussian) of data corresponding to ZnO NPs versus hydrolysis time (from 2 to 80 hours). The lines are just guides for the eyes. See also Figure 3 for the corresponding 2D plots.

At 8 h, the 2D plot shows that the point cloud starts to extend, suggesting that the anisotropic growth of the nanoparticles has begun. In the following hours, the points cloud extends more and more up to 100 nm, while remaining parallel to the 2D plot axis at ca 5-6 nm: the rods are becoming longer but their widths are somewhat maintained. At 80 h, no correlation between the length and the width is then observed for these highly anisotropic NPs (aspect ratio AR close to 13.2 ± 4.8 corresponding to a θ angle of 86°). This suggests that growth occurs mainly along the long axis of the nanoparticles. Again, this qualitative examination is confirmed by the statistical analysis of the 2D plots. As shown in Figure II.5, the length of the nanoparticles is increasing while the width is rather constant for hydrolysis time longer than 8 h. In parallel to this evolution, the correlation value progressively decreased upon time to reach values near zero. Interestingly, after 24 h, less and less points are located close to the median of the 2D plot (see Figure II.4). The number of isotropic nanoparticles is decreasing and after 80 h, very few of them are indeed observed. This result suggests that no nucleation occurs during the period of anisotropic growth and that the nucleation and growth steps are uncorrelated and occurred sequentially. Moreover, growth by oriented attachment is suggested: the isotropic nanoparticles are consumed to the benefit of the length of the rods that increases concomitantly (see Chapter III for further discussion). This example highlights how 2D plots are extremely useful to follow the growth of nano-objects and help get insights into the mechanism. Their statistical analysis gives moreover access to quantitative values of relevant estimators.

A second example demonstrating the interest of the proposed 2D plot was obtained through the analysis of some TEM pictures from reference 9. In this paper, K. Park *et al.* are reporting the effect on the gold nanoparticle growth of the addition of a cosurfactant, the benzyldimethylhexadecylammonium bromide (BDAC). They clearly demonstrate that this addition at the early stage of the NP growth induces a decrease of the mean diameter and an increase of the mean length and aspect ratio of the gold nanorods. This evolution is also clearly seen in the 2D size plots of the corresponding TEM pictures (see Figure II.6).

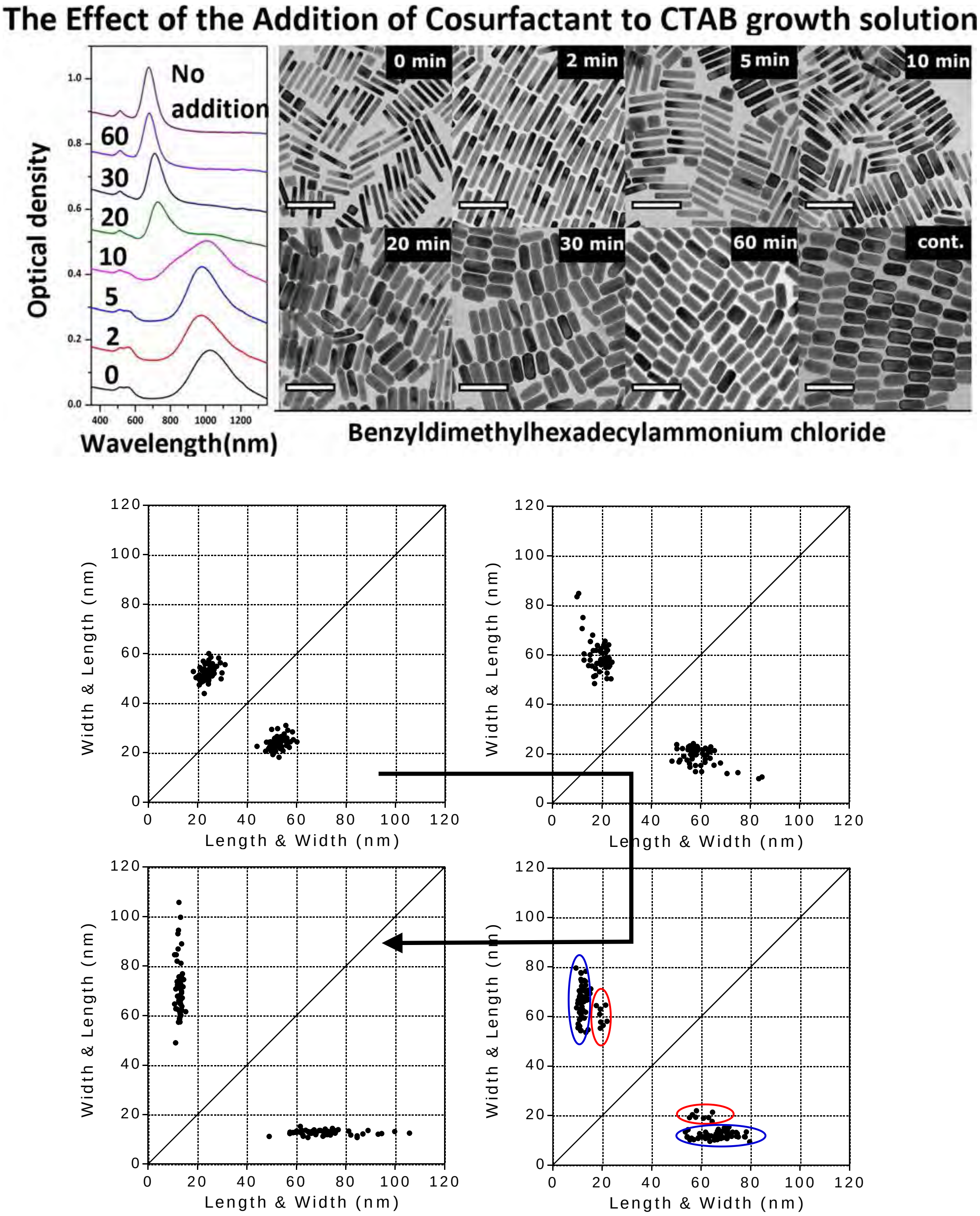

Figure II.6. Top: TEM picture extracted from the Figure 2 in the reference 9. Bottom: 2D size plots of these TEM pictures of gold nanorods synthetized with the addition to the initial growth solution of a cosurfactant at various implement times (in the order given by the arrow: after the end of the reaction, 20 min, 10 min or 2 min after the start of the reaction).

As can be seen in Figure II.6, the addition of BDAC at shorter time moves the (width, length) distribution towards the upper left and bottom right corners of the diagram. However, what was not expected, is that the shape of this distribution is changing with the modification of the experimental parameters.

The correlation between width and length (calculated for the whole set of points) is therefore strongly disturbed. Without cosurfactant addition, width and length of the nanorods are significantly correlated (average $\rho = 0.38$). This may correspond to a simultaneous growth on the two axes with two different but correlated speeds. With the addition of BDAC, the more or less isotropic (width, length) distribution is more and more elongated, and, for short implement time, it demonstrates a de-correlation between the length and the width of the nanorods (correlation is equal to 0.06, 0.15 and 0.07 for implementation time equal to 20, 10 and 2 min respectively). A multivariate analysis of this data leads to more detailed insights on the phenomenon. Indeed, as can be seen in Figure II.6 at 10 and 20 min implementation times, point clouds present an apparent complex structure with two different sub-populations of nanoparticles (see red and blue ellipses in Figure II.6). The multivariate analysis of this data enables us to isolate two sub-populations and to obtain more accurate quantitative values for each ones (proportion, average length and width, correlation). One population corresponds to thin NPs with an average width around 13 nm and a length of 65 nm (ρ close to 0.2-0.3) and a second one is associated to thicker NPs with an average width around 22 nm and a length around 55 nm (ρ close to 0.15-0.2). Figure II.7 shows that the proportion of both sub-populations changes as a function of implementation time. The “thin” NPs are disappearing in the first 30 minutes after which only the “thick” NPs are observed.

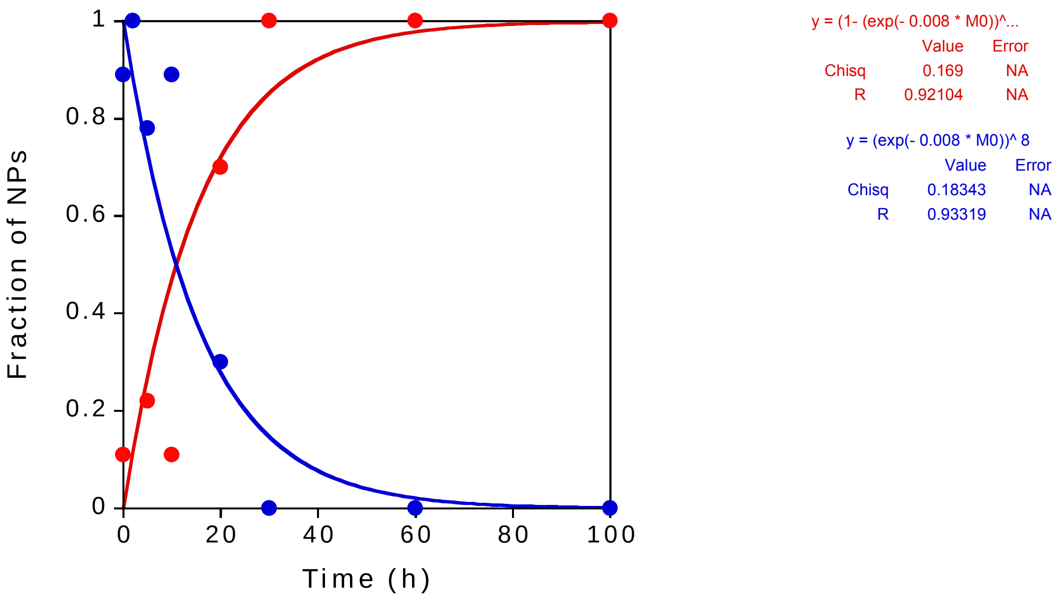

Figure II.7. Multivariate analysis of the 2D size plots corresponding to the Figure II.6: evolution of the fraction of the sub-populations corresponding to thin nanoparticles (full circle in blue) and to thicker nanoparticles (full circle in red) of gold nanorods synthetized with the addition to the initial growth solution of a cosurfactant at various implement times. The lines are just guides for the eyes.

Therefore, the 2D plot and the multivariate analysis strongly suggest in this system the competition between two chemical processes. One is leading to “thick” NPs resulting from a simultaneous growth along the two axis of the NPs. The second one gives “thin” NPs, because of a limitation of the transversal growth due to an adsorption of the cosurfactant on the (100) and (110) Au facets. The interpretation and discussion of such an evolution is however limited in this chapter, since our present analysis is made on selected micrographs and not on a set of TEM pictures representative of the global samples. A statistical bias may therefore be created by this selection process.

The reverse evolution in terms of correlation can also be seen. For example, in the paper of Ng et al.,[8] the initial gold nanorods (see blue points in Figure II.8) present a weak correlation between their lengths (in the range 40-80 nm) and their widths (around 15 nm) with ρ = 0.12.

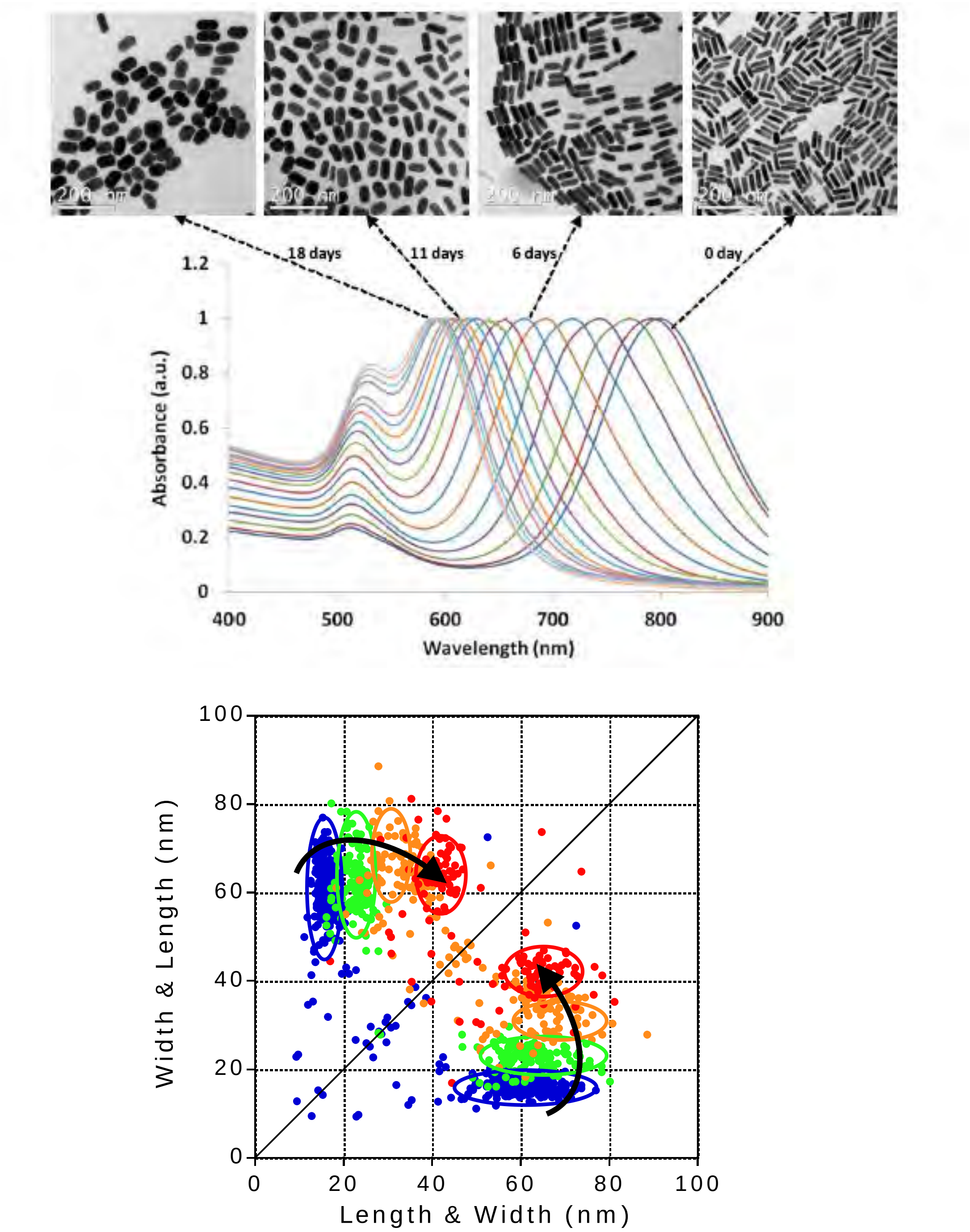

Figure II.8. Top: TEM picture extracted from the Figure 9 in the reference 8. Bottom: 2D size plots of the TEM pictures of gold nanorods being reshaped by a thermal process at 30°C during various increasing times. Blue points: initial rods. Green points: after 6 days. Orange points: after 11 days. Red points: after 18 days. The micrographs were extracted from Figure 9 in reference 8.

Maintained at a temperature of 30°C, their shapes are changing with time. As seen in Figure II.8, their aspect ratio is decreasing (since the distribution of points tends to be closer to the median of the plot) but also their lengths seem to be more correlated to their widths (see red points in Figure II.8). Indeed, the correlation parameter is equal to 0.23, 0.26 and 0.35 after 6, 11 or 18 days of reshaping respectively. Such a result may just be related to the average conservation of the volume of the particles during the reshaping process. This more or less constant volume indeed imposes a relationship between the length and the width of the objects. Again, since our present analysis is made on selected micrographs and not on a set of TEM pictures representative of the global samples, a statistical bias may therefore be created. Such a possibility limits the discussion in the present chapter. Further use of this 2D plot and statistical analysis will be presented in the next chapter concerning the synthesis of ZnO nanoparticles.

Conclusion

The previous examples suggest that taking into account the correlation between width and length of the NPs may be essential to gain a better understanding of some critical steps or processes occurring during NP formation. The proposed 2D plots may be a simple tool to visualize qualitatively such a correlation, which can also be extracted quantitatively through a multivariate analysis. In the near future, such analysis can be compared to theoretical models developed to explain the nucleation and growth processes of NPs, leading to a better control of the NPs morphology.

References

[1]. (a) http://imagej.nih.gov/ij/; (b) P. J. Wojcik, "How to measure nanoparticle size distribution using SEM pic". http://www.youtube.com/watch?v=D5KL40CFXqA.

[2]. (a) M. J. Walsh, S. J. Barrow, W. Tong, A. M. Funston, J. Etheridge, Symmetry Breaking and Silver in Gold Nanorod Growth. *ACS Nano* **2015**, 9, 715-724; (b) S. Gomez-Grana, F. Hubert, F. Testard, A. Guerrero-Martinez, I. Grillo, L. M. Liz-Marzan, O. Spalla, Surfactant (Bi)Layers on Gold Nanorods. *Langmuir* **2012**, 28, 1453-1459; (c) F. Hubert, F. Testard, G. Rizza, O. Spalla, Nanorods versus Nanospheres: A Bifurcation Mechanism Revealed by Principal Component TEM Analysis. *Langmuir* **2010**, 26, 6887-6891.

[3]. P. Giraudeau, Quantitative 2D liquid- state NMR. *Magn. Reson. Chem.* **2014**, 52, 259-272.

[4]. C. Igathinathane, L. O. Pordesimo, E. P. Columbus, W. D. Batchelor, S. R. Methuku, Shape identification and particles size distribution from basic shape parameters using ImageJ. *Comput. Electron. Agr.* **2008**, 63 (2), 168-182.

[5]. Personal communication of Dr B. Lonetti.

[6]. O. Riou, B. Lonetti, P. Davidson, R. P. Tan, B. Cormary, A. F. Mingotaud, E. Di Cola, M. Respaud, B. Chaudret, K. Soulantica, M. Mauzac, Liquid Crystalline Polymer-Co Nanorod Hybrids: Structural Analysis and Response to a Magnetic Field. *J. Phys. Chem. B* **2014**, 118 (11), 3218-3225.

[7]. J. Bomm, A. Buchtemann, A. Fiore, L. Manna, J. H. Nelson, D. Hill, W. van Sark, Fabrication and spectroscopic studies on highly luminescent CdSe/CdS nanorod polymer composites. *Beilstein J. Nanotechnol.* **2010**, 1, 94-100.

[8]. K. C. Ng, W. L. Cheng, Fine-tuning longitudinal plasmon resonances of nanorods by thermal reshaping in aqueous media. *Nanotechnology* **2012**, 23, 105602.

[9]. R. C. Wadams, L. Fabris, R. A. Vaia, K. Park, Time-Dependent Susceptibility of the Growth of Gold Nanorods to the Addition of a Cosurfactant. *Chem. Mater.* **2013**, 25, 4772-4780.

Chapitre III

Une vision nouvelle sur la croissance de nanoparticules anisotropes de ZnO

Résumé

Des nanobâtonnets d'oxyde de zinc cristallins bien définis ont été obtenus par hydrolyse du précurseur organométallique, le dicyclohexyl zinc, [Zn(Cy)$_2$] en présence seulement d'une amine primaire à chaine alkyl. Leur mécanisme de formation a été étudié grâce à une analyse multivariée des images TEM. Un processus de croissance par attachement orienté est démontré. Cette compréhension du mécanisme de croissance nous a permis un contrôle encore meilleur de la taille des nanobâtonnets de ZnO. Celle-ci peut, en effet, être facilement réglée en ajustant la vitesse d'hydrolyse, le temps de maturation du mélange réactionnel avant l'hydrolyse, la nature du ligand ainsi que la quantité d'eau.

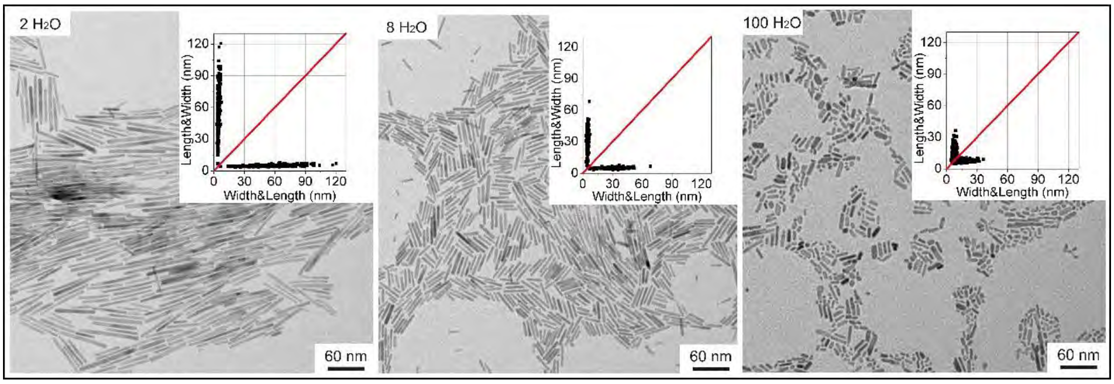

Contenu

Introduction

For several years (see chapter I), the team of LCC has developed the preparation of zinc oxide NPs taking advantage of the exothermic hydrolysis of dicyclohexyl zinc precursor, [Zn(cy)$_2$], to get, in one step and under mild conditions (*i.e.* room temperature and atmospheric pressure), well-defined crystalline zinc oxide NPs.[1-2] In this process, the control of the morphology (*i.e.* either isotropic NPs or nanorods) is achieved by varying the experimental conditions: isotropic NPs are obtained in the presence of alkyl chain amine ligands in an organic solvent while nanorods are obtained in the same experimental conditions but in the absence of solvent.[3-4] If the mechanism behind these observations has not yet been elucidated, results suggest the critical role of different parameters (composition of the pristine reaction mixture, amount of water, kinetics parameters of the reaction, temperature…) to achieve a control over the final morphology of the obtained nanorods. In this chapter, we investigate the effect of different parameters in order to obtained nanorods with controlled length. To get further insights upon relevant information on growth processes, we will use the tools presented in Chapter II to analyze correlation between length and width of anisotropic particles obtained under various experimental conditions.

III.I. Influence of the reaction and aging time

In a typical experiment, the dicyclohexyl zinc precursor, [Zn(Cy)$_2$], is mixed at room temperature with two equivalents of alkylamine RNH$_2$ (dodecylamine, DDA, R = $C_{12}H_{25}$ or octylamine, OA, R = C_8H_{17}) as ligand. No solvent was used. After 10 minutes, water is introduced by opening the vial. The hydrolysis reaction takes then place leading to the formation of ZnO NPs. Influence of this hydrolysis time was first investigated (see Figure III.1).

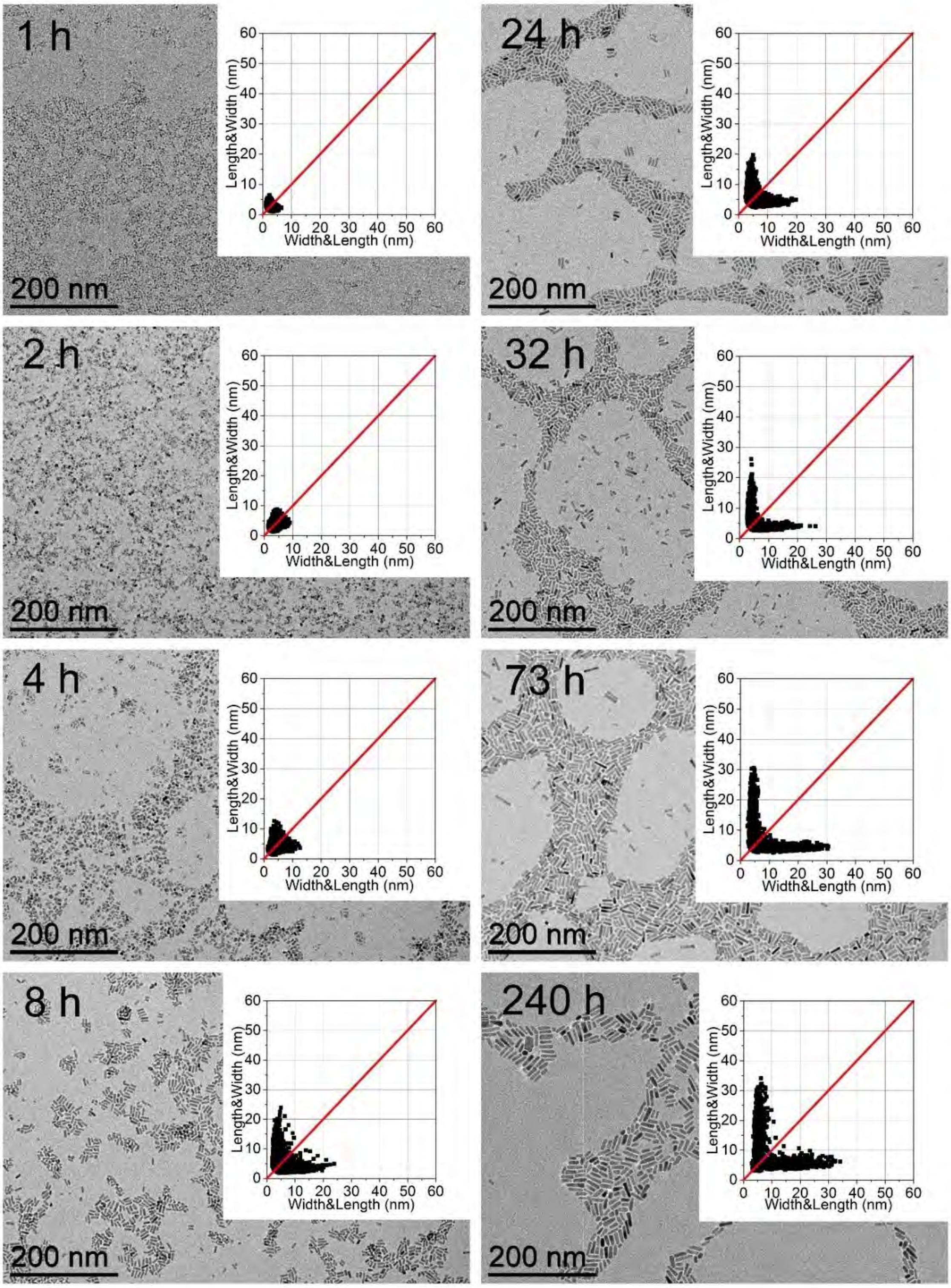

Figure III.1. 2D size plots and TEM pictures of ZnO/2DDA NPs versus hydrolysis time (from 1 to 240 hours).

Width and length of these NPs as a function of time of these NPs is depicted in Figure

III.2B. At short times (up to 4h), quasi isotropic nanoparticles are formed, the average size of which evolves from ca 3.4 ± 1.7 to 5.6 ± 3.9 nm (See Table III.1 and III.2).

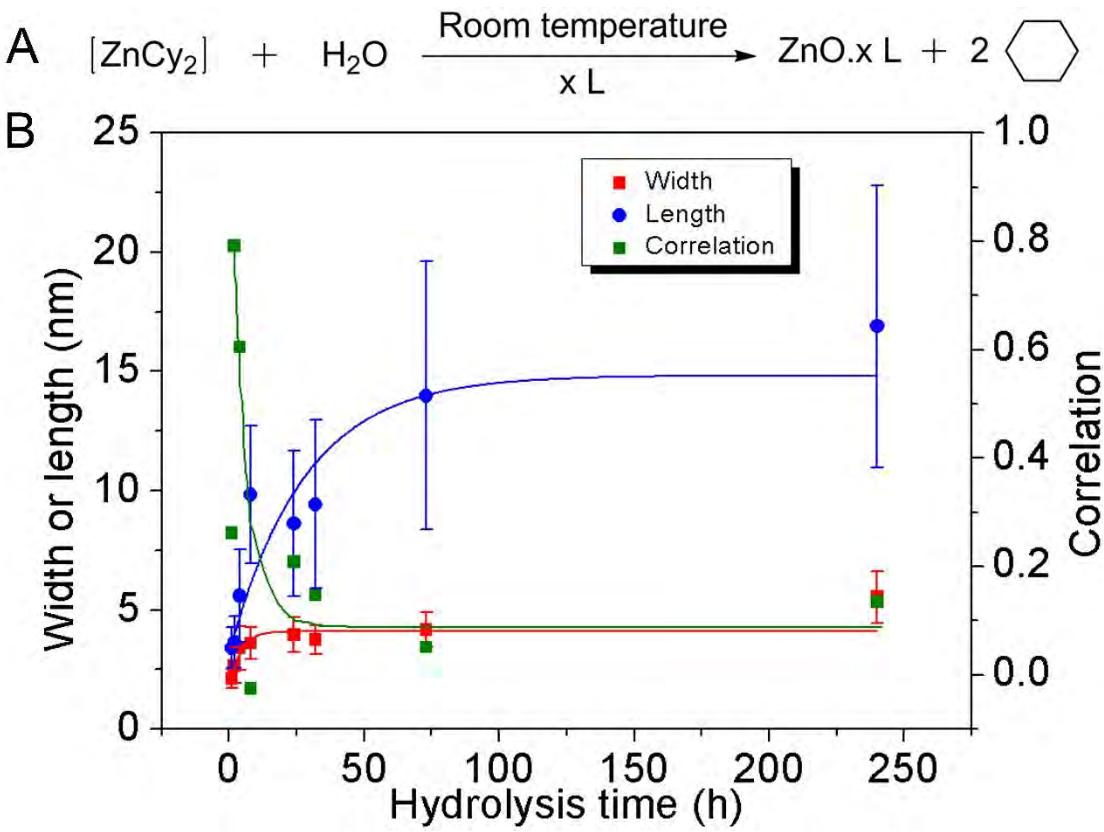

Figure III.2. A. Preparation process. B. Mean width (red), mean length (blue) and corresponding correlation (green) obtained from a multivariate analysis (with a single Gaussian) of TEM data corresponding to the evolution of ZnO NPs average size versus hydrolysis time (from 1 to 240 hours). See also Figure III.1 for corresponding 2D plots. The lines are just guides for the eyes.

Hydrolysis time (hour)	Length (nm)	Width (nm)	Population Weight (%)	Correlation
1	2.9 ± 0.8	2.0 ± 0.5	56.4	0.03
	4.1 ± 1.7	2.3 ± 0.9	43.6	0.01
2	3.2 ± 1.1	2.4 ± 1.0	70.2	0.75
	4.8 ± 2.3	3.3 ± 1.7	29.8	0.65
4	6.9 ± 3.0	3.8 ± 1.7	57.2	0.20
	3.9 ± 1.8	2.8 ± 1.3	42.8	0.73
8	10.1 ± 7.4	3.3 ± 1.3	79.2	0.39
	6.7 ± 4.8	4.1 ± 2.6	20.9	0.72
24	9.6 ± 5.9	3.8 ± 1.2	71.3	0.45
	6.2 ± 3.0	4.3 ± 1.8	28.7	0.68
32	8.5 ± 5.3	3.5 ± 0.9	70.7	-0.07
	11.6 ± 8.8	4.3 ± 1.1	29.3	-0.23
73	15.0 ± 11.2	3.9 ± 0.9	72.3	0.42
	11.4 ± 9.4	4.8 ± 1.7	27.7	0.08
240	18.6 ± 10.9	5.3 ± 1.7	74.9	0.29
	11.9 ± 8.4	6.2 ± 2.9	25.1	0.60

Table III.1. Multivariate analysis of the 2D plots corresponding to the TEM images of the Figure III.1 through Rmixmod program (the dispersion is given as twice the standard deviation obtained from calculations, and number of cluster was set to 2).

Hydrolysis time (hour)	Length (nm)	Width (nm)	Correlation
1	3.4 ± 1.7	2.1 ± 0.8	0.26
2	3.6 ± 2.2	2.7 ± 1.5	0.79
4	5.6 ± 3.9	3.4 ± 1.9	0.61
8	9.8 ± 5.8	3.6 ± 1.4	-0.03
24	8.6 ± 6.1	4.0 ± 1.5	0.21
32	9.4 ± 7.1	3.7 ± 1.2	0.15
73	14.0 ± 11.2	4.2 ± 1.5	0.05
240	16.9 ± 11.9	5.5 ± 2.2	0.14

Table III.2. Multivariate analysis of the 2D plots corresponding to the TEM images of the Figure III.1 through Rmixmod program (the dispersion is given as twice the standard deviation obtained from calculations, and number of cluster was set to 1).

The growth of ZnO NPs clearly starts by a nucleation step where pristine isotropic nanoparticles are formed. During the first hours, these pristine nanoparticles are maturing and their mean size increases. An increase of the correlation parameter ρ up to ca 0.80 is observed. At 8 h, the 2D plot shows that the point cloud starts to extend, suggesting that the anisotropic growth of the NPs has begun. In the following hours, the points cloud extends more and more up to 17 nm, while remaining parallel to the 2D plot axis at ca 5-6 nm: the rods are becoming longer but their widths are somewhat maintained. At 240 h, no correlation between the length and the width is then observed for these anisotropic NPs.

These results suggest that growth occurs mainly along the long axis of the nanoparticles. After the nucleation step, the number of isotropic nanoparticles is decreasing, less than 1% of isotropic NPs are indeed observed after 32h whereas the overall length is still increasing (Figure III.3 and Table III.3).

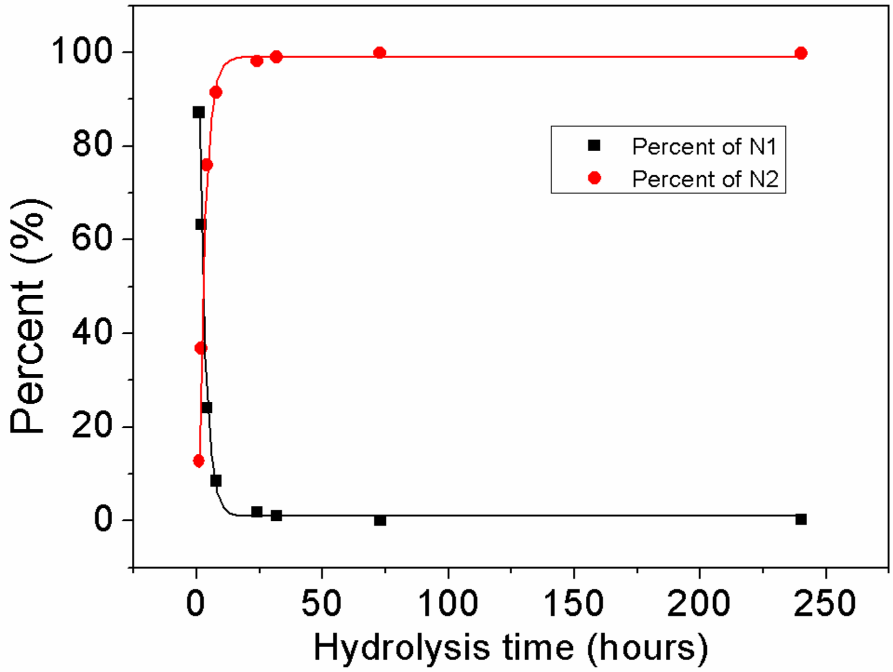

Figure III.3. Percentage (deduced from a multivariate analysis) of the two populations N1(isotropic NPs) and N2 (anisotropic NPs) depending on the hydrolysis time. See also the Figure III.1 and Table III.3.

Hydrolysis time (hour)	Number of N1	Number of N2	Percent of N1 (%)	Percent of N2 (%)
1	2451	361	87.2	12.8
2	1254	730	63.2	36.8
4	347	1093	24.1	75.9
8	120	1294	8.5	91.5
24	22	1136	1.9	98.1
32	9	793	1.1	98.9
73	1	937	0.1	99.9
240	1	630	0.2	99.8

Table III.3: Multivariate analysis of the 2D plots corresponding to the TEM images of Figure III.1 through a modified Rmixmod program.

This result suggests that no or little nucleation occurs during the period of anisotropic growth and that the nucleation and growth steps are uncorrelated and occurred sequentially. Moreover, growth by oriented attachment is suggested: the isotropic nanoparticles are consumed to the benefit of the length of the rods that increases concomitantly. At longer time Ostwald ripening might also be involved. Thus hydrolysis time appears as a first parameter to obtain nanorods with chosen length. Whereas initial nucleation reaction is very fast (after 1 minute solutions became luminescent which demonstrate the formation of ZnO NPs), growth mechanism seems to be stopped only after 3 days.

Another parameter to obtain such a control is to change the waiting time before starting hydrolysis step after mixing amine and zinc precursor reactants (see Figure III.4 and III.5 and Table III.4, III.5 and III.6). After mixing, the viscosity of the solution increases slowly to behave after 6 hours as a glass state gel (see Chapter IV for more details). Then final shape of the obtained NPs was observed 3 days after starting the hydrolysis process. Meanwhile, as shown in Figure III.6, the average length of the ZnO NPs decreases from 9.3 ± 7.5 nm to 3.4 ± 2.6 nm from aging time of 10 minutes to 6 hours, and remain almost constant after 6 hours.

The width didn’t change a lot from 10 minutes to 5 hours, but decreases from 3.6 ± 1.7 nm to 2.1 ± 1.3 nm after 5 hours, and then remains almost constant. A correlation between viscosity of the medium and NPs length is clearly observed (see Figure III.6) suggesting that nucleation occurred in a first step, after which non hydrolyzed mixture start to be attacked by diffusing water, thus favoring the growth of the former nucleated particles. Therefore the diffusion speed of the reactants and water is a second critical parameter for the nucleation and growth process. Longer aging time leads to higher viscosity, which can limit the diffusion speed and growth process and consequently shorter NPs could be obtained. These results are also in agreement with oriented attachment mechanism: in highly viscous medium, growing of isotropic nanoparticles by diffusion of ions is favored compared to diffusion and attachment of different nuclei.

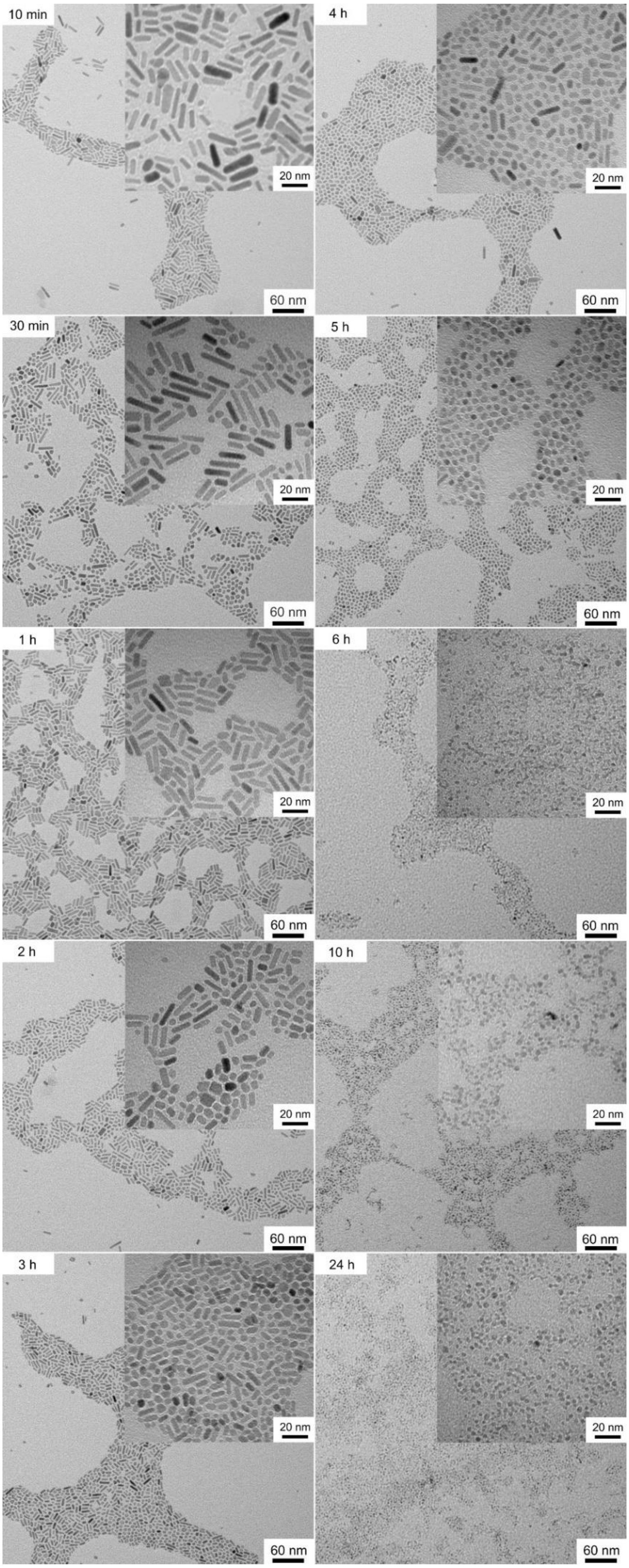

Figure III.4. TEM images of the ZnO/2DDA NPs *versus* aging time before hydrolysis.

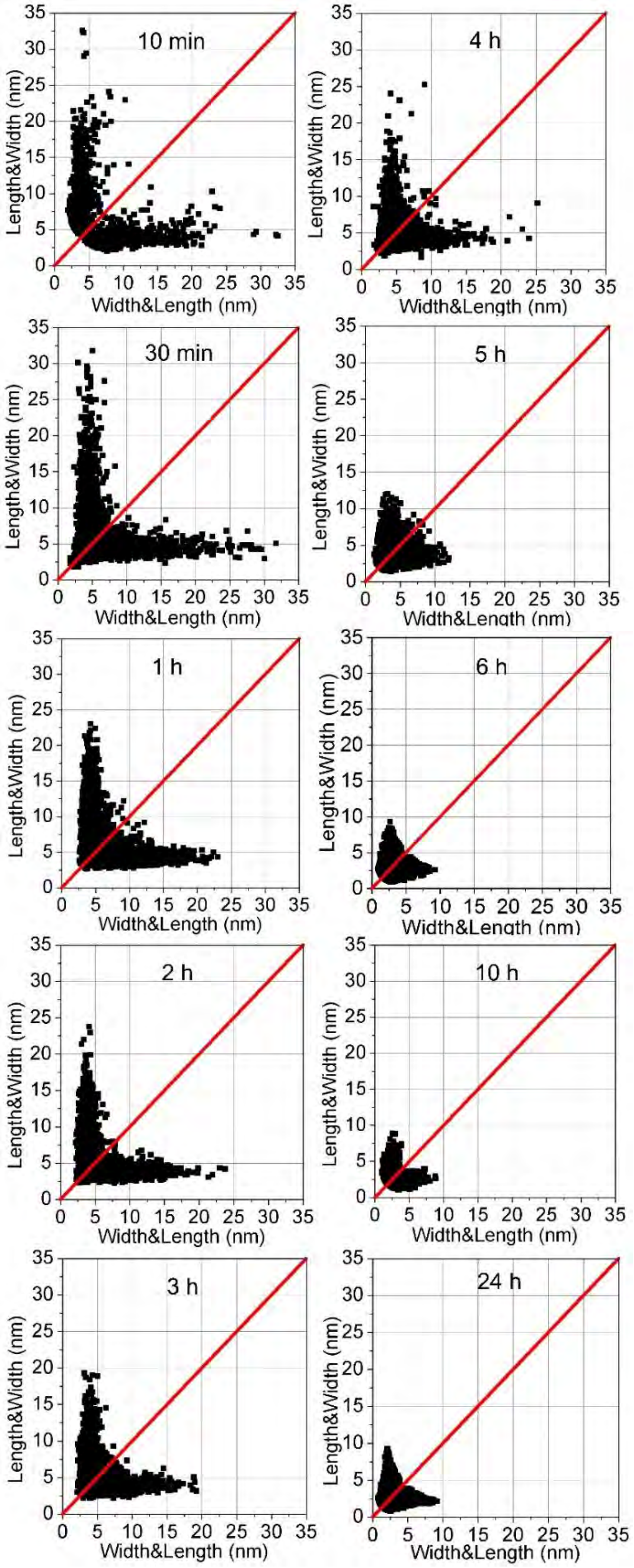

Figure III.5. 2-D size plots corresponding to the TEM images of Figure III.4.

Aging time	Length (nm)	Width (nm)	Population Weight (%)	correlation
10 minutes	8.0 ± 3.9	3.5 ± 1.0	77.6	0.24
	14.0 ± 9.3	4.5 ± 2.7	22.4	0.04
30 minutes	11.1 ± 9.8	4.3 ± 1.7	52.8	0.23
	5.8 ± 2.6	4.6 ± 2.1	47.2	0.84
1 hour	11.9 ± 7.3	4.1 ± 1.1	73.0	0.22
	8.4 ± 3.8	5.1 ± 2.4	27.0	0.44
2 hours	9.7 ± 6.5	3.7 ± 1.2	65.7	0.21
	5.7 ± 2.8	4.0 ± 1.7	34.3	0.97
3 hours	9.2 ± 5.9	3.8 ± 1.3	57.9	0.23
	5.6 ± 2.0	4.4 ± 1.7	42.1	0.77
4 hours	5.2 ± 2.2	4.3 ± 1.9	58.2	0.88
	8.5 ± 6.1	4.1 ± 1.4	41.8	0.35
5 hours	4.7 ± 2.0	3.7 ± 1.7	71.8	0.86
	6.3 ± 3.2	3.3 ± 1.4	28.2	0.30
6 hours	2.6 ± 0.9	1.8 ± 0.7	56.8	0.53
	4.4 ± 2.5	2.5 ± 1.4	43.2	0.34
10 hours	2.7 ± 0.8	1.8 ± 0.6	52.5	0.14
	4.1 ± 2.1	2.2 ± 1.2	47.5	0.23
24 hours	2.7 ± 1.2	1.9 ± 1.1	67.5	0.76
	4.9 ± 2.6	2.4 ± 1.0	32.5	0.22

Table III.4. Multivariate analysis of the 2D plots corresponding to the TEM images of the Figure III.4 through Rmixmod program (the dispersion is given as twice the standard deviation obtained from calculations, and number of cluster was set to 2).

Aging time	Length (nm)	Width (nm)	correlation
10 minutes	9.3 ± 7.5	3.7 ± 1.8	0.40
30 minutes	8.6 ± 9.0	4.4 ± 1.9	0.13
1 hour	10.9 ± 7.3	4.4 ± 1.8	-0.02
2 hours	8.3 ± 6.7	3.8 ± 1.4	0.10
3 hours	7.7 ± 5.9	4.1 ± 1.6	0.02
4 hours	6.6 ± 5.4	4.2 ± 1.7	0.32
5 hours	5.1 ± 2.8	3.6 ± 1.7	0.41
6 hours	3.4 ± 2.6	2.1 ± 1.3	0.61
10 hours	3.4 ± 2.1	2.0 ± 1.0	0.40
24 hours	3.4 ± 2.7	2.1 ± 1.2	0.54

Table III.5. Multivariate analysis of the 2D plots corresponding to the TEM images of the Figure III.4 through Rmixmod program (the dispersion is given as twice the standard deviation obtained from calculations, and number of cluster was set to 1).

Aging time	Number of N1	Number of N2	Percent of N1 (%)	Percent of N2 (%)
10 min	39	975	3.8	96.2
30 min	71	1499	4.5	95.5
1 hour	14	1056	1.3	98.7
2 hours	76	1166	6.1	93.9
3 hours	50	904	5.2	94.8
4 hours	105	1375	7.1	92.9
5 hours	664	1956	25.3	74.7
6 hours	1691	244	87.4	12.6
10 hours	978	94	91.2	8.8
24 hours	1309	203	86.6	13.4

Table III.6: Multivariate analysis of the 2D plots corresponding to the TEM images of Figure III.4 through a modified Rmixmod program.

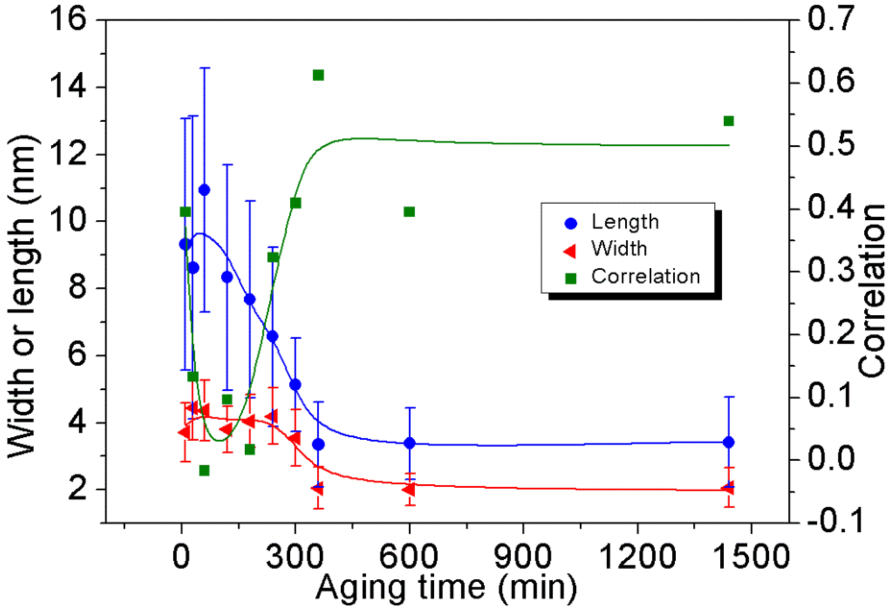

Figure III.6. Mean width (red), mean length (blue) and corresponding correlation (green) obtained from a multivariate analysis (with a single Gaussian) of TEM data corresponding to the evolution of ZnO NPs average size versus aging time before hydrolysis (from 1 to 24 hours). See also Figure III.5 for corresponding 2D plots. The lines are just guides for the eyes.

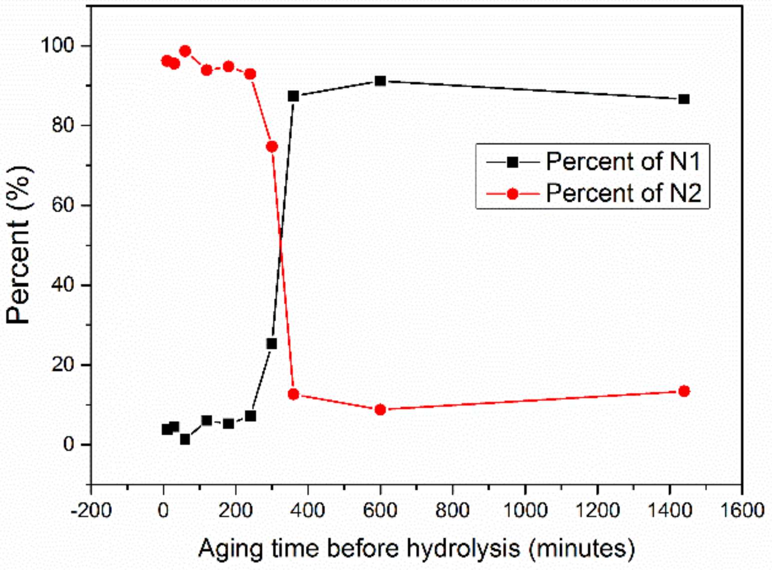

Figure III.7. Percentage (deduced from a multivariate analysis) of the two populations N1(isotropic NPs) and N2 (anisotropic NPs)depending on the aging time before hydrolysis. See also Table III.6.

Moreover it has to be noted that a change of viscosity also occurred within the frame of hydrolysis process due to the interaction between ZnO NPs and alkylamine. Considering the timescale of the two previous mechanisms (few days for growth of nanorods and few hours for gelation), this one might compete during the formation of ZnO NPs.

II.2. Influence of the amount of water

We then studied the possibility to control the amount of water reaching the mixture of amine and zinc precursor. To avoid at maximum the observed gelation process, hydrolysis was initiated, in all following experiments, 10 minutes after mixing process. In a first set of experiments water feeding rate was controlled as depicted in Figure III.7 by using PTFE tubes of different length.

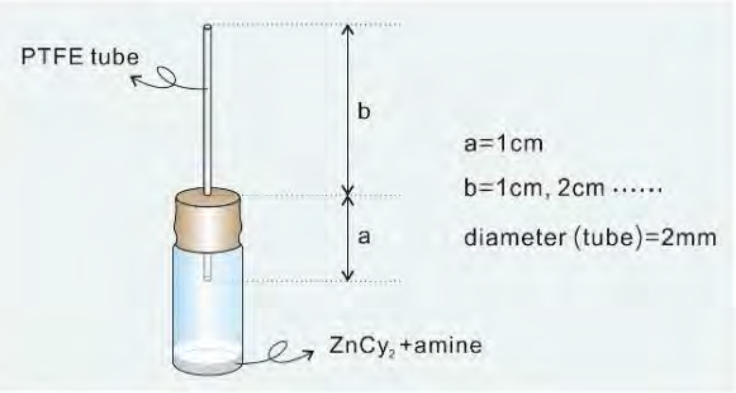

Figure III.8. Schematic illustration for the preparation of ZnO NPs depending on different length of tubes for hydrolysis.

As shown in Figure III.9, anisotropic NPs with mean length of 16.5±11.6 nm could be prepared if the vial without stopper was used. Interestingly, the length of the NPs decreased if longer tubes were used. For the longest 20 cm tube quasi isotropic 1.7±1.1

nm ZnO NPs were thus obtained. Decreasing the feeding rate of water favored the gelation process to occur, and prevents the formation of anisotropic NPs (see Figure III.10, Table III.7 and III.8). As expected, the same tendency is observed when the diameter of the PTFE tube was increased from 2 mm to 4 mm (see Figure III.11 and III.12, as well as the corresponding Tables III.9 and III.10). Nevertheless, for a given length, longer NPs were obtained with larger tube. The latter increase the amount of water reaching per unit of time the reactive medium such that growing process occurred more rapidly than gelation process.

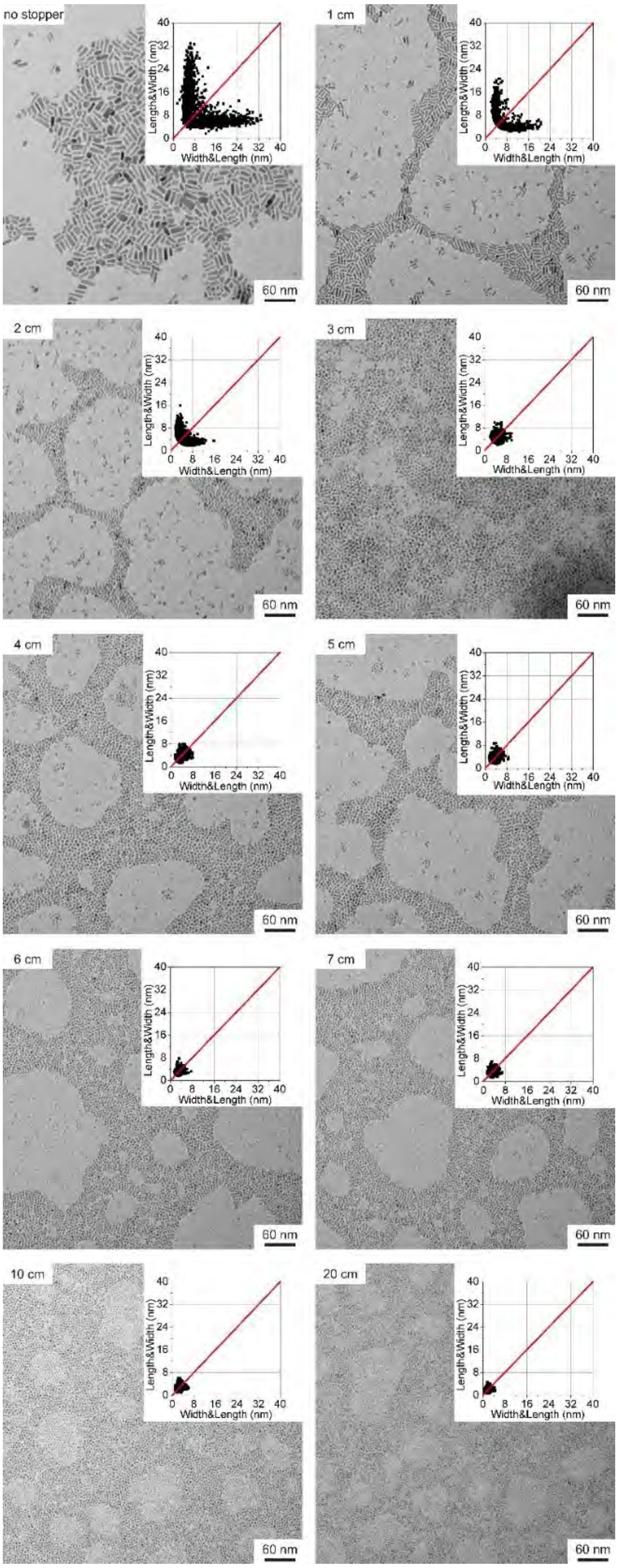

Figure III.9. TEM images and 2D size plots of the ZnO/2DDA NPs *versus* length tube (diameter 2 mm).

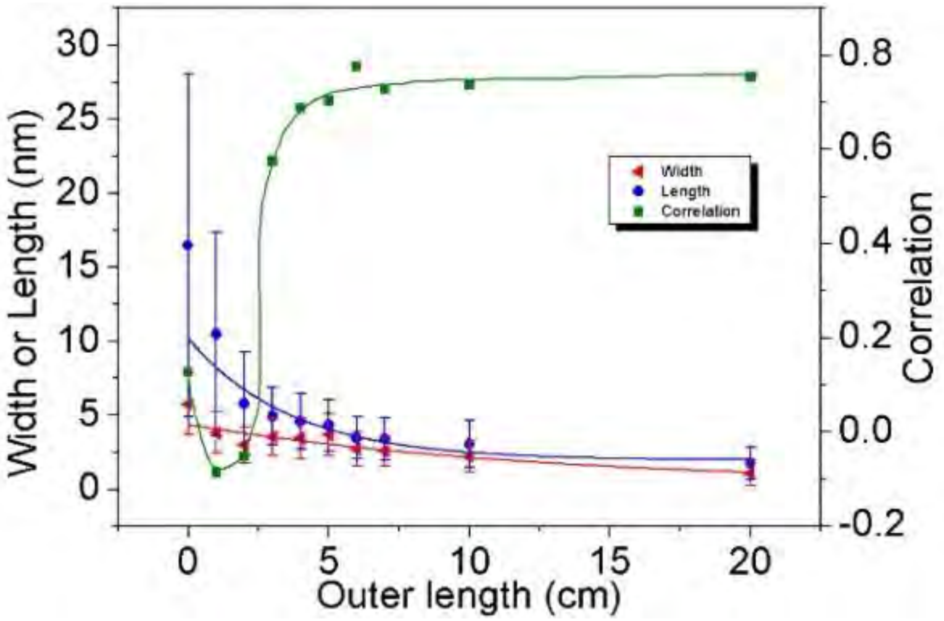

Figure III.10. Mean width (red), mean length (blue) and corresponding correlation (green) obtained from a multivariate analysis (with a single Gaussian) of the TEM pictures of Figure III.8. The red, blue and green line depicts the mean width, mean length and corresponding correlation respectively. The lines are just guides for the eye.

Outer length of the	Length (nm)	Width (nm)	correlation
no stopper	16.5 ± 11.6	6.1 ± 2.8	0.13
1	10.5 ± 6.9	4.1 ± 1.8	-0.09
2	5.8 ± 3.5	3.1 ± 1.3	-0.05
3	4.9 ± 1.9	3.7 ± 1.4	0.58
4	4.6 ± 1.9	3.5 ± 1.5	0.69
5	4.3 ± 1.8	3.4 ± 1.4	0.70
6	3.5 ± 1.4	2.8 ± 1.1	0.78
7	3.4 ± 1.4	2.7 ± 1.1	0.73
10	3.0 ± 1.6	2.2 ± 1.1	0.74
20	1.7 ± 1.1	1.1 ± 0.8	0.75

Table III.7. Multivariate analysis of the 2D plots corresponding to the TEM images of the Figure III.8 through Rmixmod program (the dispersion is given as twice the standard deviation obtained from calculations, and number of cluster was set to 1).

Outer length of the tube (cm)	Length (nm)	Width (nm)	Population Weight (%)	correlation
no stopper	17.5 ± 11.5	5.8 ± 2.1	81.8	0.35
	11.9 ± 6.7	7.4 ± 4.2	18.2	0.55
1	9.9 ± 6.0	3.9 ± 1.3	84.9	-0.38
	13.6 ± 7.9	5.2 ± 2.6	15.1	-0.38
2	6.6 ± 3.3	3.1 ± 1.5	66.8	-0.05
	4.3 ± 0.9	3.1 ± 0.8	33.2	0.06
3	4.5 ± 1.2	3.6 ± 1.1	67.7	0.56
	5.8 ± 2.1	3.9 ± 1.9	32.3	0.51
4	4.4 ± 1.7	3.6 ± 1.5	75.7	0.88
	5.1 ± 1.9	3.3 ± 1.3	24.3	0.58
5	4.1 ± 1.4	3.4 ± 1.3	74.3	0.88
	4.9 ± 2.1	3.4 ± 1.6	25.7	0.63
6	3.2 ± 1.00	2.7 ± 0.9	68.4	0.86
	4.1 ± 1.4	3.1 ± 1.2	31.6	0.63
7	3.2 ± 1.0	2.6 ± 0.9	75.6	0.81
	4.2 ± 1.6	2.9 ± 1.4	24.4	0.62
10	2.7 ± 1.1	2.1 ± 1.0	73.6	0.82
	3.9 ± 1.3	2.5 ± 0.9	26.4	0.42
20	1.5 ± 0.5	0.9 ± 0.3	68.5	-0.14
	2.3 ± 1.2	1.5 ± 0.9	31.5	0.68

Table III.8. Multivariate analysis of the 2D plots corresponding to the TEM images of the Figure III.8 through Rmixmod program (the dispersion is given as twice the standard deviation obtained from calculations, and number of cluster was set to 2).

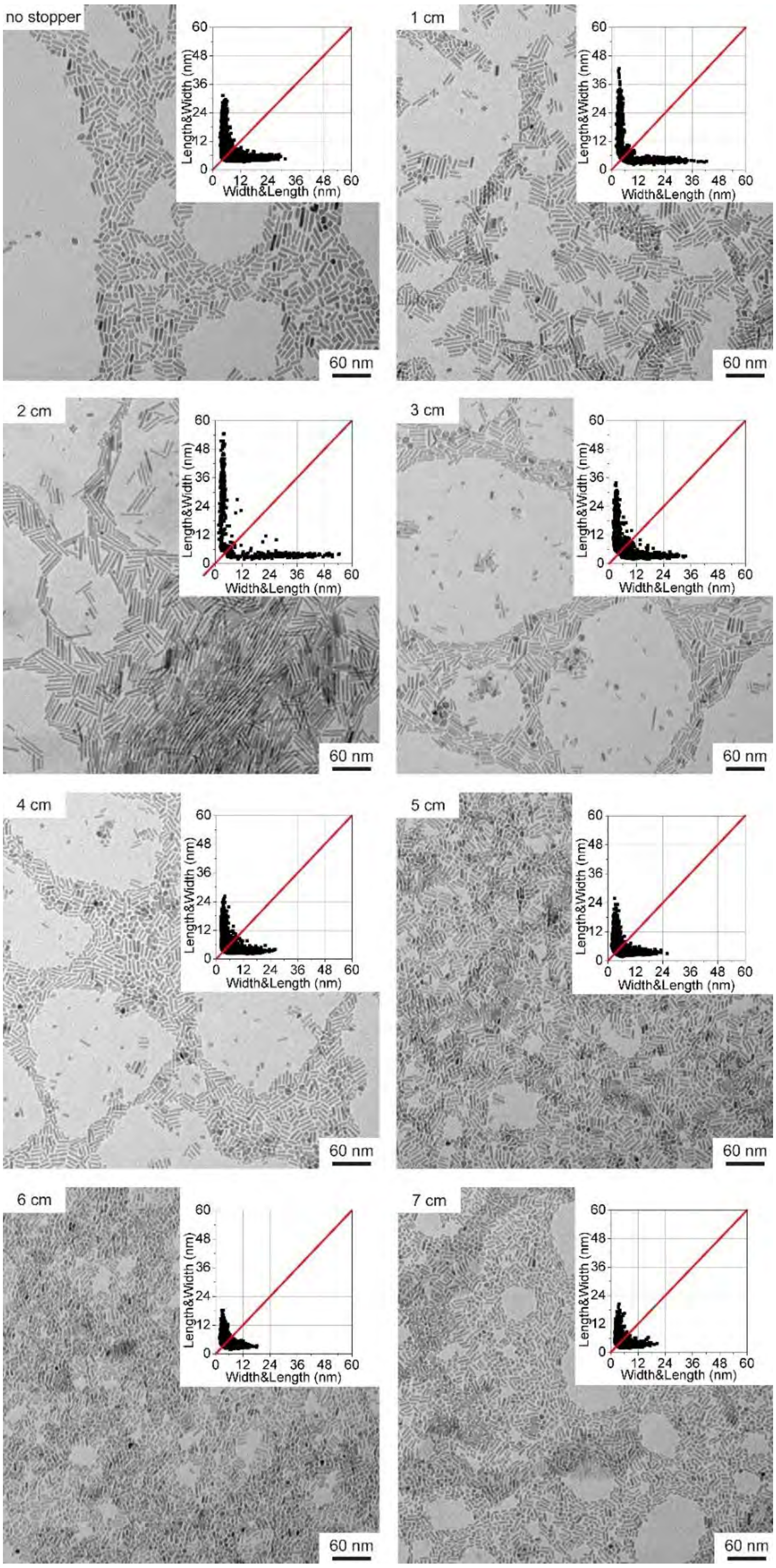

Figure III.11. TEM images and 2D size plots of the ZnO/2DDA NPs *versus* length tube (diameter 4 mm).

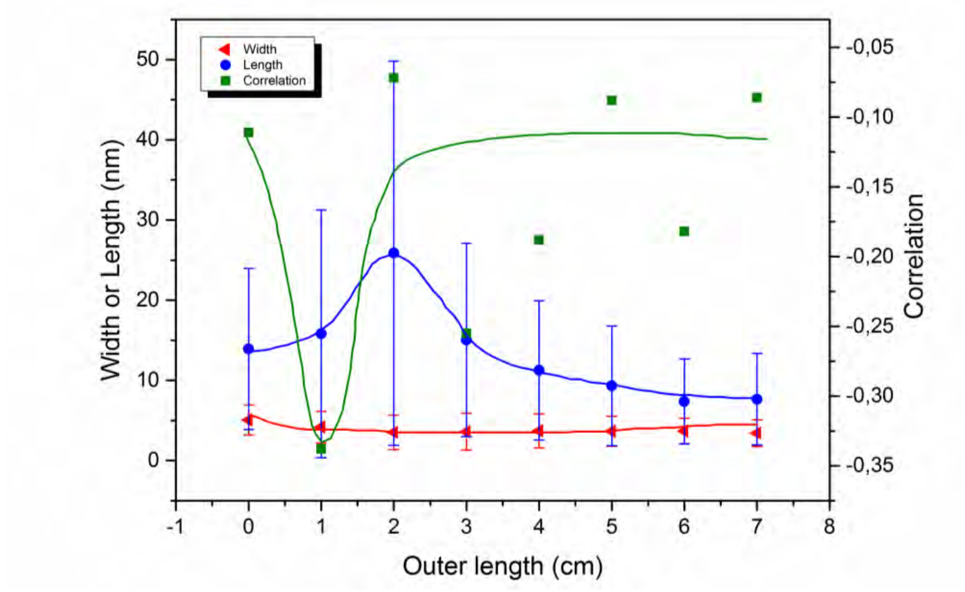

Figure III.12. Mean length (blue), mean width (red) and corresponding correlation (green) issued from a multivariate analysis (with a single Gaussian) of data corresponding to ZnO/2DDA NPs versus different size of PTFE tube (4 mm diameter, exposed to the air for 1 week, see Figure III.10). The lines are just guide for the eyes.

Outer length of the tube (cm)	Length (nm)	Width (nm)	Correlation
no stopper	13.9 ± 10.0	5.1 ± 1.8	-0.11
1 cm	15.8 ± 15.4	4.2 ± 2.0	-0.34
2 cm	25.9 ± 24.0	3.5 ± 2.1	-0.07
3 cm	15.0 ± 12.0	3.6 ± 2.3	-0.25
4 cm	11.2 ± 8.7	3.7 ± 2.1	-0.19
5 cm	9.3 ± 7.4	3.6 ± 1.9	-0.09
6 cm	7.4 ± 5.3	3.7 ± 1.6	-0.18
7 cm	7.6 ± 5.7	3.4 ± 1.7	-0.09

Table III.9. Multivariate analysis of the 2D plots corresponding to the TEM images of the Figure III.10 through Rmixmod program (the dispersion is given as twice the standard deviation obtained from calculations, and number of cluster was set to 1).

Outer length of the tube (cm)	Length (nm)	Width (nm)	Population Weight (%)	correlation
no stopper	15.4 ± 9.8	4.8 ± 1.2	75.0	0.24
	9.6 ± 4.1	5.9 ± 2.3	25.0	0.35
1	18.1 ± 14.1	3.8 ± 1.3	79.2	0.06
	7.1 ± 2.4	5.5 ± 2.1	20.8	0.61
2	28.0 ± 21.8	3.3 ± 1.2	88.6	0.34
	9.3 ± 10.7	5.3 ± 3.9	11.4	0.78
3	17.0 ± 11.4	3.2 ± 1.2	73.2	0.09
	9.8 ± 6.0	4.7 ± 3.0	26.8	0.15
4	12.4 ± 8.1	3.4 ± 1.3	80.0	0.10
	6.8 ± 3.7	5.0 ± 2.7	20.0	0.78
5	10.9 ± 7.0	3.4 ± 1.4	66.6	0.19
	6.1 ± 2.3	4.1 ± 2.2	33.4	0.50
6	8.7 ± 5.3	3.3 ± 1.2	58.7	0.12
	5.5 ± 1.9	4.2 ± 1.5	41.3	0.69
7	8.9 ± 5.6	3.1 ± 1.3	63.9	0.28
	5.4 ± 2.0	4.0 ± 1.7	36.1	0.66

Table III.10. Multivariate analysis of the 2D plots corresponding to the TEM images of the Figure III.10 through Rmixmod program (the dispersion is given as twice the standard deviation obtained from calculations, and number of cluster was set to 2).

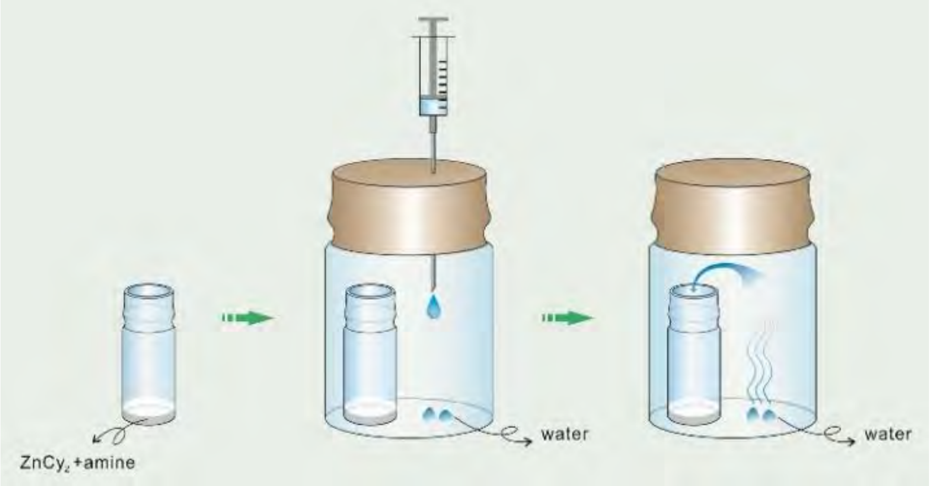

Scheme 1. Schematic illustration for the preparation of ZnO NPs depending on different equivalent of water.

To go one step further, the amount of water introduced in the vessel is varied from 2 eq. up to 100 eq. as depicted in Scheme 1 and Figure III.13 (see also Tables III.11 and III.12). Increasing the amount of introduced water leads to a decrease of the NPs aspect ratio. In the case of NPs stabilized by 2 eq. OA, the 2D plots reveal a distribution of size where the width is more or less constant (ca 5 nm) and the length of the NPs is spread over the 5-65 nm range (see Figure III.13, Tables III.11 and III.12). The average aspect ratio is close to 8.2 ± 8.6 corresponding to a θ angle close to 83° and a total de-correlation between the two axes of the particles are obtained. As the amount of water increases, the 2D plot exhibits less and less extended length range, the points cloud is more and more focused around the median line which is characteristic of a decrease of the aspect ratio. Especially for more than 8 eq. of water, the width of the NPs increases from 5 nm up to 7 nm (see Figure III.14). Interestingly, the number of isotropic nanoparticles is increasing as the amount of water increases (see Figure III.15). This result suggests that large amount of water favors multi-nucleation. As the quantity of zinc precursor is the same for all the experiments (0.025 mmol), multi-nucleation competes with growth and consequently, aspect ratio decreases.

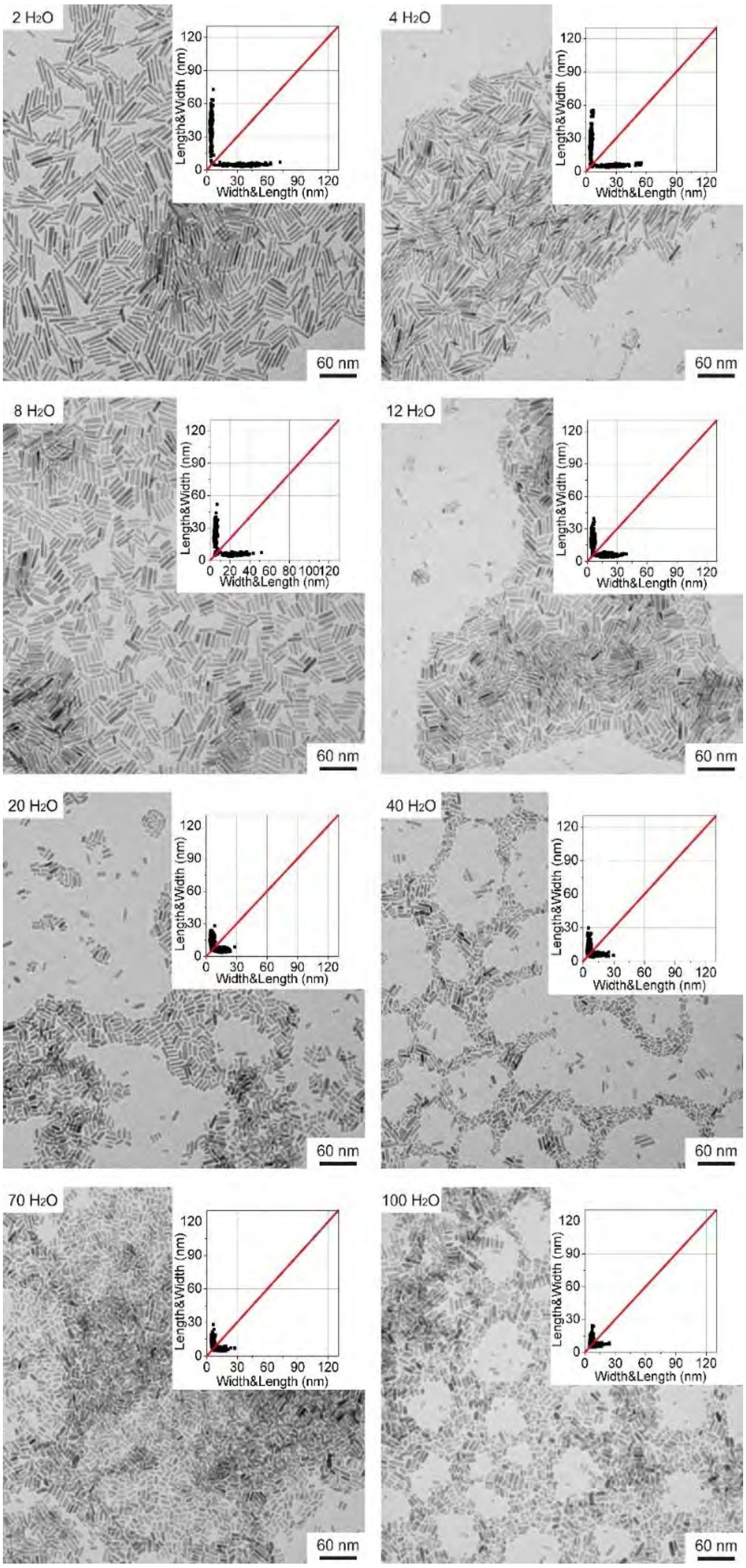

Figure III.13. TEM picture and 2D size plots of ZnO NPs prepared in the presence of 2 eq. OA for different amounts of water.

Equivalent of H_2O	Length (nm)	Width (nm)	Population Weight (%)	Correlation
2	36.4 ± 10.8	4.3 ± 0.9	69.3	0.33
	37.2 ± 29.3	4.8 ± 1.5	30.7	0.22
4	25.1 ± 10.1	4.6 ± 0.8	61.1	0.20
	20.8 ± 21.3	5.5 ± 1.3	38.9	0.47
8	24.0 ± 8.6	4.9 ± 1.1	59.3	0.34
	24.8 ± 17.4	5.8 ± 1.6	40.7	0.23
12	18.1 ± 7.9	5.4 ± 1.4	82.7	-0.10
	23.0 ± 13.0	6.6 ± 1.8	17.3	-0.38
20	15.0 ± 6.7	5.8 ± 1.7	100.0	0.07
	----	----	----	----
40	8.9 ± 3.4	5.5 ± 1.3	63.8	-0.06
	15.9 ± 8.9	6.0 ± 1.7	36.2	-0.09
70	11.2 ± 3.3	5.9 ± 1.1	74.9	0.21
	14.5 ± 7.4	6.4 ± 2.0	25.1	-0.09
100	10.4 ± 4.6	6.1 ± 1.1	82.5	0.28
	13.9 ± 6.8	7.5 ± 1.1	17.4	-0.03

Table III.11. Multivariate analysis of the 2D plots corresponding to the TEM images of the Figure III.12 through Rmixmod program (the dispersion is given as twice the standard deviation obtained from calculations, and number of cluster was set to 2).

Equivalent of H_2O	Length (nm)	Width (nm)	Correlation
2	36.6 ± 10.8	4.5 ± 1.3	0.25
4	25.8 ± 15.5	5.0 ± 1.3	0.35
8	24.3 ± 12.9	5.3 ± 1.6	0.26
12	18.9 ± 9.7	5.6 ± 1.7	0.05
20	15.0 ± 6.7	5.8 ± 1.7	0.07
40	11.4 ± 9.1	5.7 ± 1.5	0.16
70	12.0 ± 5.5	6.0 ± 1.4	0.18
100	11.0 ± 5.8	6.3 ± 1.6	0.46

Table III.12. Multivariate analysis of the 2D plots corresponding to the TEM images of the Figure III.12 through Rmixmod program (the dispersion is given as twice the standard deviation obtained from calculations, and number of cluster was set to 1).

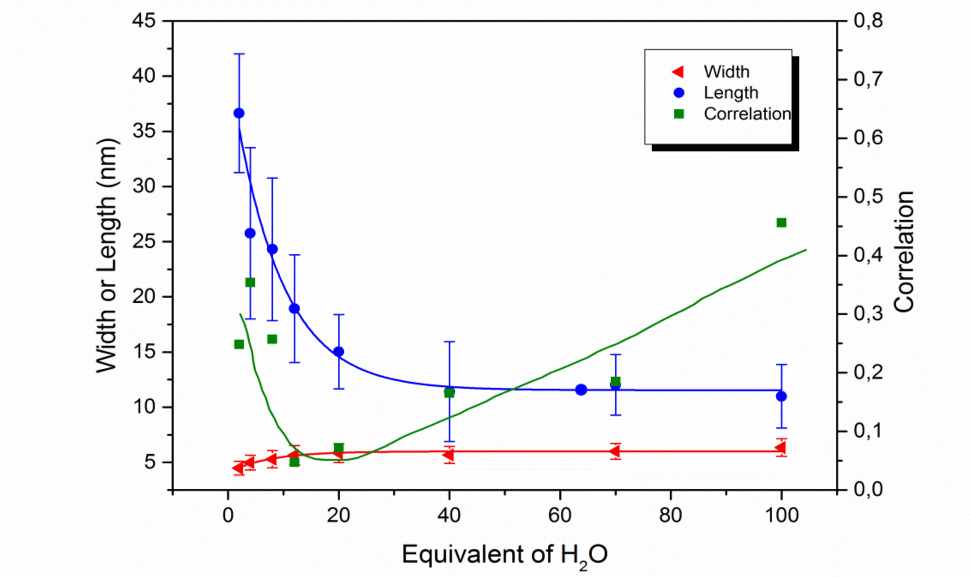

Figure III.14. Mean width (red), mean length (blue) and corresponding correlation (green) issued from a multivariate analysis (with a single Gaussian) of data corresponding to ZnO NPs prepared in the presence of 2 eq. OA versus equivalent of water. The lines are just guides for the eyes. See also Figure III.12.

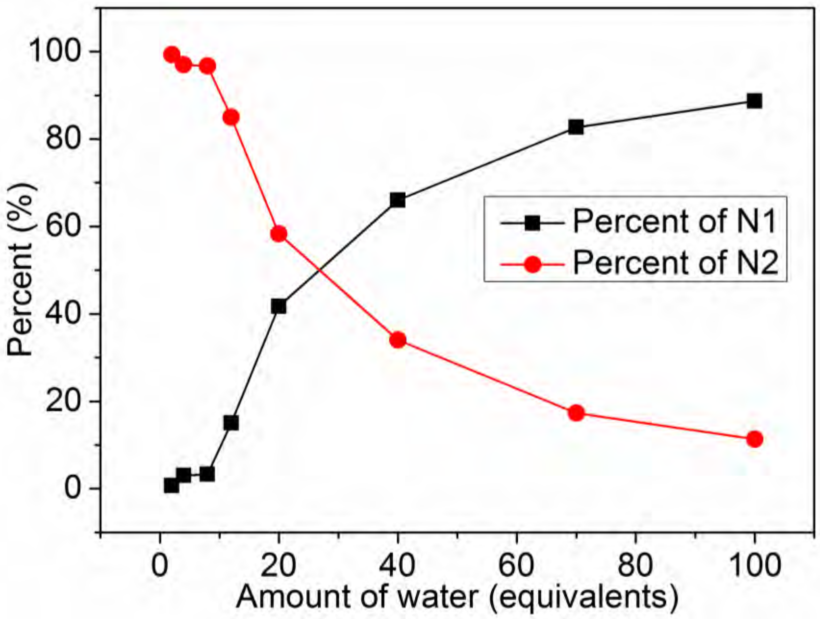

Figure III.15. Percentage (deduced from a multivariate analysis) of the two populations N1(isotropic NPs) and N2 (anisotropic NPs) depending on the amount of water. The data corresponds to ZnO NPs prepared in the presence of 2 eq. OA. Similar results are obtained when the NPs are prepared using DDA instead of OA (see for example Figure III.16, Figure III.17, and Figure III.18).

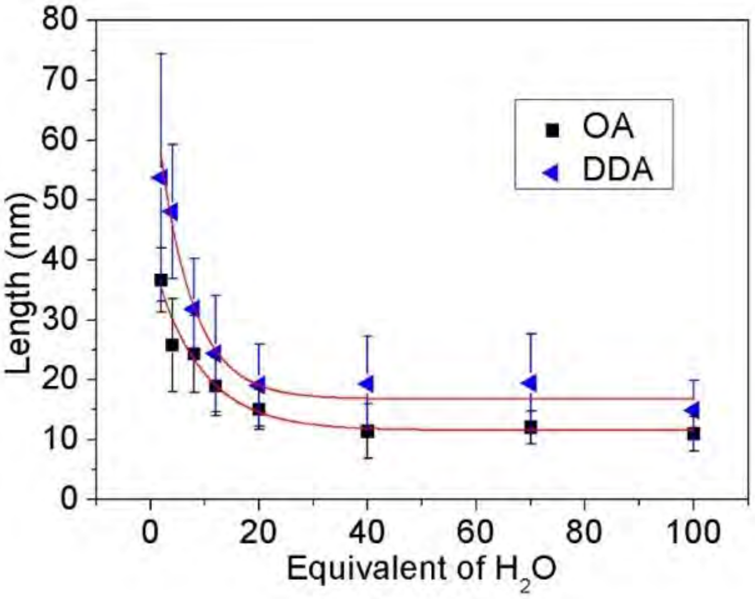

Figure III.16. Comparison of the average length of NPs prepared in the presence of 2 eq. OA or DDA depending on the amount of water.

These results highlight that the water amount is much more important than the length of the alkyl chain of the amine ligand on the aspect ratio of the NPs. However, significant differences can be observed when the NPs are prepared in the presence of OA or DDA. While the width of the nanorods is similar regardless of the ligand, the aspect ratio is much more important when DDA is used instead of OA. The length of the NPs ranges from 5 to 65 and 15 to 100 nm for OA and DDA, respectively. Another important difference is the absence of isotropic NPs for 2 and 4 eq. of water in the presence of DDA. This suggests that the kinetic of growth by oriented attachment is faster with DDA than with OA.

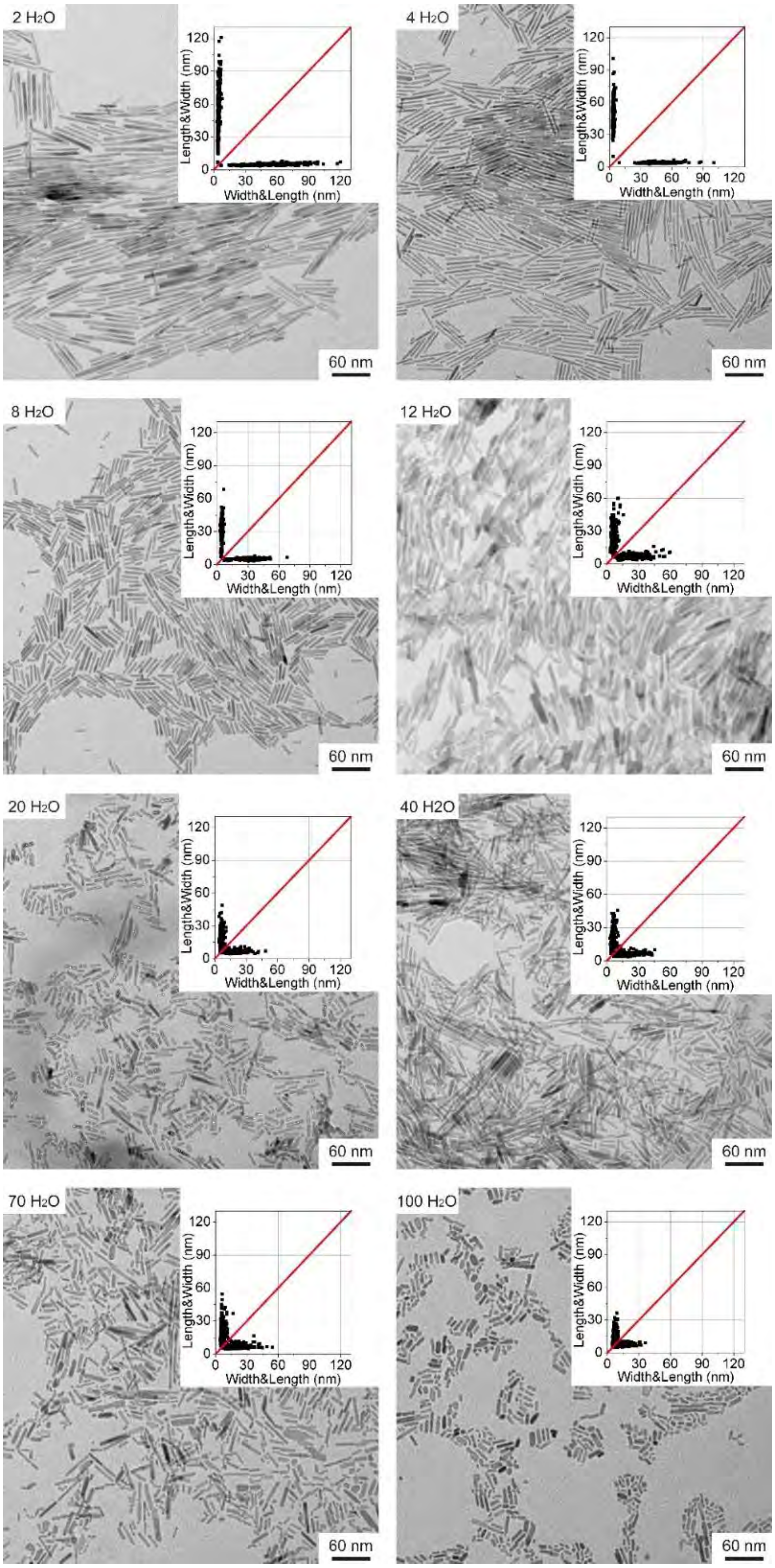

Figure III.17. TEM picture and 2D size plots of ZnO NPs prepared in the presence of 2 eq. DDA for different amounts of water. See corresponding Tables III.13 and III.14.

Equivalent of H_2O	Length (nm)	Width (nm)	Population Weight (%)	Correlation
2	48.3 ± 34.5	4.5 ± 1.0	77.1	0.36
	72.2 ± 40.8	5.6 ± 1.8	22.9	0.27
4	46.0 ± 17.6	3.8 ± 0.8	79.0	0.04
	56.1 ± 29.9	4.5 ± 1.3	21.0	0.02
8	32.6 ± 11.5	4.5 ± 0.6	52.0	0.06
	31.1 ± 20.8	5.1 ± 1.4	48.0	0.35
12	24.1 ± 18.3	5.7 ± 2.0	73.8	0.32
	25.1 ± 22.1	8.4 ± 3.9	26.2	0.58
20	16.9 ± 10.1	5.9 ± 1.3	66.9	0.03
	23.4 ± 15.3	7.2 ± 2.6	33.1	-0.24
40	16.8 ± 10.8	5.5 ± 1.8	79.0	0.27
	28.7 ± 17.2	7.4 ± 3.3	21.0	-0.31
70	15.7 ± 9.7	5.7 ± 1.3	53.9	0.14
	23.9 ± 18.3	7.6 ± 3.7	46.1	-0.20
100	12.7 ± 6.2	6.7 ± 1.6	59.1	0.08
	18.1 ± 10.8	8.1 ± 2.3	40.9	-0.05

Table III.13. Multivariate analysis of the 2D plots corresponding to the TEM images of the Figure III.16 through Rmixmod program (the dispersion is given as twice the standard deviation obtained from calculations, and number of cluster was set to 2).

Equivalent of H_2O	Length (nm)	Width (nm)	Correlation
2	53.8 ± 41.2	4.8 ± 1.5	0.51
4	48.1 ± 22.3	4.0 ± 1.1	0.21
8	31.9 ± 16.7	4.8 ± 1.2	0.21
12	24.4 ± 19.4	6.4 ± 3.5	0.35
20	19.1 ± 13.5	6.4 ± 2.2	0.15
40	19.3 ± 15.7	5.9 ± 2.6	0.36
70	19.5 ± 16.5	6.6 ± 3.3	0.18
100	14.9 ± 9.9	7.3 ± 2.3	0.31

Table S12. Multivariate analysis of the 2D plots corresponding to the TEM images of the Figure III.16 through Rmixmod program (the dispersion is given as twice the standard deviation obtained from calculations, and number of cluster was set to 1).

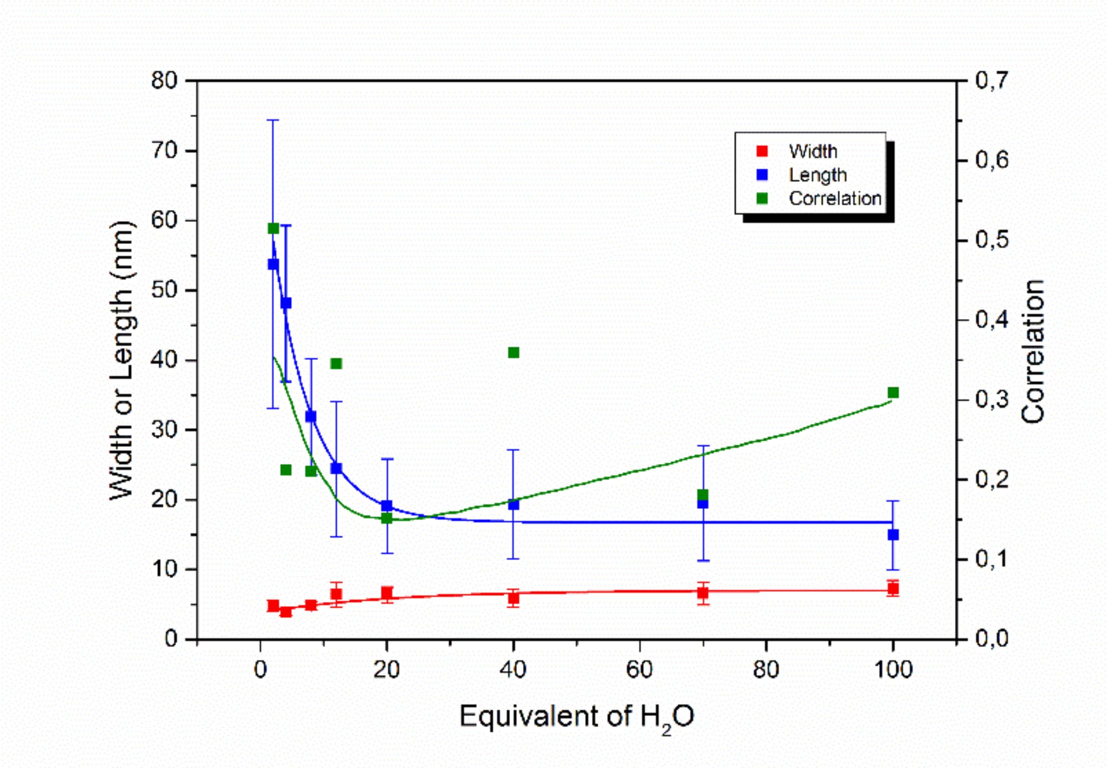

Figure III.18: Mean width (red), mean length (blue) and corresponding correlation (green) issued from a multivariate analysis (with a single Gaussian) of data corresponding to ZnO NPs prepared in the presence of 2 eq. DDA *versus* the equivalents of water. The lines are just guides for the eyes. See also Figure III.16.

Conclusion

In summary, we demonstrated that the size of the ZnO NPs could be adjusted by controlling the hydrolysis rate, the aging time before hydrolysis, the nature of ligand and the amount of water. Growing mechanism occurred through an oriented attachment process, and is eventually hampered by gelation process induced by interaction of zinc precursor or ZnO NPs with amine ligands. The gathered results can help us understand the correlation between those parameters and the morphology of the NPs, which could strongly affect the versatile properties of the ZnO NPs.

Finally, the gelification process detected in the previous experiments will be fully described and analyzed in the following chapter.

References

[1]. M. Monge, M. L. Kahn, A. Maisonnat, B. Chaudret, *Angew. Chem. Inter. Ed.* **2003**, *42*, 5321-5324.

[2]. M. L. Kahn, M. Monge, V. Collière, F. Senocq, A. Maisonnat, B. Chaudret, *Adv. Funct. Mater.* **2005**, *15*, 458-468.

[3]. M. L. Kahn, A. Glaria, C. Pages, M. Monge, L. Saint Macary, A. Maisonnat, B. Chaudret, *J. Mater. Chem.* **2009**, *19*, 4044 – 4060.

[4]. Z. Zheng, R. Butynska, C. Valverde Serrano, J. D. Marty, C. Mingotaud, M. L. Kahn. *Chem. Eur. J.* **2016**, *22*, 15614-15618.

Chapitre IV

Nouvelle approche vers des matériaux hybrides organique-inorganique

Résumé

Dans ce chapitre, nous proposons une approche originale pour obtenir des matériaux hybrides pouvant être mis en forme et remodelés. Nous démontrons sans équivoque la formation de structures oligomériques dans le mélange constitué d'amine primaire à longue chaine alkyl avec des composés organométalliques. Nous avons montré que dans le cas du zinc, des oligomères de type Zn-amido, structures rarement rapportées dans la bibliographie par rapport aux oligomères bien connus de type Zn-amine, sont obtenues. Cette réaction d'oligomérisation entre les centres métalliques induit la formation d'un gel qui peut être transformé en fibres, en motifs estampés ou en pièces moulées. Enfin, les matériaux hybrides d'oxyde métallique sont obtenus simplement par hydrolyse du gel organométallique. Cette voie originale vers des matériaux hybrides facilement transformables a été démontrée pour l'oxyde de zinc et étendue à d'autres oxydes métalliques tels que l'oxyde d'étain et l'oxyde de fer, ce qui prouve l'universalité de la méthode.

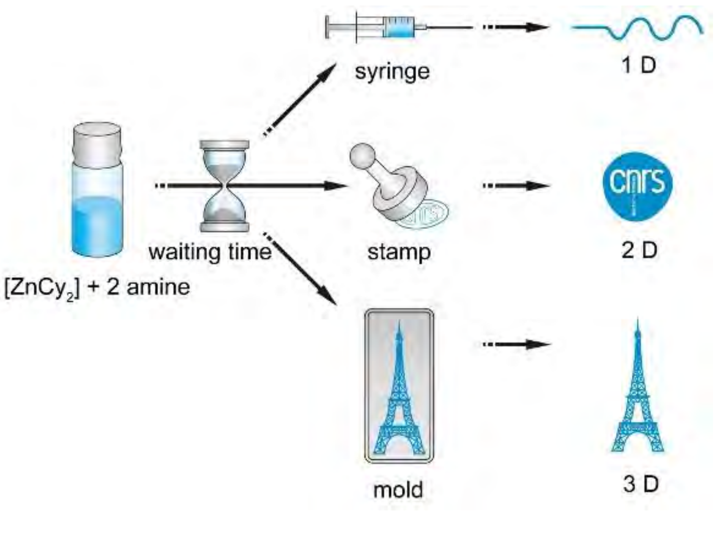

Contenu

Introduction

Metal oxides possess quite unique and peculiar properties in optics, electronic, catalysis etc...[1] This has stimulated the development of numerous synthetic pathways towards materials with well-controlled sizes and shapes.[2-7] One well developed approach giving rise to such materials is the “sol-gel” method which starts from metal alkoxides or metal salts in aqueous solutions and involves their controlled hydrolysis and condensation yielding metal oxides. Processing of the gel or of the “sol” opens many opportunities to shape the ultimate material,[8, 9] a route extensively applied to the preparation of thin films, organized 3D- and porous materials.[10-12] To extend the scope of this method to metal with unfavourable hydrolysis equilibria, a modified sol-gel process, namely polymerizable complex method also known as Pechini method[10, 13] has been developed. It involves small-molecule chelating ligands (typically a mixture of citrate and ethylene glycol) to form in a first step a homogeneous solution of metal/citrate complexes. Heating of this complex initiates a polyesterification reaction that enables the formation of an extended covalent polymer network from which, after combustion, inorganic materials are obtained. Both previous methods are mainly restricted to aqueous solutions and there is still a need to develop a non-aqueous equivalent to sol-gel chemistry. This is a prerequisite to extend sol gel chemistry to other synthetic strategies such as those involving organometallic precursors. The organometallic route applies to a large number of metal centres,[14] and simply involves the hydrolysis of the metal complexes in solution. It has been shown to efficiently lead to highly crystalline nanoparticles.[14, 15] Size and shape of the NPs are controlled during the hydrolysis step by the means of additional ligands such as fatty amines or fatty acids.[16]

Here, we propose an alternative approach for which the polymerization process (gel formation) is induced at room temperature by controlled coordination between metal centres and amine-containing ligands.

IV. 1. Gel formation

As a proof of principle a mixture of hexadecylamine (or shorter amine) and $[ZnCy_2]$ (in a ratio of 2 equivalents of amine per zinc precursor) was chosen without additional solvent.[17] A precedently undetected feature of this process is the large increase of the mixture viscosity with aging and prior to hydrolysis. Whereas both are solids at room temperature, admixture of $[ZnCy_2]$ and dodecylamine (DDA) (in the 1:2 molar ratio) under an inert atmosphere rapidly leads to a liquid phase with a low viscosity, evolving to a viscous mixture after a waiting time (t_w) of a few hours (t_w = 4-5 hours), eventually yielding a transparent gel or a glass-like solid for t_w > 8 hours (Figure IV.1a). Herein we disclose that this transient state can be exploited to shape the macroscopic organization of the forthcoming metal oxide material.

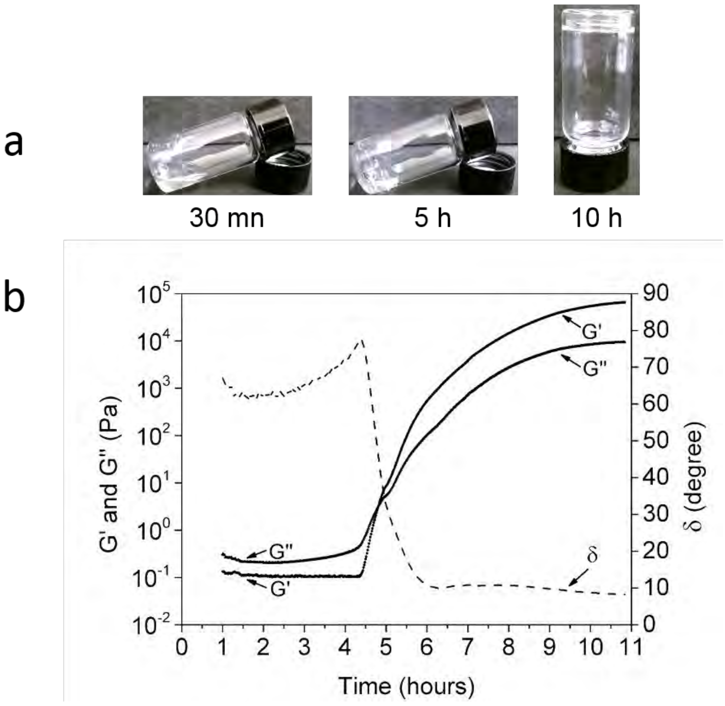

Figure IV. 1. (a) Visual aspect of the $[ZnCy_2]$/DDA (1:2) mixture under argon. The mixture under argon appears like: a liquid for a waiting time, t_w, of 30 minutes, a viscous liquid for t_w = 5 hours and a gel for a t_w = 10 hours. (b) Time dependence of the elastic modulus G', the viscous modulus G" and the phase angle, δ, between the stress and strain measured under sinusoidal stress (frequency 1 Hz) for the $[ZnCy_2]$/DDA (1:2) mixture under nitrogen. The origin of the time scale corresponds to the mixing process.

IV. 2. Rheology

Rheological measurements performed at 298 K under nitrogen revealed an abrupt increase of the elastic modulus, G', and the viscous modulus, G'', of more than 3 orders of magnitude for t_w = 5 h (Figure IV.1b). In addition, during this transition, the elastic modulus abruptly overrides the viscous modulus, which is a feature of the transition from a liquid to a hard gel or a solid-like material. This rheological study highlights the formation of an increasingly dense cross-linked network between t_w = 5 h and 12 h that becomes persistent after t_w = 8 h, in accordance with the macroscopic observation of a viscoelastic liquid for t_w = 5 h and a solid-like material for t_w = 8 h.

The modulus G' and G'' were measured by applying a sinusoidal stress to the sample, at the frequency of 1 Hz, and the resulting sinusoidal strain was recorded. Because of the very large change in viscosity during the experiment, the stress applied had to be adapted. A stress amplitude of 20 Pa was applied from 0 to 6 hours of measurement. And a stress amplitude of 1000 Pa was applied from 6 to 9h45 hours of measurement.

The measurement was started 1h after the preparation of the reactive mixture. On the data plot, an increment of 1h (with no points) was thus applied. The mixture was prepared in a glove box under argon, and after 1h of rest under inert atmosphere, the mixture was injected within the rheometer plates' gap. The visual aspect of the mixture was checked from time to time. The mixture within the gap remained transparent all over the experiment. At the end of the experiment, the gap was still adequately filled. The resulting fluid was still transparent, a bit yellowish and a bit glassy. It quickly turned more plastic then white when exposed to air.

With the same preparation of the sample in the gap, a series of frequency sweep measurements has been performed with time (time after mixing). The sinusoidal stress amplitude is set at 0.5 Pa at 4.92 h; 1 Pa from 5.08 to 7.0 h; 20 Pa from 7.0 to 7.83 h; 200 Pa at 8.16 h; 1000 Pa from 8.85 to 12.4 h. The frequency sweep was 10 Hz-0.1 Hz from 4.92 to 5.33 h; 10 Hz-0.02 Hz from 5.5 to 7.0 h, 10 Hz-0.01 Hz from 7.5 to 7.83 h; 10 Hz-0.005 Hz from 8.16 to 8.85 h; 10 Hz-0.001 Hz from 9.6 to 12.4 h. This stepwise increase of the frequency range has been selected in order to monitor conveniently the fast changes at the beginning of the experiment, and then to catch the cross-over frequency as it moved to lower frequencies at longer experiment times, when the mixture gelled.

The gelation has been monitored by registering the changes of G' and G" with a sinusoidal stress amplitude comprised between 20-1000Pa, at a frequency of 1 Hz, from 1 to 11 hours after mixing [$ZnCy_2$] with 2 DDA (Figure IV.1). Up to 4.5 h after mixture, both moduli are low (viscous modulus G"≈0.5Pa; elastic modulus G' ≈ 0.1 Pa). At this stage, the fact that both the moduli are low and the viscous modulus G" is larger than the elastic modulus G’ features a liquid state. An abrupt increase of G' (from 0.1 Pa to 1 kPa, 4 order of magnitude) and G" (from 0.5 Pa to 500 Pa, three order of magnitude) is measured between 4h30 and 6 h of waiting time, which quantifies the increase of the viscosity. During this transition, G' becomes higher than G", which is well showed by the abrupt decrease of the dephasing (δ). It evidenced the change in the viscoelasticity of the sample, with the elastic behaviour becoming predominant. This highlights the formation of a network, which keeps on increase its cross-linking density with time.

In order to get more information on the formation of this network, the variation of G' and G" over a larger range of frequency has been monitored, from ≈ 5 h to ≈ 12 h after mixing. From these frequency sweep measurements (Figure IV.2.), it can be seen that progressively, the G' curves went over the G" curves on an increasing range of frequency, demonstrating the transition from a liquid to a viscoelastic liquid then to a gel-like behaviour.

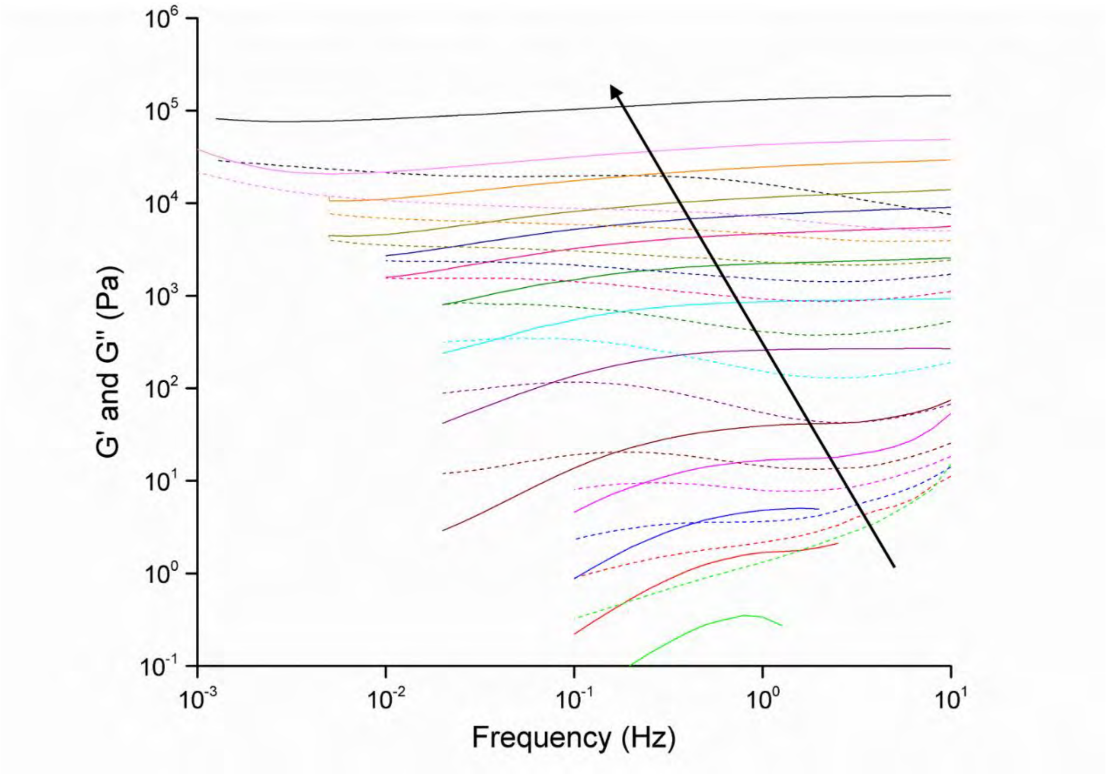

Figure IV.2. Frequency dependency of the elastic modulus G’ and the viscous modulus G" of the mixture [ZnCy$_2$]/DDA (1:2) kept under nitrogen gas after various aging time. Solid line: G’. Dashed line: G’’. The arrow indicates the increasing waiting time, in hours, by color set from the light green curves (4.92 h) to the black curves (12.4 h): 4.92, 5.08, 5.17, 5.33, 5.5, 6.0, 6.5, 7.0, 7.5, 7.83, 8.16, 8.85, 9.6 and 12.4. The cross-over frequency is defined as the frequency at which G' = G", for each set of G'/G" curves, and can be observed from 5.17 h (marine blue curves) to 8.16 h (olive green curves). Above ca 8.5 – 9 h, G’ and G’’ does not cross anymore in the range of frequency studied (10-0.001 Hz) (see also Figure IV.3) indicating the presence of longer clusters with persistent entanglements.

After 8.5 h of waiting time, G’ and G’’ do not cross over anymore, and both moduli reached a plateau of high stress (around 5.10^4 Pa for G" and 10^5 Pa for G') which is characteristic of a hard gel. Since the cross-over frequency of G' and G" ($f_{G'=G''}$) is related to the lifetime of entanglements, the decrease of $f_{G'=G''}$ with time also enables to monitor the progression of cross-linking quite precisely, up to the formation of the infinite covalent network (Figure IV.3). The lower the cross-over frequency, the higher is the cross-links density and persistence. Interestingly, the gelation process was slow enough to be monitored by conventional oscillatory rheology up to 4 decades of frequency.

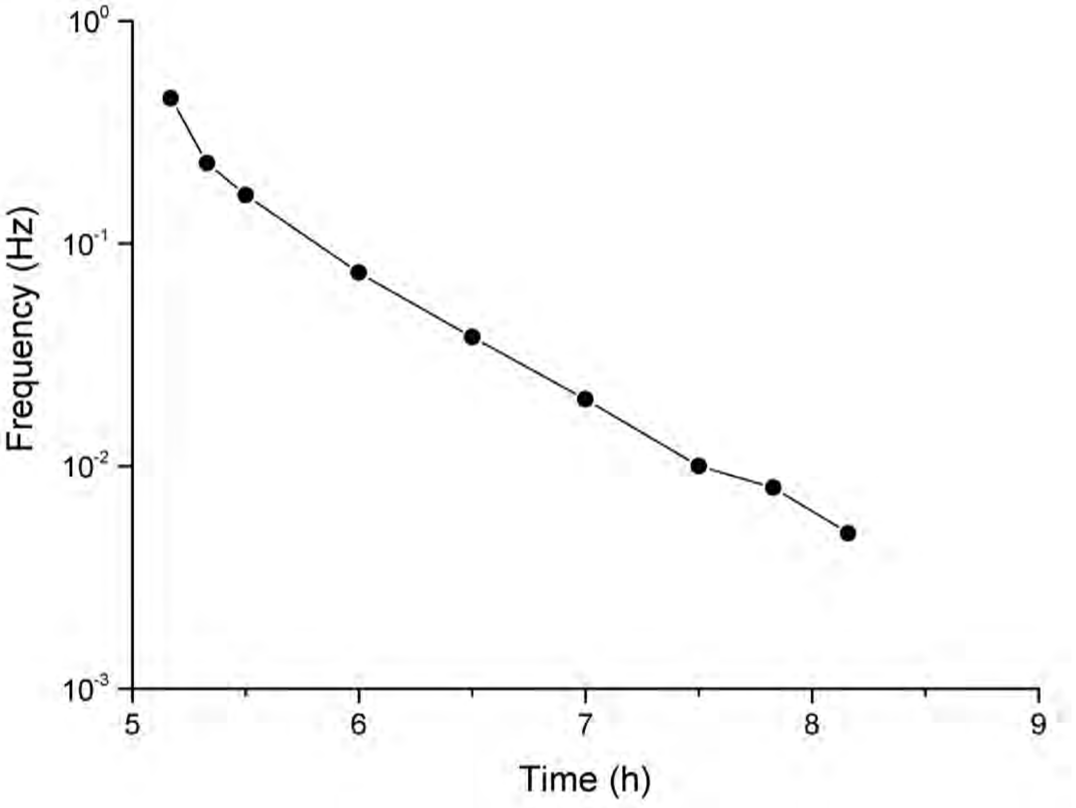

Figure IV.3 Frequency of G'/G'' crossover point ($f_{G'=G''}$) depending on the aging time. Above ca 8.5-9 h, the crossover could not be measured (too low) and/or did not exist anymore

The critical gelation point can be defined as the point at which G"/G'=tan(delta) is independent on the frequency, namely the cross-over point of the curves tan(δ) = f(t) plotted for the different frequencies[17, 18]. No crossover of the curves could be obtained within the duration of the experiment, but extrapolation at higher time provides a cross point between 14-15 h for frequencies between 0.001 and 1 Hz. The gelation point of the mixture, which corresponds to the formation of the infinite permanent network (bond percolation) can thus be estimated around 14-15 h.

IV. 3. Structure characterization

It has been reported that a 1:1 adduct, [$H_2RN \rightarrow ZnCy_2$], is formed in solution between [$ZnCy_2$] and DDA.[19] However such an adduct cannot explain the above rheological properties.

IV. 3. 1 NMR studies

In situ liquid and solid state NMR studies revealed that, over time, the amines are actually deprotonated yielding amido ligands which are able to bridge the zinc ions and thus favour the formation of oligomeric [$Zn(NHR)_2$]$_n$ structures.

Liquid state NMR spectroscopic study

^{1}H and ^{13}C NMR preliminary experiments were performed on a [$ZnCy_2$]/DDA (1:2) mixture solubilized in toluene-d_8. Figure IV.4 shows the ^{1}H NMR spectra of DDA, [$ZnCy_2$], and the [$ZnCy_2$]/DDA (1:2) mixture just after the mixing of the two compounds.

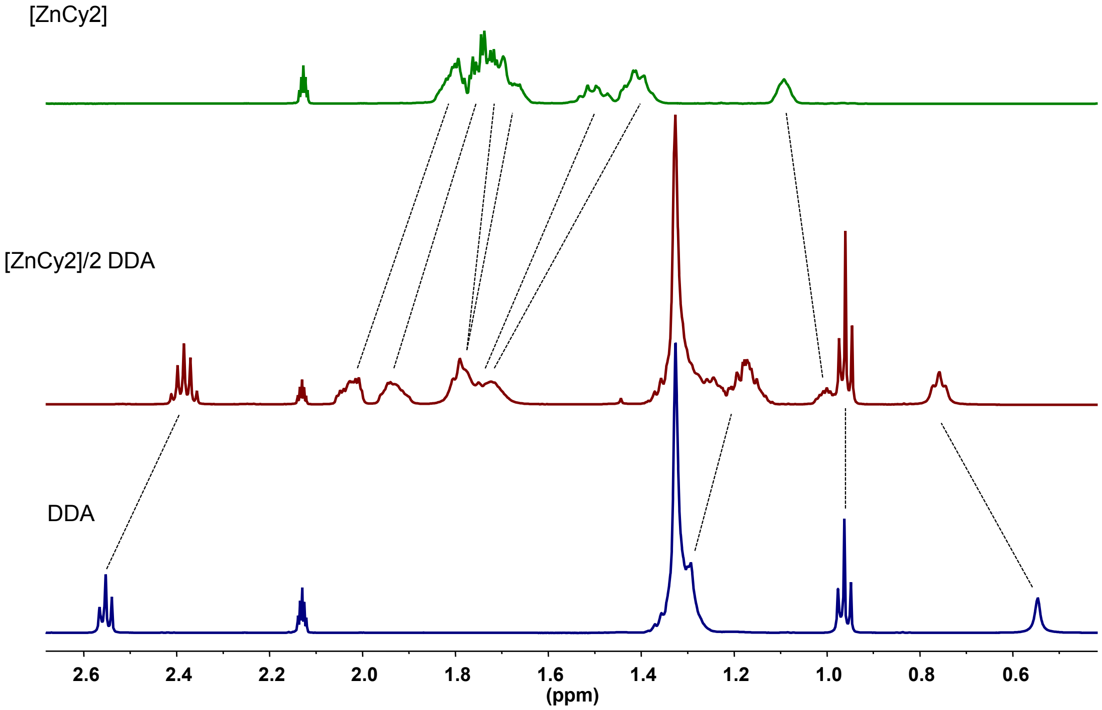

Figure IV.4 ^{1}H NMR spectra in toluene-d_8 of (bottom) DDA; (top) [$ZnCy_2$]; (middle) [$ZnCy_2$]/DDA (1:2) mixture, 10 minutes after mixing. See Table IV.1 for attributions of some peaks.

Clearly, the DDA and [ZnCy$_2$] resonances are shifted for the [ZnCy$_2$]/DDA (1:2) mixture. The α-CH$_2$ and the NH$_2$ protons of the [ZnCy$_2$]/DDA (1:2) mixture appear respectively at δ = 2.39 and 0.76 ppm, instead of δ = 2.55 and 0.55 ppm for the free amine. Moreover, the self-diffusion coefficients (noted D), measured by PGSE-NMR spectroscopy, for DDA (D= 12.0×10^{-10} m^2.s^{-1}) and [ZnCy$_2$] alone (D=8.3×10^{-10} m^2.s^{-1}) are significantly higher than those measured for the [ZnCy$_2$]/DDA (1:2) mixture (D=9.6×10^{-10} and 7.3×10^{-10} m^2.s^{-1}, respectively) under similar experimental conditions. Such observations indicate a fast exchange (on the NMR timescale) between free and coordinated amine molecules and substantiate the reversible coordination of the amine to the metal centre of the zinc complex to afford an adduct as previously observed for [ZnCy$_2$]/DDA (1:2) mixture.[20] 30 minutes after mixing, the diffusion coefficients becomes even smaller (D = 8.2(±0.2) x 10^{-10} m^2.s^{-1} and 6.8(±0.1) x 10^{-10} m^2.s^{-1}, for DDA and [ZnCy$_2$] respectively). Surprisingly, an additional sharp signal at 1.44 ppm corresponding to cyclohexane molecules is observed. This signal continuously increases over time. In addition, several new signals at 3.08, 2.97, 2.23, and 0.35 ppm appear. Their intensities increase slowly over time (up to 96 h) while the ones associated to both DDA and [ZnCy$_2$] compounds decrease (Figure IV.5). The complete disappearance of the [ZnCy$_2$] resonances is reached after ca 26 h while the new resonances exhibit a maximum of intensities after ca 8 h, then slowly disappear and can no longer be observed after 96 h. 2D ^{1}H and ^{13}C NMR experiments (COSY, HSQC, HMBC) clearly evidence that these new signals correspond to Zn amido complexes (Table IV.1).

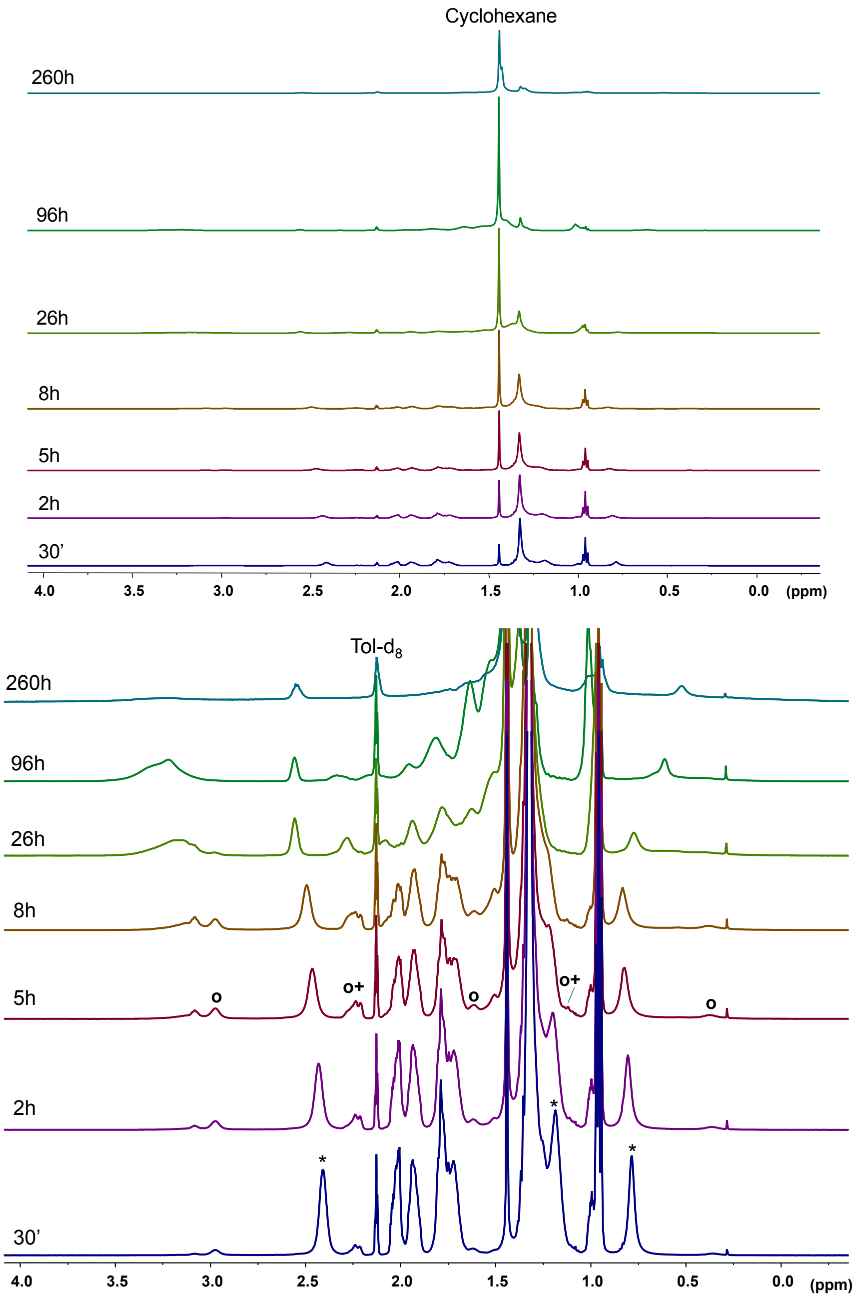

Figure IV.5 (Top) ^{1}H NMR spectra in toluene-d$_8$ of a solution of [ZnCy$_2$]/DDA (1:2) for different waiting time. (Bottom) Zoom of the top ^{1}H NMR spectra to better observe the small resonances. *, ■, o, ◊, and ▼ indicate the characteristic resonances of respectively, the DDA, the [ZnCy$_2$], the monomeric, the dimeric, and the oligomeric Zn amido molecules, respectively.

	NH	α-CH_2	β-CH_2	central-CH_2	CH_3
DDA[a]	0.55	2.55/ 42.4	1.30/ 34.3	1.25-1.39/ 22.7-32.0	0.96/ 14.1
[$ZnCy_2$]-DDA	0.76	2.39/ 41.9	1.19/ 33.3	1.17-1.39/ 22.7-32.0	0.96/ 14.1
Monomeric Zn amido	0.35	2.97/ 48.7	1.62/ 38.5	1.25-1.43/ 22.7-32.0	0.96/ 14.1
Dimeric Zn amido	0.54	3.08/ 48.9	1.69/ 38.5	1.25-1.51/ 22.7-32.0	0.96/ 14.1
Oligomeric Zn amido	0.35-0.72	3.14-3.33/ 48.6-49.0	1.74-1.82/ 38.6-38.7	1.35-1.64/ 22.8-33.1	0.98-1.01/ 14.1
	Zn-CH	**α-CH_2**	**β-CH_2**	**γ-CH_2**	
[$ZnCy_2$][b]	1.09/ 33.9	1.40-1.73/ 31.7	1.69-1.80/ 30.9	1.67-1.51/ 27.9	
[$ZnCy_2$]-DDA	1.00/ 30.6	1.93-2.01/ 33.9	1.69-1.77/ 31.1	1.73-1.77/ 28.5	
Monomeric Zn amido	1.13/ 27.4	2.00-2.22/ 34.3	1.74-1.92 31.1	1.80-1.93/ 28.7	
Dimeric Zn amido	1.13/ 27.4	2.03-2.22/ 35.3	1.76-1.92 31.2	1.80-1.93/ 28.8	

Table IV.1 ^1H and ^{13}C chemical shifts (δ_H/δ_C; ppm) for the various species observed in the [$ZnCy_2$]/DDA (1:2) mixture in toluene over time.

These latter are produced by the acid-base reaction between [$ZnCy_2$] and DDA that forms [$CyZn-N(H)C_{12}H_{25}$] compounds and cyclohexane, concomitantly. Interestingly, DOSY measurements give two diffusion coefficients (Figure IV.6): $D_1 = 6.6(\pm0.1) \times 10^{-10}$ $m^2.s^{-1}$ and $D_2 = 4.3(\pm0.1) \times 10^{-10}$ $m^2.s^{-1}$ that correspond to both monomeric and dimeric Zn amido complexes, respectively.[21, 22]

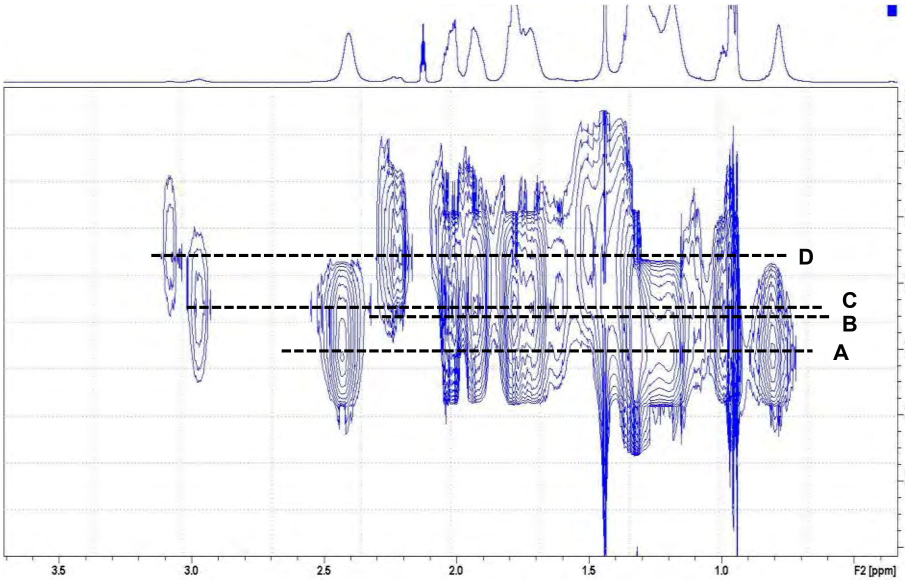

Figure IV.6 DOSY spectrum of a toluene-d_8 solution of [ZnCy$_2$]/DDA (1:2), 2 hours after mixing. A, B, C and D correspond to diffusion coefficient of DDA, [ZnCy$_2$], monomeric and dimeric Zn amido complexes, respectively.

These Zn amido complexes are in slow exchange (in the ms range) with free DDA and [ZnCy$_2$] molecules as evidenced by NOESY (Figure IV.7).

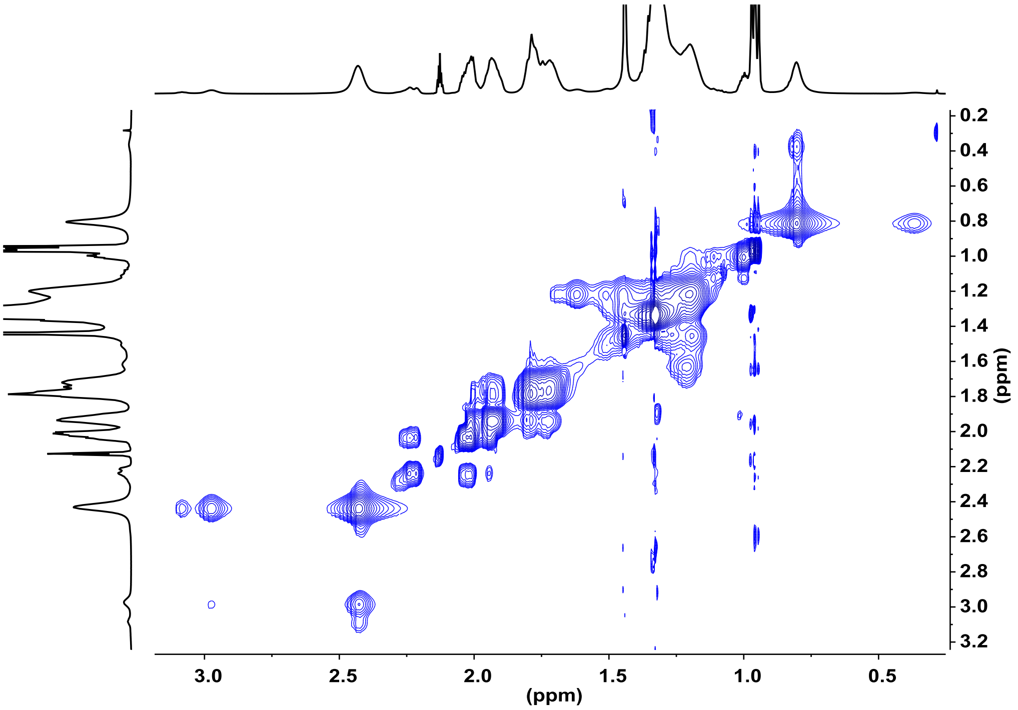

Figure IV.7 ^{1}H NOESY NMR spectrum of a toluene-d_8 solution of [ZnCy$_2$]/DDA (1:2), 2 hours after mixing.

Strong negative cross-peaks between the DDA and the Zn amido resonances on the one hand and between the [ZnCy2] and the Cy group of the Zn amido complexes resonances on the other hand are indeed observed. After 26 h, new broad resonances appear, notably above 3 ppm and below 0.9 ppm. Their diffusion coefficients become lower and lower over time. The D values range from 2.7 to 4.0(±0.3) x 10^{-10} $m^2.s^{-1}$ for 26 h of waiting time and decrease to 1.3 to 2.0(±0.2) x 10^{-10} $m^2.s^{-1}$ for 96 h. These results evidence that bigger and bigger oligomeric Zn amido complexes are formed over time (from 2-3 nm at 26h to 4-6 nm at 96 h using the Stokes-Einstein equation, corrected by the change of viscosity of the mixture). Their ^1H resonances can be edited with a diffusion filter experiment (Figure IV.8). The diffusion filtered ^1H NMR spectrum confirms that the Zn oligomers are mostly composed of Zn amido molecules with only few residual cyclohexyl groups.

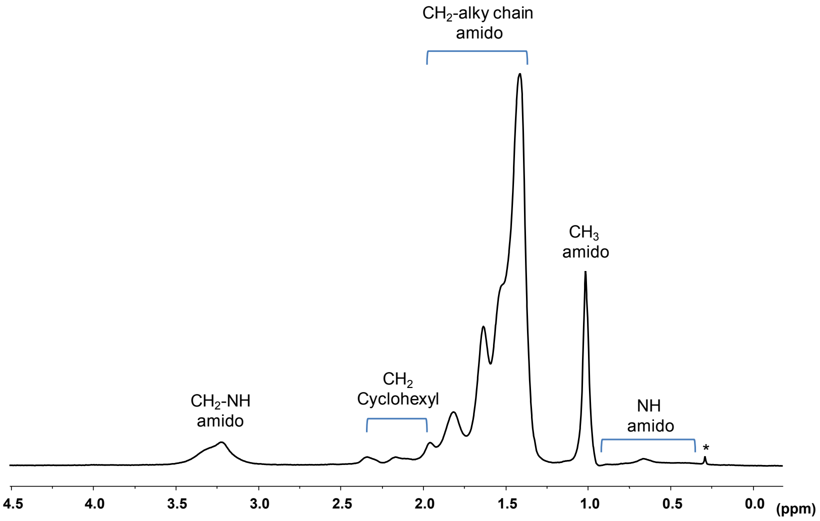

Figure IV.8 Diffusion filtered ^1H NMR spectrum in toluene-d8 of a solution of [ZnCy2]/DDA (1:2), 96 h after mixing. The diffusion filter was set in order to remove the fast diffusing species. * Trace of grease.

96 h after mixing, a gel starts to build inside the toluene solution leading to very broad resonances for the Zn amido oligomers. The DDA resonances remain sharp evidencing that residual DDA molecules that are not involved in the gel exist in the toluene solution (Figure SI4, 260 h).

Therefore, these experiments in toluene demonstrate that a slow reaction occurs between [$ZnCy_2$] and DDA leading to oligomeric species and formation of cyclohexane. The "polymerization" of [$ZnCy_2$] with DDA explains the observed gelation of the mixture.

After getting such information in solution, similar experiments were performed on the [$ZnCy_2$]/DDA (1:2) mixture.

Solid state NMR spectroscopic study

Magic Angle Spinning (MAS) NMR experiments were conducted on a [$ZnCy_2$]/DDA (1:2) mixture. Mixing the two powders of [$ZnCy_2$] and DDA leads to a liquid at room temperature.[23] ^{13}C spectra were acquired with Cross-Polarization (CP), Direct-Polarization (DP), and Insensitive Nuclei Enhanced by Polarization Transfer (INEPT). DP sequence yields quantitative spectra of all the ^{13}C nuclei present in the sample, while CP and INEPT sequences edit molecular segments being respectively rigid (with order parameter $S > 0.5$ and/or correlation time of molecular segment reorientation $\tau c > 10 \mu s$) or mobile ($S < 0.05$ and $\tau c < 0.01 \mu s$).[24] 30 minutes after mixing, no signal is detected in the ^{13}C CP-MAS experiment (Figure IV.9) while strong ^{13}C signal are observed in the ^{13}C INEPT-MAS experiment (Figure IV.10). These results indicate that at the beginning of the reaction, the [$ZnCy_2$]/DDA (1:2) mixture is a liquid phase with highly mobile molecules.

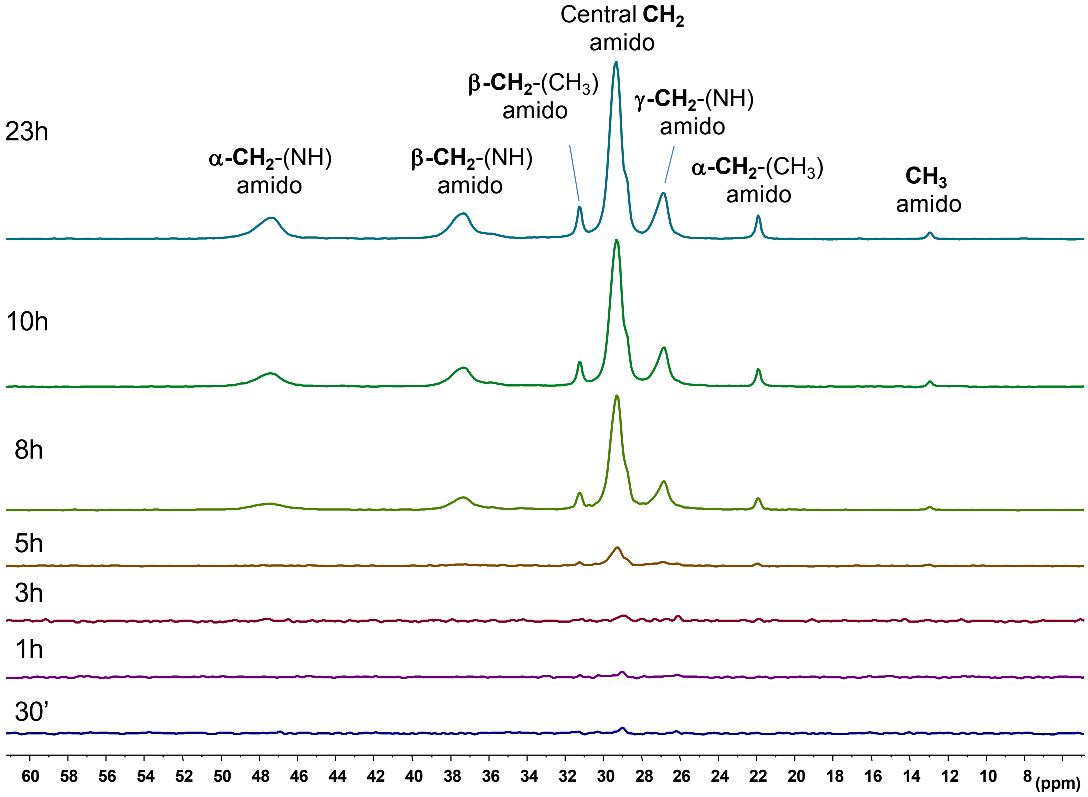

Figure IV.9 ^{13}C CP-MAS experiment of the [ZnCy$_2$]/DDA (1:2) mixture over time.

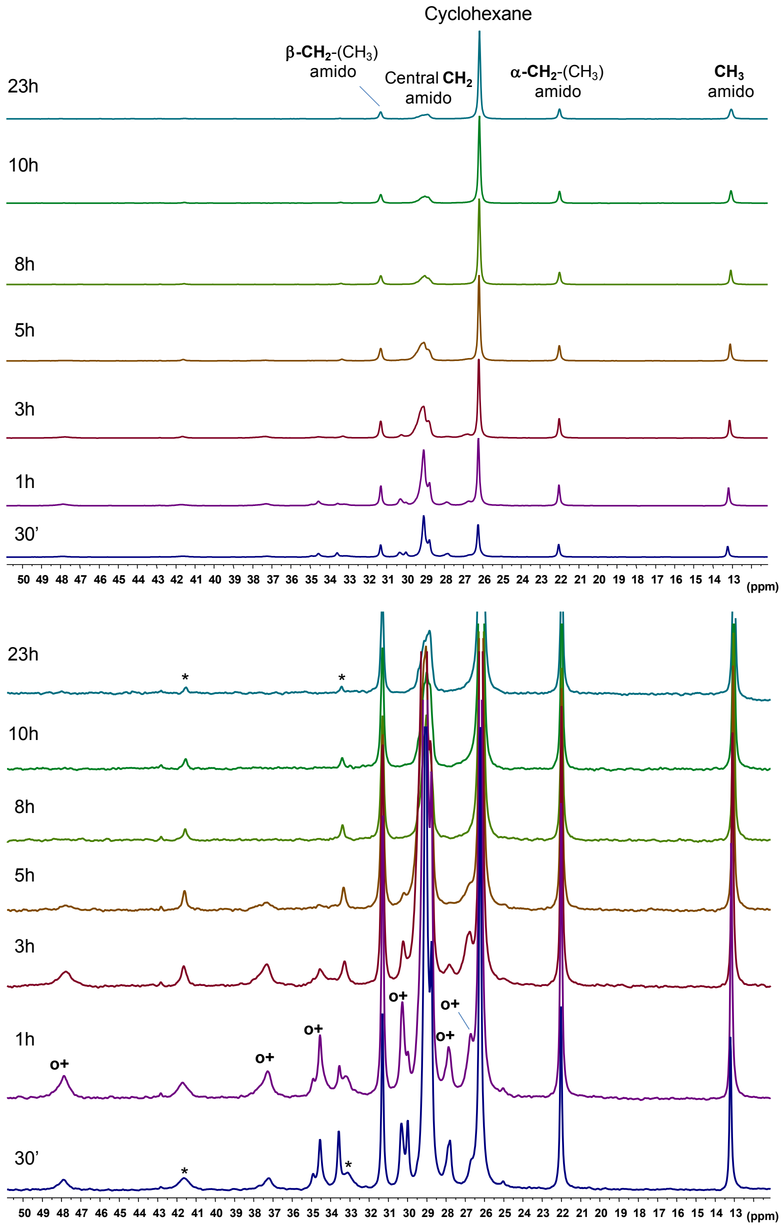

Figure IV.10 (Top) ^{13}C INEPT-MAS experiment of the [ZnCy$_2$]/DDA (1:2) mixture over time. (Bottom) Zoom of the top ^{13}C INEPT-MAS spectra to better observe the small resonances. *, ■, o and ◊ indicate the characteristic resonances of, respectively, DDA, [ZnCy$_2$], the monomeric and the dimeric Zn amido molecules, respectively.

Four sets of signals corresponding to DDA, [ZnCy$_2$], cyclohexane, and Zn amido complexes (both monomeric and dimeric species) are observed in the ^{13}C INEPT-MAS spectra. The intensities of the ^{13}C resonances of the Zn amido complexes observed in the ^{13}C INEPT-MAS spectra increase over time until the signals associated to [ZnCy$_2$] species disappear (maximum concentration at ca 2 h). Then, the Zn amido resonances slowly disappear and no more signal is detectable after 8 h. Concomitantly the intensity of the ^{13}C resonance of the cyclohexane ($\delta = 26.2$ ppm) observed in the ^{13}C INEPT-MAS spectra increases over time. On the other hand, ^{13}C signals characteristic of the Zn amido complexes start to appear in the CP-MAS spectra after 5 h. Their intensities increase continuously over time up to ca 23 h (Figure IV.9). These results indicate that Zn amido complexes become more and more rigid over time and substantiate the oligomerization reaction. The final ^{13}C CP-MAS spectrum is composed only of amido resonances and no more cyclohexyl resonance is detected, as in toluene solution. In the final ^{13}C CP-MAS spectrum, the most intense resonances correspond to the carbons close to the NH group while the carbon resonances of the CH_3 group are much weaker (Figure IV.9). The reverse is observed in the ^{13}C INEPT-MAS (Figure IV.10), stating the presence of a rigid Zn-NH core and a much more mobile methyl alkyl chain extremity. Note that a small amount of residual mobile DDA can be detected in the ^{13}C INEPT-MAS at the end of the oligomerization.

The kinetics of the oligomerization have been determined following the cyclohexane resonance over time (Figure IV.11). Fitting of the area of the cyclohexane resonance as a function of time by an exponential decay gives a characteristic constant of $k \sim 1\ h^{-1}$ for DDA. This constant is strongly dependent on the exact nature of the amine used.

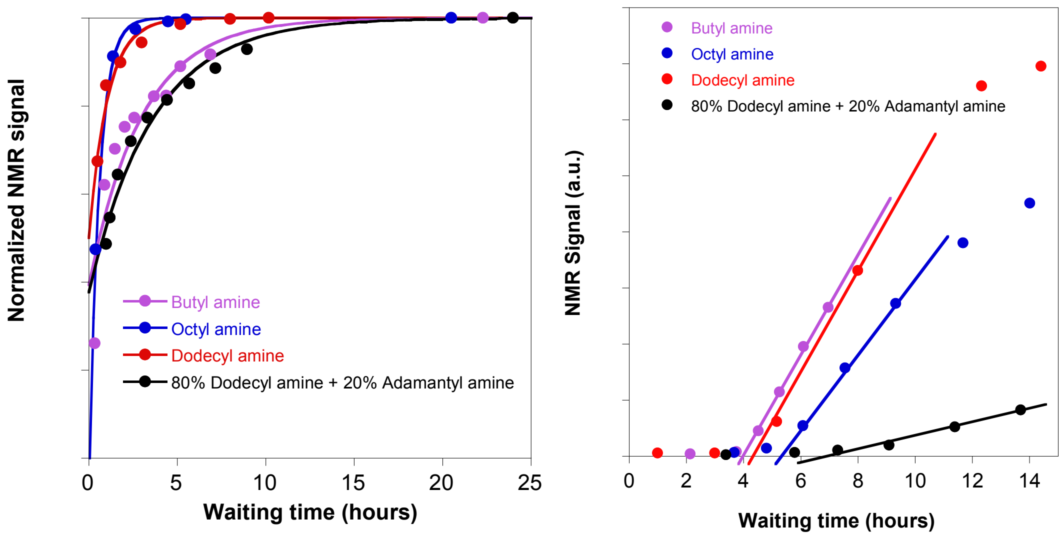

Figure IV.11 (Left) Normalized area of the cyclohexane ^{13}C resonance (in the DP-MAS experiment) as a function of waiting time for the [$ZnCy_2$]/amine (1:2) mixture, for four types of amine. The data are roughly fitted with the following equation: $y = \ln(\frac{I_f - I(t)}{I_f})$ $I_{normalized} = 1 - \exp(-(t+t_a)/t_c)$ where t_a and t_c are respectively an adjusting time and a characteristic time of cyclohexane formation. The adjusting time (which was found positive and can be related to some fast initiation process - the kinetic is not a simple exponential decay-) as well as the characteristic time (see Table 1 in the main text) increased with the amine order Octyl amine ($t_a \sim 0$ h) < Dodecyl amine ($t_a \sim 0.7$ h) < Butyl amine ($t_a \sim 1.5$ h) < Mixture 80% of dodecyl amine + 20% adamantyl amine ($t_a \sim 1.8$ h). (Right) Integrated area of the whole ^{13}C spectrum (in the CP-MAS experiment, see Figure SI8) as a function of waiting time for the [$ZnCy_2$]/amine (1:2) mixture, for four types of amine. For each sample, a line is drawn to estimate the onset time of gelification (see Table IV.2).

	OA	DDA	BUA	80% DDA + 20% ADA[c]
t_{rcyclo}[a] (min)	34 ± 12	62 ± 20	180 ± 60	215 ± 60
$t_{onsetgel}$[b] (min)	320 ± 40	270 ± 30	240 ± 20	420 ± 40

Table IV.2. Influence of the amine structure on the kinetics of oligomerization and gel formation at room temperature. [a] t_{rcyclo} corresponds to the characteristic time of the cyclohexane release, t_{rcyclo} is determined by ^{13}C DP-MAS NMR. The concentration of cyclohexane versus time in the mixture is adjusted to an exponential function with the characteristic time (Figure IV.11). [b] $t_{onsetgel}$ corresponds to the onset time of gelification, $t_{onsetgel}$ is determined by ^{13}C CP-MAS NMR. The integrated area of the whole ^{13}C spectrum is used to estimate the onset time (Figure IV.11). [c] OA, DDA, BUA, and ADA stands for Octyl amine, Dodecyl amine, Butyl amine, and Adamantyl amine, respectively

Finally, for comparison, the [ZnCy$_2$]/DDA (1:2) gel formed in the toluene solution has been transferred in a MAS rotor and the ^{13}C CP-MAS and INEPT-MAS experiment performed. Identical ^{13}C spectra were obtained (Figure IV.12). The reaction in toluene or in the solid state is the same and corresponds to the formation of Zn amido complexes and their oligomerization. This reaction is however one order of magnitude slower in toluene (k ~ 0.07 h^{-1}).

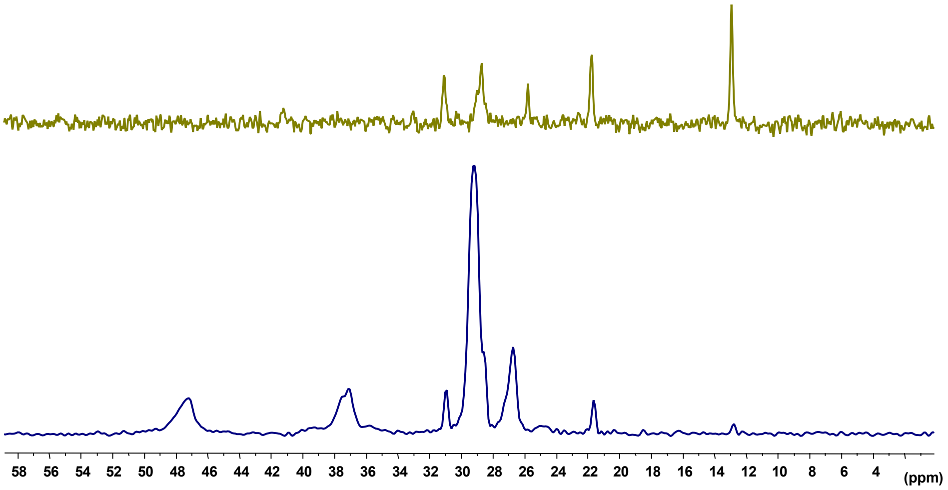

Figure IV.12 (Top) ^{13}C INEPT-MAS and (Bottom) ^{13}C CP-MAS spectrum of the gel formed in the [ZnCy$_2$]/DDA (1:2) mixture in toluene.

IV. 3. 2 Molecular simulations

In order to support these results molecular simulations were performed for such an oligomeric $[Zn(NHR)_2]_n$ structure showing that the total Gibbs free energy is equal to -34.2 kcal.mol^{-1} per added zinc, *i.e.* the reaction is exothermic. The formation of oligomers is therefore energetically favorable.

Calibration of the calculation level

Various calculation levels were investigated for their ability to describe the coordination sphere of zinc, especially the Zn-C and Zn-N bond lengths, in dialkylzinc and zinc-amido complexes. Three representative experimental structures were selected from the Cambridge Data Base (CDB) (see structures below). The performance of the hybrid functional B3PW91 was compared to the one of PBE-D3 and M06L functionals. In contrast to the former, the two latter functionals have been designed to be able to account for weak non-bonding interactions.[25] The functionals have been used in combination with various basis sets implemented in Gaussian09 (6-31G**, DGDZVP, and def2-TZVP).

The calculated Zn-C bond length of C_i-symmetric $[ZnEt_2]$ is very sensitive to the basis set. Whatever the calculation level, it is longer than the experimental value (1.9547 Å).[26] The shortest calculated values are obtained at the B3PW91/DGDZVP and M06L/DGDZVP levels, *i.e.* 1.9640 Å and 1.9645 Å, respectively.

The description of the Zn-N bond was investigated in the zinc-amido complexes referred to as DOMWEH[27] and CADCEP[28] in the CDB (see structures below).

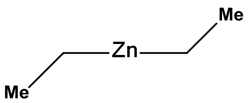

$ZnEt_2$

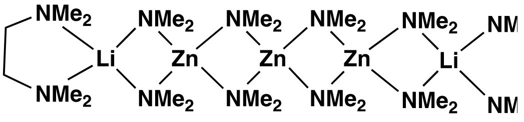

DOMVEH

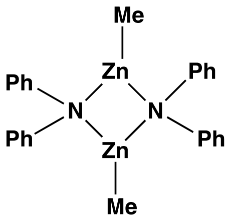

CADCEP

In the case of the binuclear Zn-amido complex CADCEP, the best compromise for an accurate description of both the Zn-CH_3 and Zn-NPh_2 bonds is the B3PW91/DGDZVP level of calculation. The PBE-D3 and M06L functionals yield too long and non-equivalent Zn-amino bonds (Table IV.3). The calculation of Zn-C and Zn-N bond lengths is little sensitive to the basis set.

	Zn-Me	Zn-NPh_2	Zn-NPh_2	Zn-Zn	Zn-N-Zn	N-Zn-N
CDB	1.955	2.079	2.081	2.913	90.6	89.3
		2.062	2.066		90.7	89.4
B3PW91/DGDZVP	1.955	2.096	2.103	2.961	90.1	90.1
		2.084	2.088		89.8	90.0
B3PW91/	1.957	2.096	2.101	2.936	90.8	89.0
def2-SVP/def2-TZVP(Zn)	1.960	2.089	2.086		91.0	89.0
B3PW91/def2-TZVP	1.961	2.101	2.094	2.932	88.9	91.2
	1.964	2.085	2.089		89.0	90.9
M06L/def2-TZVP	1.956	2.036	2.035	2.982	89.3	90.5
	1.952	2.172	2.204		90.2	89.6
PBE-D3/def2-TZVP	1.960	2.082	2.086	2.966	89.8	89.9
	1.963	2.122	2.113		89.9	90.4
PBE-D3/DGDZVP	1.960	2.083	2.087	2.999	91.1	88.8
	1.963	2.127	2.114		90.1	89.2

Table IV.3 Selected bond distances (in Å) and angles (in degrees) calculated at various level for CADCEP.

The discrimination between the various calculation levels is more difficult in the case of trinuclear Zn-amido complex DOMWEH: M06L/Def2TZVP ≈ PBE-D3/Def2TZVP > PBE-D3/DGDZVP ≈ B3PW91/DGDZVP. Whatever the calculation level, both the calculated Zn-N bond lengths and the Zn-Zn bond distances are longer than the experimental values (Table IV.4).

	Ring			End----Li
	Zn-N	Zn-N	Zn-Zn	Zn-N
CDB	1.998	2.029	2.851	2.014
	1.975	2.016		2.005
B3PW91/DGDZVP	2.086	2.061	2.928	2.081
	2.110	2.070		2.086
B3PW91/ def2-SVP/def2-TZVP(Zn)	2.094	2.068	2.910	2.059
	2.106	2.062		2.067
M06L/ def2-TZVP	2.081	2.061	2.839	2.042
	2.096	2.053		2.053
PBE-D3/def2-TZVP	2.086	2.052	2.873	2.038
	2.104	2.062		2.052
PBE-D3/DGDZVP	2.087	2.055	2.889	2.068
	2.110	2.065		2.069

Table IV.4 Selected bond distances (in Å) and angles (in degrees) calculated at various level for DOMWEH.

B3PW91/DGDZVP and PBE-D3/DGDZVP were therefore pre-selected. Since the last one takes into account van der Waals interactions, PBE-D3/DGDZVP was finally chosen for the theoretical studies described hereafter.

Formation of the organometallic gel

Formation of the organometallic gel is supposed to occur because of the three following reactions:

1) The formation of the 1:1 adduct between the zinc precursor and the amine

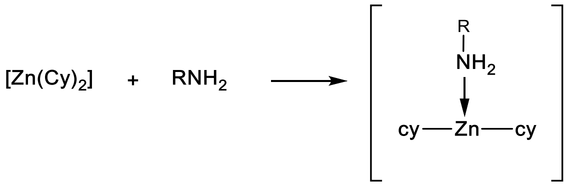

2) The conversion of the adduct through an intramolecular acido-basic reaction with release of cyclohexane

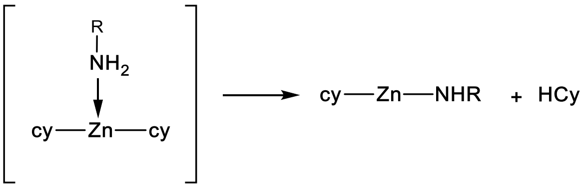

3) The polycondensation of the previous molecule with amine, leading to

oligomers of the zinc precursors.

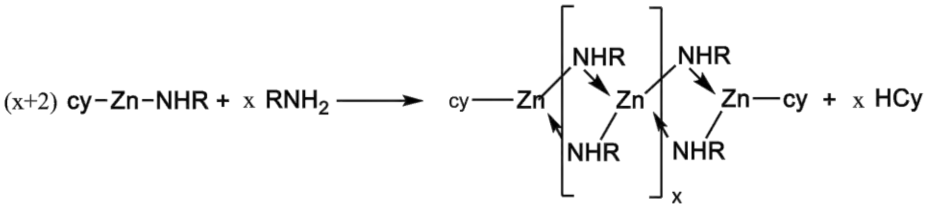

To better understand the structure of these oligomers, minimization of a tetranuclear bis-cyclohexyl-zinc amido complex has been performed. Figure IV.13 shows the corresponding conformation.

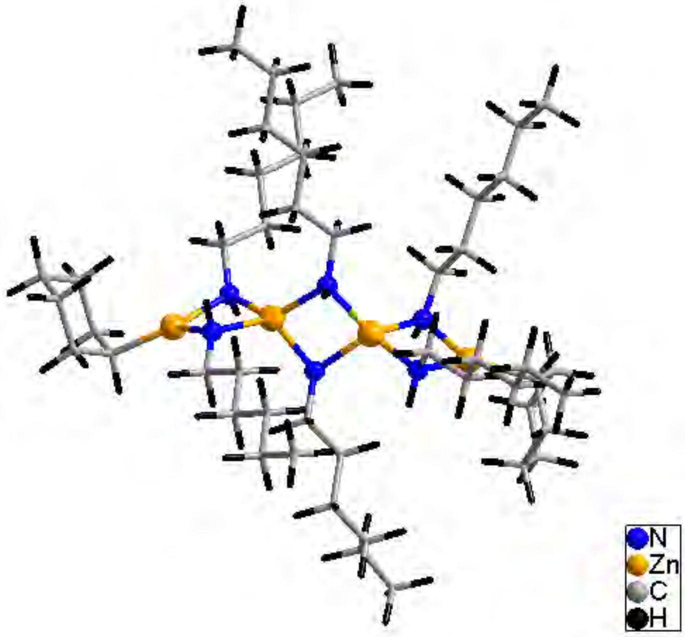

Figure IV.13: Minimize molecular structure of a tetranuclear *bis*-cyclohexyl-zinc amido complex.

Such calculation allows one to also estimate the energies related to the previously described reactions. In particular, the oligomerization consists in two acido-basic reactions and one cyclisation through the formation of two dative bonds per each zinc linked to the polymer. The calculated total Gibbs free energy is equal to -34.2 kcal.mol^{-1} per added zinc, stating that the reaction is exothermic. The formation of oligomers is therefore energetically favorable.

IV. 3. 3 Wide angle X-ray scattering

From the hypothetical model shown in Figure IV.13, a theoretical WAXS reduced intensity can be computed using Debbye's formula. Comparison to the WAXS experimental one (Figure IV.14 left) evidences the good agreement. Similarly, the theoretical Radial Distribution Function (Figure IV.14 right) obtained *via* the Fourier Transform of the theoretical reduced intensity exhibits similar curve as the experimental one.

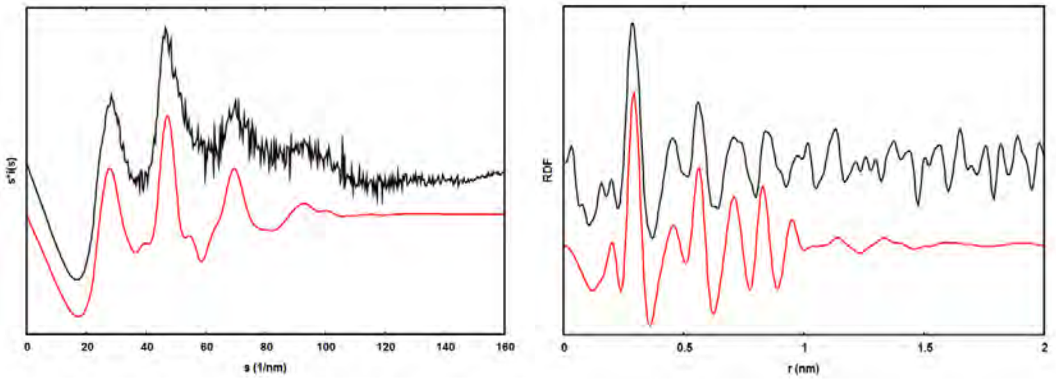

Figure IV.14 (Left) WAXS Reduced intensity, in black experimental and in red, computed from the molecular model given in Figure IV.13. (Right) Radial distribution function, in black experimental and in red, computed from the molecular model given in Figure IV.13.

The globally good agreement between theoretical and experimental data, observed both in reciprocal and real spaces is a clear evidence that the molecular structural features are realistic, especially the Zn-N framework. Indeed, calculated Zn-N and Zn-Zn distances of the optimized oligomer range from 2.054 Å to 2.081 Å (mean value = 2.064 Å) and from 2.843 Å to 2.895 Å (mean value = 2.862 Å), respectively. Those values are in very good agreement with the WAXS experimental values measured at 0.2 and 0.3 nm, respectively. Other studies have argued for such oligomeric structures but they have not been confirmed.[29, 30] The subsequent gelification and solidification processes should be the result of entanglement as well as cross-linkage between chains.

The reaction rate of this oligomerization depends on both the concentration of the reactants and on the amine structure (Table IV.2). Briefly, this rate is high for small alkyl amines and low for bulky amines. Consequently, the speed of the gel formation (which was found consistent between NMR and rheological studies) varies in function of the amine structure. One can therefore easily adjust the timescale of the gelification process of the organometallic precursor/amine mixtures either by a judicious choice of the amine or, for a constant composition, by changing the waiting time. Thus, a large range of viscosities of the mixtures can be attained, which is of paramount importance for sample processability.

IV. 4. Processability

Processability of the [ZnCy$_2$]/DDA gels was tested following three different paths (**Scheme IV.1**).

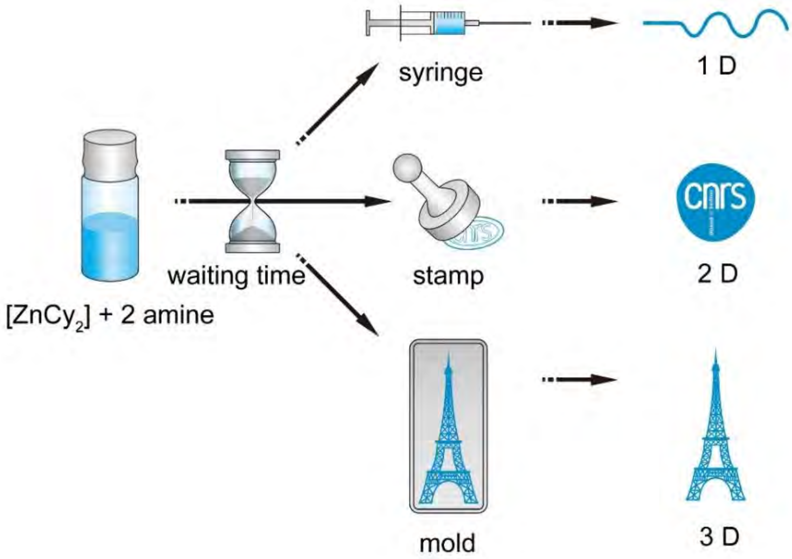

Scheme IV.1. Processing of the organometallic gel, leading to fibers (1D objects), patterns (2D objects) or molded materials (3D objects) before hydrolysis. The waiting time should be adjusted depending on the selected process.

The use of a simple extrusion process, a stamp, or a mould leads respectively to fibres with various diameters and lengths, thin patterns on a solid substrate, or more elaborate 3D forms of the organometallic gel. Upon exposure to air, all of these lead to the formation of hybrid zinc oxide structures. They exhibit the characteristic luminescence of ZnO nanoparticles (Figures IV.15 and IV.16)

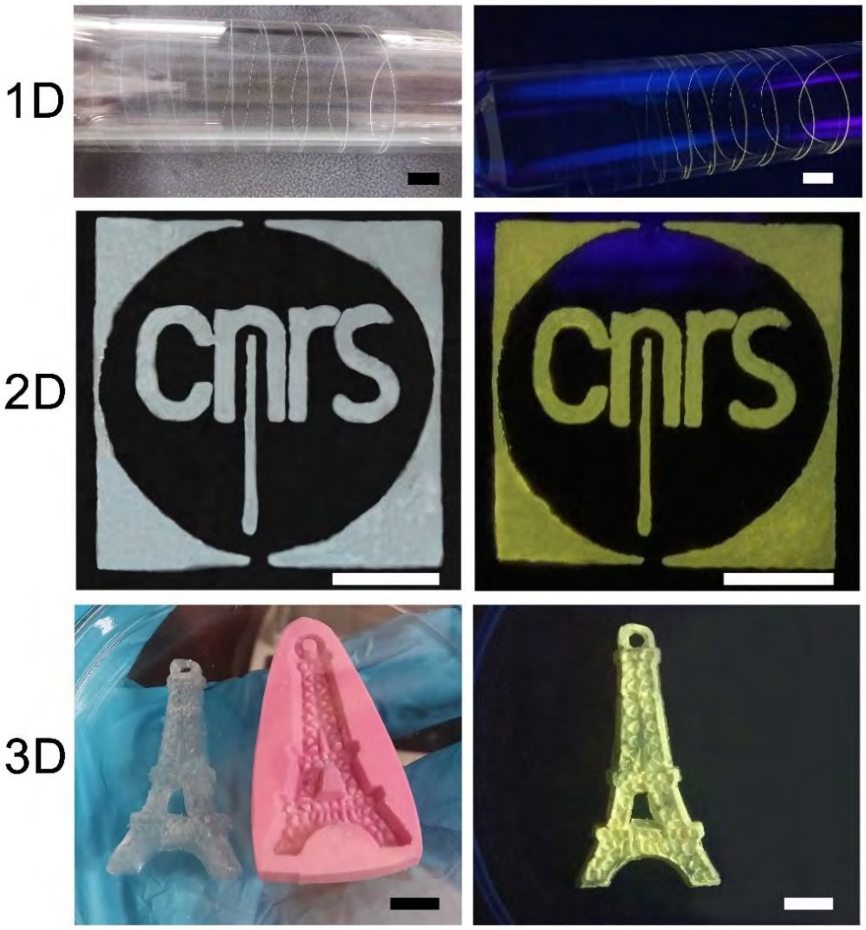

Figure IV.15 Left column. Fibres (1D object) coiled around a glass tube, patterns obtained by stamping on a glass slide (2D object), moulded Eiffel Tower (3D object) with its corresponding mould (pink silicone). Pictures of 1D and 2D objects are taken after exposure to air (in order to hydrolyse the organometallic gels), and before exposure to H_2O for the 3D object to show the transparent aspect of the organometallic gel under inert atmosphere. Right column. The same structures (after exposure to air) under UV light. The yellow luminescence (corresponding to a broad emission band around 580 nm, see Figure SI14) is due to the presence of ZnO in these final hybrid materials. Scale bar = 1 cm.

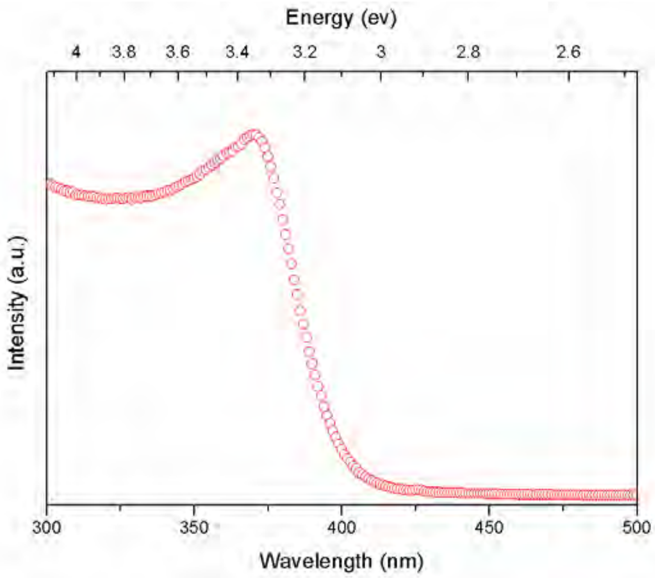

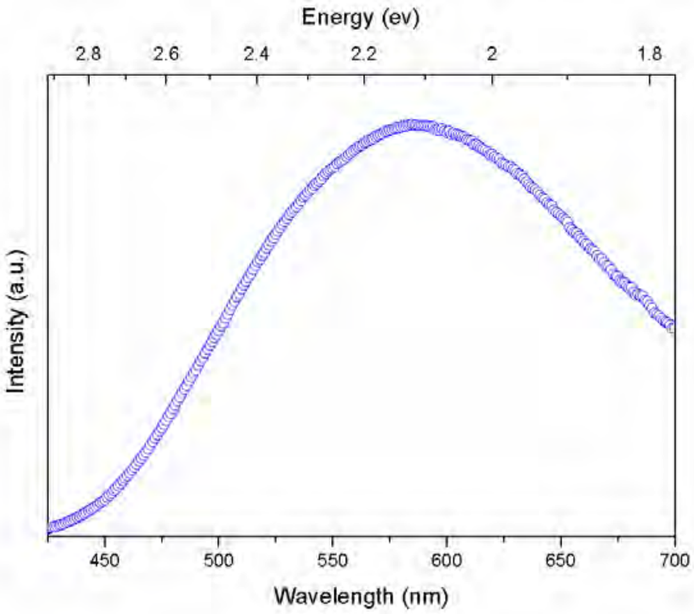

Figure IV.16 (Top) Excitation spectrum of the fibers after contact with air. Emission wavelength: 580 nm. (Bottom) Emission spectrum of the fibers after contact with air. Excitation wavelength: 340 nm.

Powder X-ray diffraction (PXRD) diagrams display the same pattern in the 15° to 40° range which corresponds to the hexagonal zincite phase, space group $P6_3mc$. No crystalline hydroxide phase is observed. Additional peaks at lower theta (5 to 13° range) are observed which corresponds to the amine species.[31] When the X-ray diffraction measurements are performed after calcination, all the peaks associated to the ligand disappear and only the diffraction diagram of the hexagonal zincite phase of ZnO remains. Decrease of the peak widths after calcination is clearly related to an increase in average size of the crystallites forming the material. Taking into account the anisotropy in shapes of ZnO nanoparticles, Scherrer analysis of the diffractogram suggests an average size of ca 6x30 nm^2 before calcination and 17x25 nm^2 after calcination (Figure IV.17).

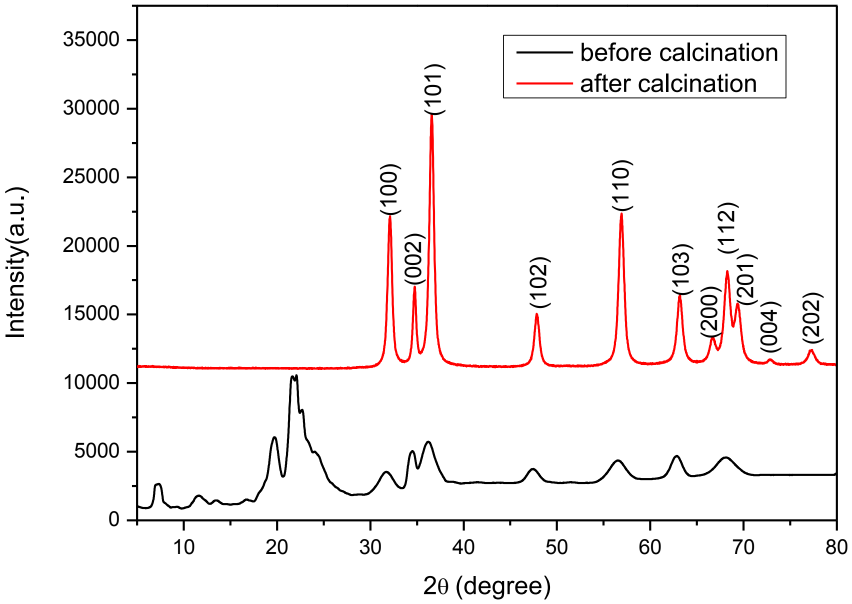

Figure IV.17 PXRD patterns before (a) and after (b) calcination of the ZnO hybrid material. The peak indications correspond to the hexagonal zincite phase, space group P63mc.

Compressive tests revealed that these materials are quite brittle with a Young's modulus of ca 71 ± 5 MPa and an ultimate tensile strength of 1.5 ± 0.3 MPa.

Evolution of the aspect of the gel

The aspect of the gel during the hydrolysis process was also qualitatively monitored by recording its aspect over time when exposed to the air. As shown in Figure IV.18, the aspect of the gel is strongly affected by the initial state of the zinc precursor / DDA mixtures, and therefore by the waiting time between mixing the two compounds and the exposure to air. Very surprisingly, the fastest changes are observed in the most viscous sample (with a waiting time of 10 h between mixing and hydrolysis): a thick crust is formed which then densifies at the air/mixture interface. For a sample corresponding to a short waiting time (30 minutes), the exposure of the gel to the air induces a continuous change in the whole solution which is more and more light-diffusive and white. Even if the complete understanding of the kinetic is beyond the scope of this manuscript, such simple experiments demonstrate the huge impact of the initial waiting time (and therefore of the gelation process) step. This step is critical in classical sol gel process to control size and shape of NPs. A similar effect is observed here. Hence, hydrolysis performed when the mixture is a viscous liquid (*i.e.* $t_w = 30$ min) leads to nanorods while hydrolysis in the gel phase ($t_w = 5$ and 10 h) yields to isotropic nanoparticles (Figure IV.18). The size analysis of these nanoparticles performed through a 2D-plot,[32] indicates that for short aging time, the anisotropic growth is the dominant process while for longer aging times, this latter is strongly limited or overridden by the nucleation processes. This is rationalized by the limited diffusion of the reactants and/or of the pristine ZnO nuclei with increasing viscosity.

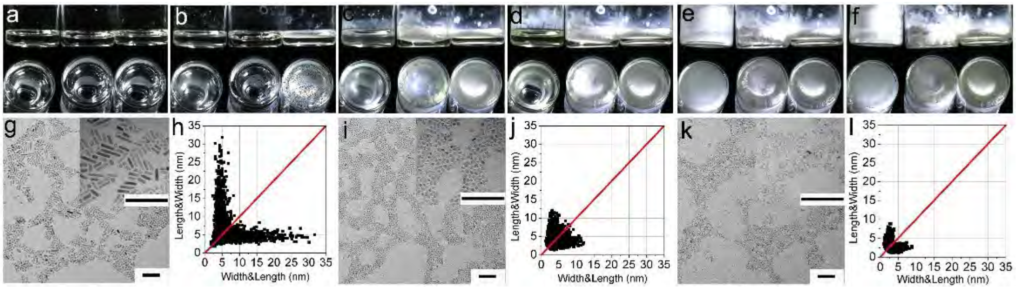

Figure IV.18 [$ZnCy_2$]/DDA (1:2) mixtures exposed to air. Top: Side view and bottom view of flasks (with lids off) containing the [$ZnCy_2$]/DDA (1:2) mixtures with various waiting times in the glove box (30 min, 5h, and 10 hours from left to right in each picture) and increasing time in contact with air (a), 5 minutes (b), 1 hour (c), 3 hours (d), 12 hours (e), and 3 days (f). Bottom: TEM images and the corresponding 2-D size plots of the samples after 3 days of hydrolysis. Samples with a waiting time in the glove box of: (g and h) 30 minutes, (i and j) 5 hours, (k and l) 10 hours. Scale bar corresponds to 60 nm.

Whatever the waiting time in the glove box (30 min, 5 or 10 hours) may be, point clouds (graphs h, j and l) present an apparent complex structure with different sub-populations of nanoparticles. The multivariate analysis of this data enables to isolate two sub-populations and to obtain more accurate quantitative values for each ones (proportion, average length and width, correlation, see Table IV.5). For short waiting time (30 minutes), the main population (representing 53% of the observed nanoparticles) corresponds to anisotropic nanoparticles (NPs) with an average width around 4.3 nm and a length of 11.1 nm. The calculated correlation between with and length is rather low and close to 0.2.

Waiting time	Length (nm)	Width (nm)	Population weight (%)	correlation
30 minutes	11.1 ± 9.8	4.3 ± 1.7	53	0.22
	5.8 ± 2.6	4.6 ± 2.1	47	0.85
5 hours	6.3 ± 3.2	3.3 ± 1.4	28	0.30
	4.7 ± 2.0	3.7 ± 1.7	72	0.86
10 hours	4.1 ± 2.1	2.2 ± 1.2	47	0.23
	2.7 ± 0.8	1.8 ± 0.6	53	0.14

Table IV.5 Multivariate analysis of the nanoparticle sizes.

This low value is related to the growth process with an increase of the length of the nanoparticles while the width is rather constant; it is consistent with previous studies[32]. The second one (representing 47% of the observed NPs) is associated to almost isotropic NPs with an average width around 4.6 nm and a length around 5.8 nm. The high correlation value calculated, *i.e.* 0.8, may correspond to a simultaneous growth on the two axes with two slightly different but correlated speeds. For longer waiting time (5h and 10h), the average dimension of both population is decreasing with time. At 5h, a small fraction of anisotropic NPs (28% of the NPs) was still observed but with lower aspect ratio than for 30 min (ca 2 vs 3). Most of the NPs are isotropic. At 10h, anisotropic NPs are still observed but with lower aspect ratio (below 1.8) than for other waiting times. In summary, it appears that, when performed in gel state, the hydrolysis process favor the formation of isotropic NPs.

Interestingly, the final hybrid material displays a liquid crystal state above ca 30 °C up to the melting point around 80 °C (Figure IV.19).

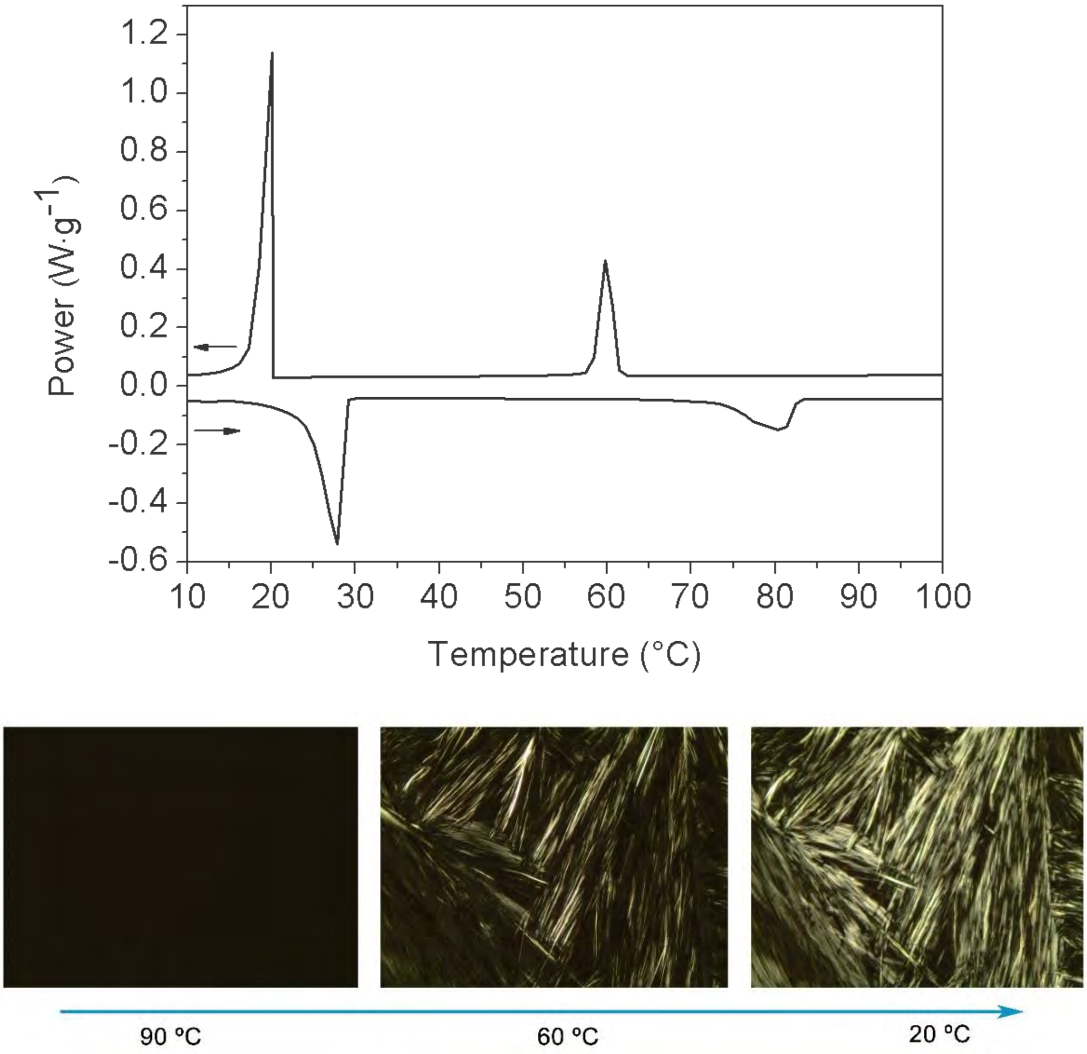

Figure IV.19 Top. Thermogram of the [ZnCy$_2$]/DDA (1:2) hybrid fiber after being exposed to the air for 3 days (cooling and heating rate 10 °C min^{-1}). Positive power corresponds to exothermic process. The thermograms are reproducible over heating/cooling cycles. Bottom. Polarized optical microscopy images at various temperature of ZnO/DDA (1:2) hybrid fibers after being exposed to the air for 3 days.

Therefore, melting these materials allows to easily reshape the hybrid materials as depicted in Figure IV.20.

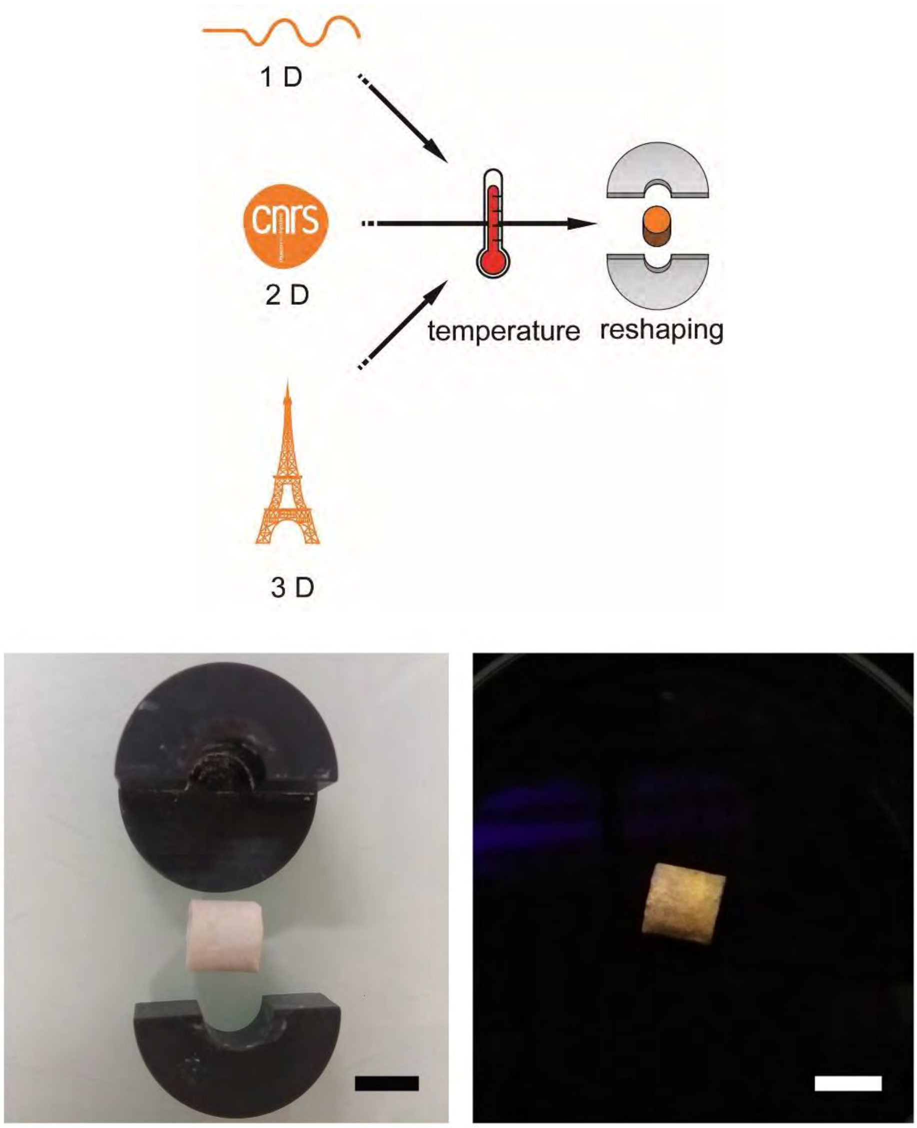

Figure IV.20 Reshaping of processed and hydrolyzed organometallic gel. Top: schematic principle. Bottom: example of the reshaping of the molded Eiffel Tower into a cylinder. Left: under visible light, reshaped material and the mold used. Right: reshaped material under UV light. Bar scale: 1 cm

Fibres of ZnO hybrid material calcined at 350 °C leads to pure ZnO fibres consisting of NPs (Figure IV.21). While the pristine fibre have a relatively smooth surface and a rather dense core, the sintered fibres have shrunk (in both radial and lateral axes by a factor 1/3) and present a tormented porous structure as shown by SEM analysis. As a proof of their dense and continuous structure, these ZnO fibres exhibit photocurrent properties under UV exposure.

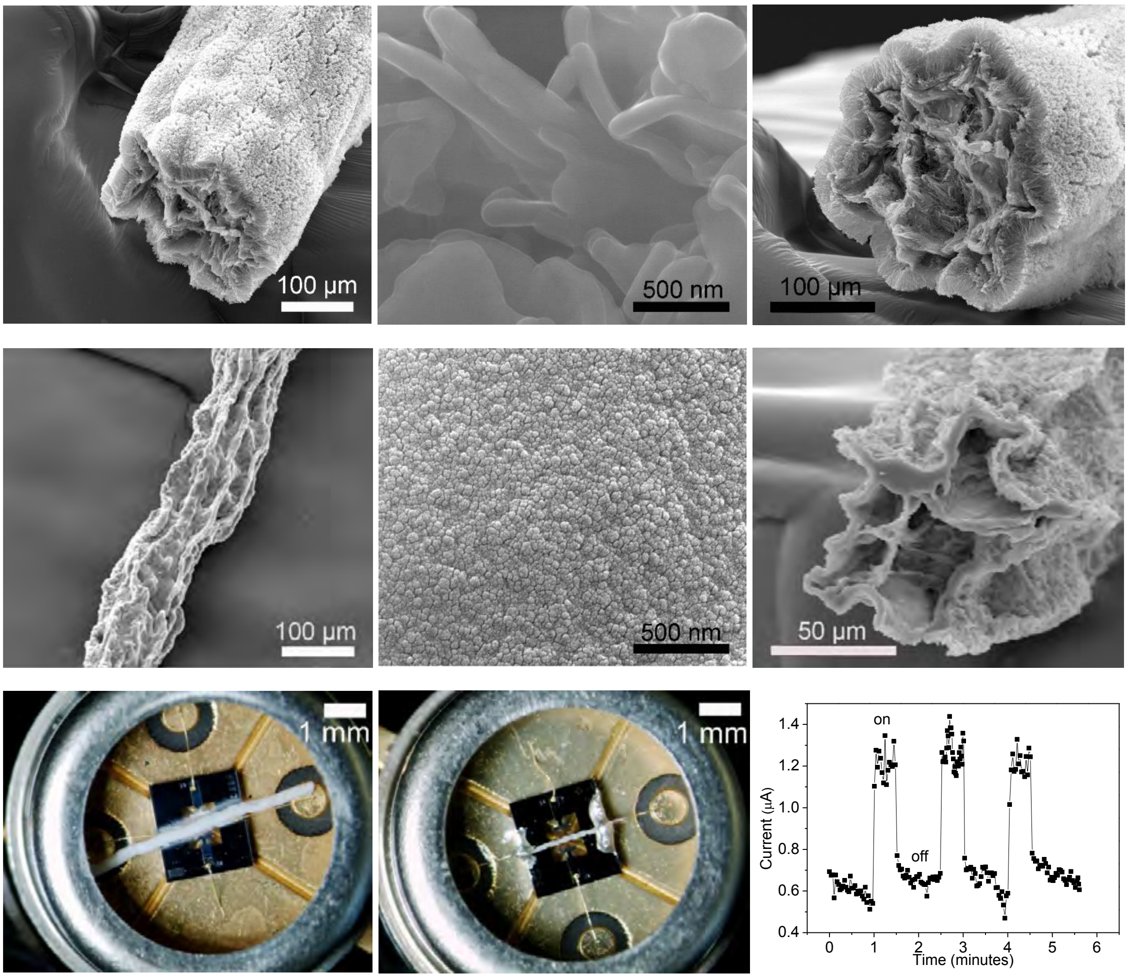

Figure IV.21 Top: SEM images at various magnifications of a ZnO hybrid fibre. From left to right: general view, surface of the fibre, cross section of the fibre. Middle: SEM images at various magnifications of the calcined ZnO hybrid fibre. From left to right: general view, surface of the fibre, cross section of the fibre.Bottom: pictures of the device used to measure the photocurrent properties: with the pristine ZnO hybrid fibre (left) and after its calcination (middle). Typical answer to UV exposure (wavelength: 365 nm) of the device (right).

IV. 5. Generalization

Fascinatingly, this new pathway towards inorganic material is not restricted to ZnO. Experiments performed with $[Sn(NMe_2)_2]_2$ and $[(Fe\{N(SiMe_3)_2\}_2)_2]$ organometallic precursors gave rise to similar results (Figures IV.22 and IV.23).

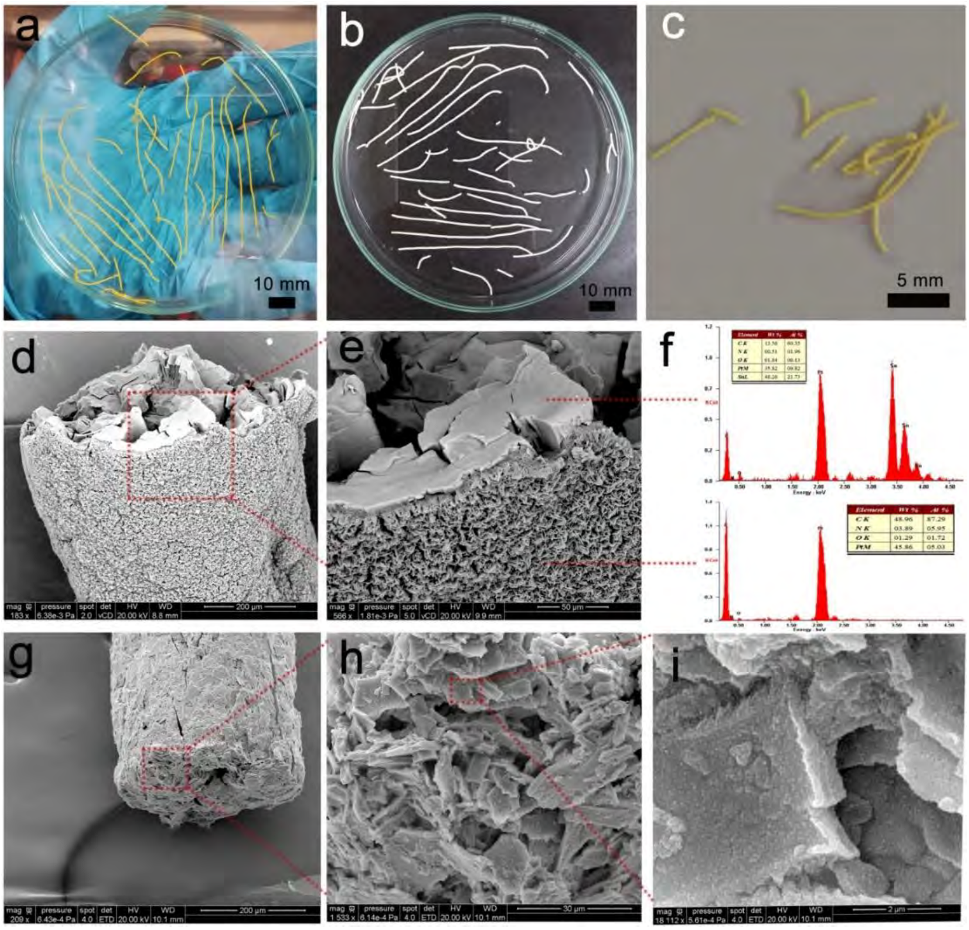

Figure IV.22 Fibers obtained from the $[Sn(NMe_2)_2]_2$/DDA (1:2) before and after hydrolysis. (a) Hybrid fibers of $[Sn(NMe_2)_2]_2$/DDA (1:2) in the glove box, (b) Same fibers after 3 days of hydrolysis, (c) and after calcination at 450 °C for 6 hours. (d and e) SEM images of the fibers after hydrolysis, but before calcination. The magnification of the surface of the fiber (e) suggests a “core-shell” structure. The EDX analysis (f) demonstrates that the inside of the fiber contains mainly tin and the shell mainly DDA. This “core-shell” structure could be induced by the shearing occurring during the fiber formation. (g-i) SEM image at various magnification of the fibers after calcination.

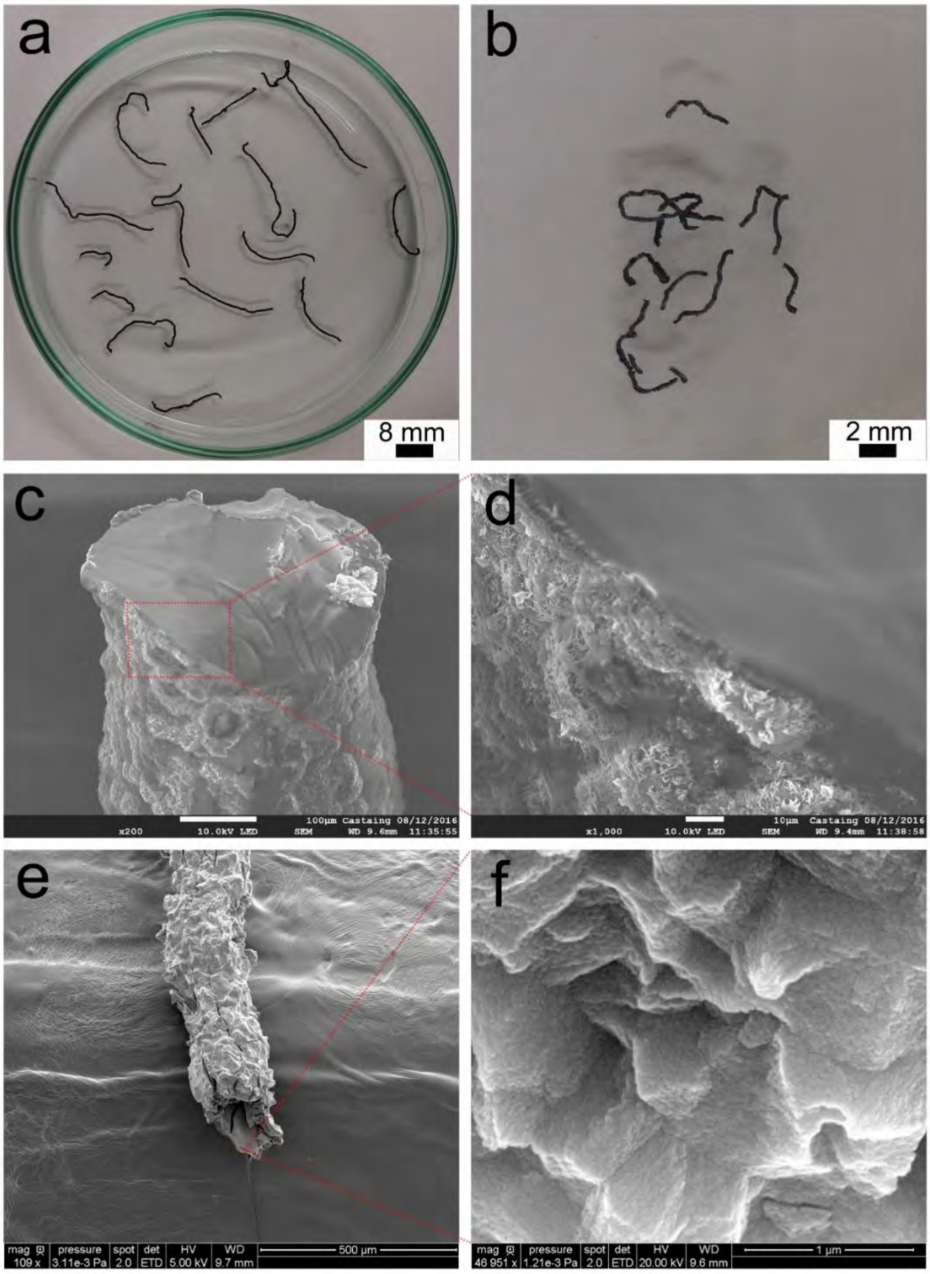

Figure IV.23 Morphology characterization of the iron oxide hybrid fibers before and after calcination: (a) photograph of the hybrid fibers after hydrolysis, (b) photograph of the fibers after calcination at 350 °C for 6 hours, (c and d) SEM images of the fibers after hydrolysis, but before calcination (e and f) SEM images of the fibers after calcination.

TEM pictures reveal that the fibers consist of very small nanoparticles before calcination (Figures IV.24 and IV.25).

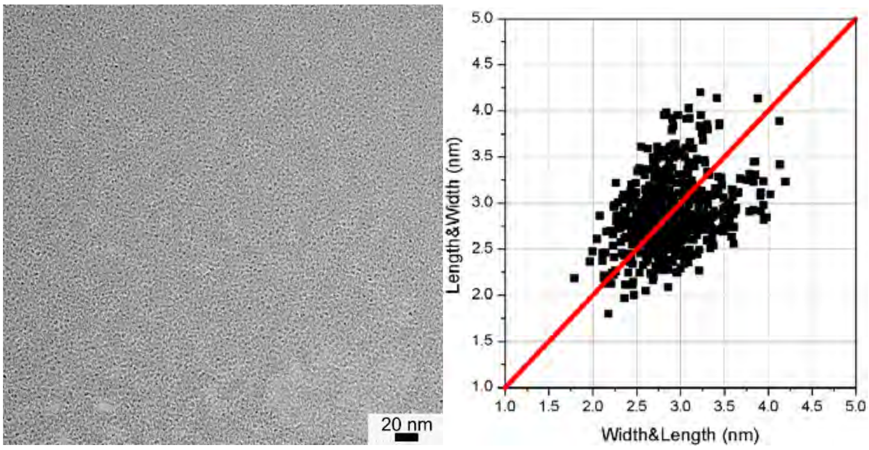

Figure IV.24 TEM image and the 2-D plot of the tin oxide hybrid materials (crushed fibers then dispersed in THF). The point cloud obtained is centered on the median (θ = 45°). This corresponds to the presence of quasi isotropic nanoparticles, the average size of which is ca 2.7 ± 0.8 and 2.3 ± 0.6 nm, , for the length and the width, respectively. The correlation between width and length is equal to 0.67 suggesting as observed previously for ZnO that a simultaneous growth on the two axis occurs with two slightly different but correlated speeds.

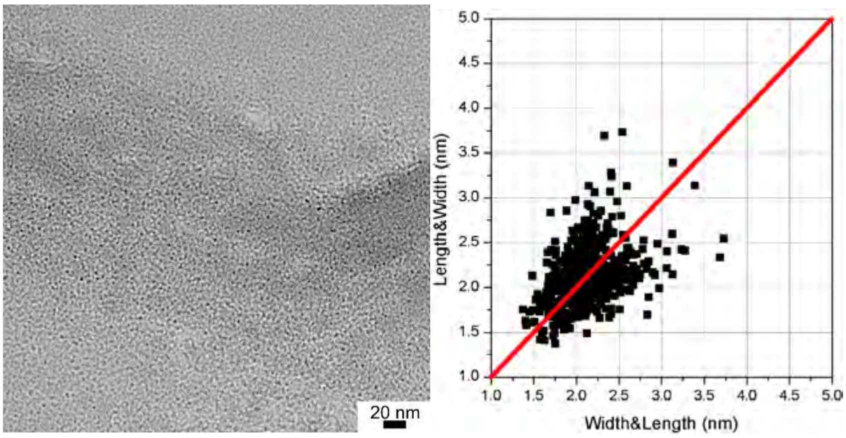

Figure IV.25 TEM image and the 2-D plot of the iron oxide hybrid materials (crushed fibers then dispersed in THF). The point cloud obtained is centered on the median (θ = 45°). This corresponds to the presence of quasi isotropic nanoparticles, the average size of which is ca 2.4 ± 0.8 and 2.0 ± 0.5 nm, for the length and the width, respectively. The correlation between width and length is equal to 0.63 suggesting as observed previously for ZnO and tin oxide that a simultaneous growth on the two axis occurs with two slightly different but correlated speeds.

After calcination, the PXRD patterns confirm the tetragonal phase of the material characteristic of SnO_2 (Figure IV.26) and the rhombohedral phase, characteristic of hematite, α-Fe_2O_3 (Figure IV.27).

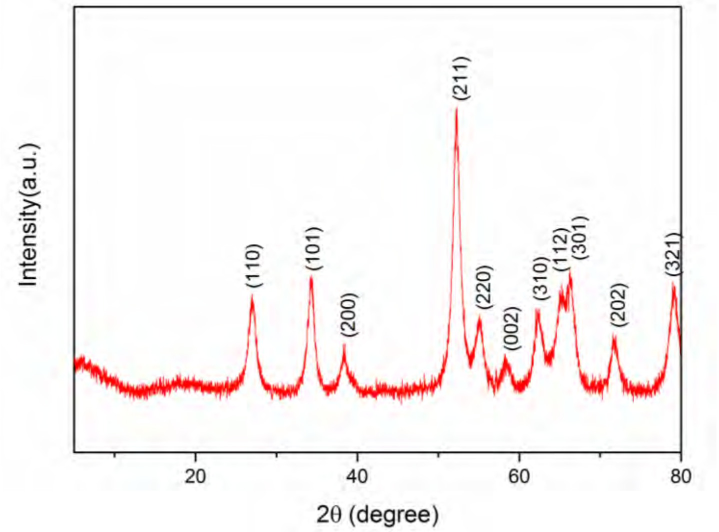

Figure IV.26 PXRD patterns of the tin oxide material obtained after calcination. Indexation is based on the tetragonal phase of the material characteristic of SnO_2 (JCPDS 01-071-5324). Scherrer analysis suggests an average size of ca 9 nm for the tin oxide crystallites after calcination.

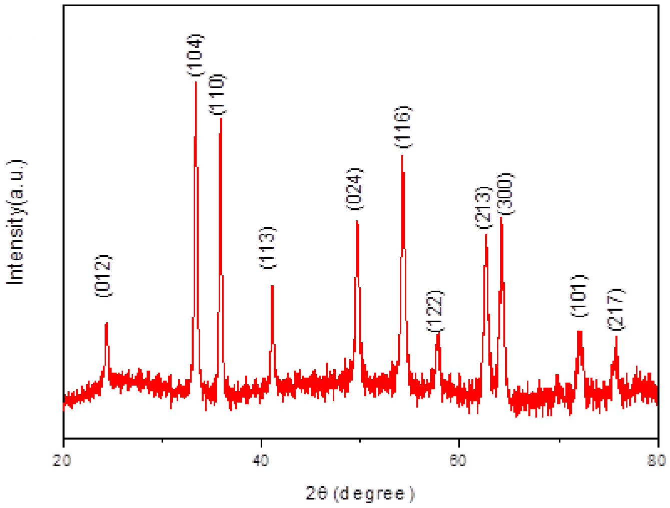

Figure IV.27 PXRD patterns of the iron oxide material obtained after calcination. Indexation is based on the rhombohedral phase characteristic of hematite, α-Fe_2O_3 (JCPDS 86-0550). Scherrer analysis suggests an average size of ca 40 nm for the iron oxide crystallites after calcination.

Both tin oxide and zinc oxide fibers behave as semiconductors (MOS) and as expected modification of their conducting properties in the presence of volatile chemical compound (VOC) is observed (Figure IV.28). This process appears to be extendable to a large number of organometallic precursors leading to processed material with many possible compositions and shape.

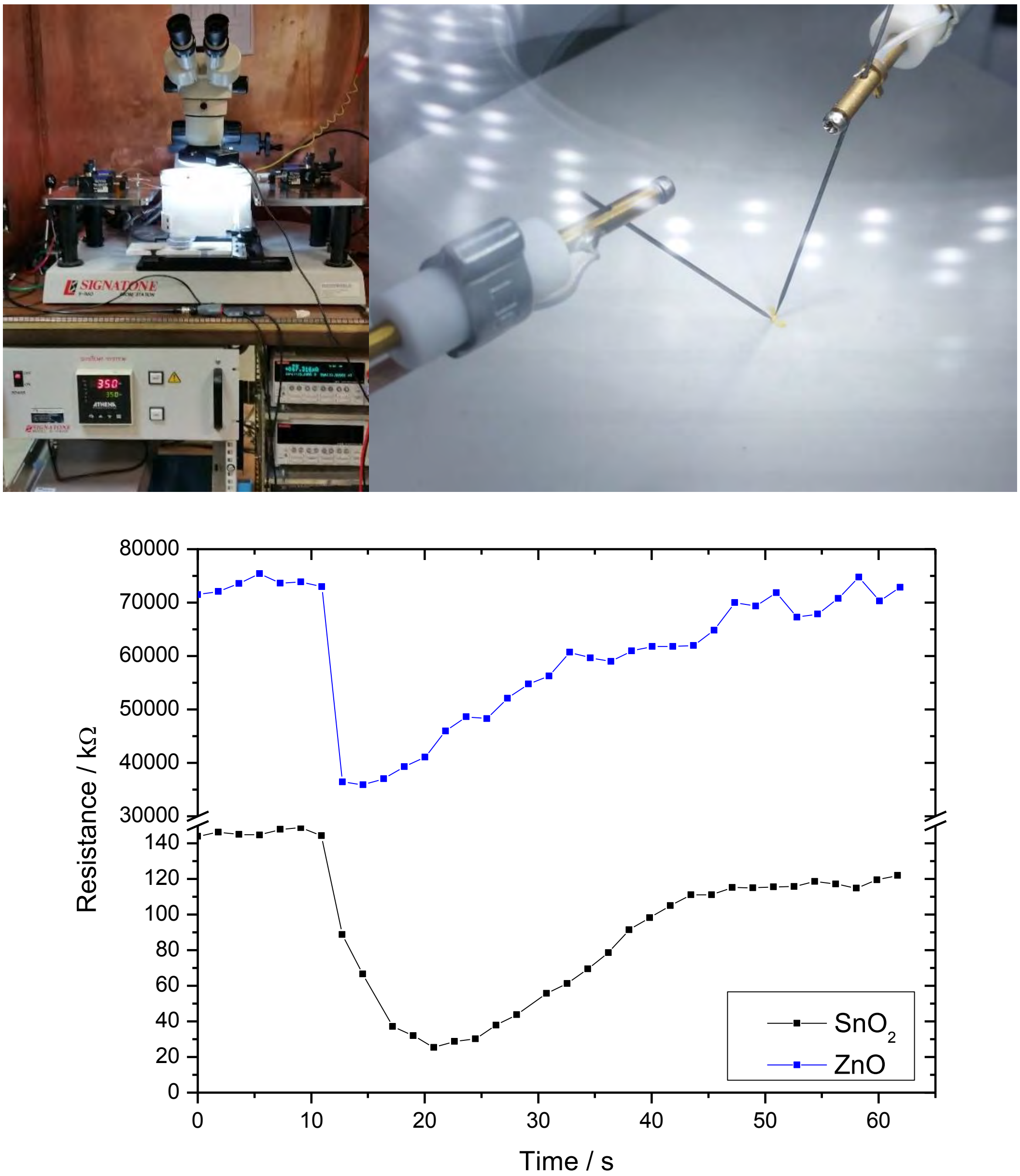

Figure IV.28 (Top) Picture of the two points probe and heating chuck used to measure the ethanol gas response of ZnO and SnO_2 wires. (Bottom) Typical response of the zinc oxide (chuck temperature ca 400°C) and tin oxide (chuck temperature ca 350°C) fibers.

Conclusion

The gathered results demonstrate an innovative approach based on processable organometallic gels that can be easily shaped (and reshaped) into complex 3D structures. These shapes are retained during the hydrolysis of the gel to yield hybrid organic-metal oxide nanoparticles material, and further after calcination where the pure metal oxide material is obtained. In the present study, zinc, tin and iron oxides have been obtained but considering the rich library of organometallic complexes, this original strategy can be extended to various metal oxides, including mixed metal oxides. This opens unprecedented opportunities to shape in a controlled fashion inorganic and hybrid materials.

References

[1] Nanoparticles: From Theory to Application. Ed.: Schmid G., Wiley Vch, **2006**.

[2] A. K. Ganguli, A. Ganguly, S. Vaidya, *Chem. Soc. Rev.* **2010**, *39*, 474.

[3] Z. Zhuang, Q. Peng, Y. Li, *Chem. Soc. Rev.* **2011**, *40*, 5492.

[4] M. R. Langille, M. L. Personick, C. A. Mirkin, *Angew. Chem. Int. Ed.* **2013**, *52*, 13910.

[5] H. Duan, D. Wang, Y. Li, *Chem. Soc. Rev.* **2015**, *44*, 5778.

[6] S. Diodati, P. Dolcet, M. Casarin, S. Gross, *Chem. Rev.* **2015**, *115*, 11449.

[7] C. Dhand, N. Dwivedi, X. J. Loh, A. N. Jie Ying, N. K. Verma, R. W. Beuerman, R. Lakshminarayanan, S. Ramakrishna, *RSC Adv.* **2015**, *5*, 105003.

[8] A. Feinle, M. S. Elsaesser, N. Husing, *Chem. Soc. Rev.* **2016**, *45*, 3377.

[9] D. Gu, F. Schuth, *Chem. Soc. Rev.* **2014**, *43*, 313.

[10] A. E. Danks, S. R. Hall, Z. Schnepp, *Mater. Horizon.* **2016**, *3*, 91.

[11] A. Carretero-Genevrier, G. L. Drisko, D. Grosso, C. Boissiere, C. Sanchez,

Nanoscale **2014**, *6*, 14025.

[12] S.-H. Wu, C.-Y. Mou, H.-P. Lin, *Chem. Soc. Rev.* **2013**, *42*, 3862.

[13] M. P. Pechini, Method of preparing lead and alkaline earth titanates and niobates and coating method using the same to form a capacitor. US patent US3330697 A, **1967**.

[14] M. L. Kahn, A. Glaria, C. Pages, M. Monge, L. Saint Macary, A. Maisonnat, B. Chaudret, *J. Mat. Chem.* **2009**, *19*, 4044.

[15] C. Amiens, B. Chaudret, D. Ciuculescu-Pradines, V. Colliere, K. Fajerwerg, P. Fau, M. Kahn, A. Maisonnat, K. Soulantica, K. Philippot, *New J. Chem.* **2013**, *37*, 3374.

[16] M. Monge, M. L. Kahn, A. Maisonnat, B. Chaudret, *Angew. Chem. Int. Ed.* **2003**, *42*, 5321.

[17] A. Ponton, S. Warlus, P. Griesmar, *J Colloid Interface Sci* **2002**, *249*, 209.

[18] Y. Tanaka, in *Rheology* (Ed.: J. De Vicente), InTech, **2012**.

[19] Z. Zheng, R. Butynska, C. V. Serrano, J.-D. Marty, C. Mingotaud, M. L. Kahn, *Chem. Eur. J.* **2016**, *22*, 15614.

[20] Y. Coppel, G. Spataro, C. Pagès, B. Chaudret, A. Maisonnat, M. L. Kahn, *Chem. Eur. J.* **2012**, *18*, 5384

[21] M. Westerhausen, T. Bollwein, A. Pfitzner, T. Nilges, H.-J. Deiseroth, *Inorg. Chim. Acta* **2001**, *312*, 239.

[22] S. D. Cosham, M. S. Hill, A. L. Johnson, K. C. Molloy, *Dalton Trans.* **2014**, *43*, 859.

[23] Z. Zheng, R. Butynska, C. V. Serrano, J.-D. Marty, C. Mingotaud, M. L. Kahn, *Chem. Eur. J.* **2016**, *22*, 15614.

[24] A. Nowacka, P. C. Mohr, J. Norrman, R. W. Martin, D. Topgaard, *Langmuir* **2010**, *26*, 16848.

[25] S. Grimme, *Wiley Interdisciplinary Reviews: Computational Molecular Science* **2011**, *1*, 211.

[26] A. D. Pajerski, G. L. BergStresser, M. Parvez, H. G. Richey, *J.Am. Chem. Soc.* **1988**, *110*, 4844.

[27] D. R. Armstrong, C. Dougan, D. V. Graham, E. Hevia, A. R. Kennedy,

Organometallics **2008**, *27*, 6063.

[28] N. A. Bell, H. M. M. Shearer, C. B. Spencer, *Acta Crystallographica Section C* **1983**, *39*, 1182.

[29] J. G. Noltes, J. Boersma, *J. Organomet. Chem.* **1969**, *16*, 345.

[30] G. E. Coates, D. Ridley, *J. Chem. Soc.* **1965**, 1870.

[31] M. L. Kahn, A. Glaria, C. Pages, M. Monge, L. Saint Macary, A. Maisonnat, B. Chaudret, *J. Mater. Chem.* **2009**, *19*, 4044.

[32] Z. H. Zhao, Z. Q. Zheng, C. Roux, C. Delmas, J. D. Marty, M. L. Kahn, C. Mingotaud, *Chem.-Eur. J.* **2016**, *22*, 12424.

Conclusion générale

____

Conclusions

Le domaine des nanosciences est un champ disciplinaire extraordinaire à l'interface entre différentes sciences. Il se nourrit de la convergence de plusieurs disciplines : chimie, physico-chimie, physique et biologie. Ce travail en est une modeste illustration.

A partir d'une approche de synthèse par voie organométallique de nanoparticules d'oxyde de zinc, nous avons dans un premier temps exploré les paramètres permettant le contrôle de la croissance anisotrope de ces objets. Nous avons ainsi mis en évidence le rôle important de la quantité d'eau qui est plus marquée que celle de la longueur de la chaine alkyl des ligands amine. Nous avons également développé une représentation bidimensionnelle permettant de visualiser très facilement des phénomènes de croissance et de mettre en exergue les corrélations éventuelles entre longueur et largeur dans des nanoparticules anisotropes. Cette approche a été développée à l'interface avec les statistiques et ouvre des perspectives que nous détaillerons dans la partie suivante.

Par ailleurs, nous avons mis en évidence une nouvelle chimie des précurseurs nous permettant d'accéder à des gels. Ces derniers peuvent être mis en forme pour créer des matériaux hybrides organique-inorganique malléables qui ouvrent des perspectives en science des matériaux. Ces hybrides mis en forme peuvent ensuite être calcinés et former des oxydes métalliques purs aux propriétés qu'il conviendra d'étudier plus en profondeur. Les travaux sur ces nouveaux matériaux sont en cours. En particulier, nous nous intéressons à leurs propriétés de détection, un des axes majeurs des activités développées dans l'équipe NOS. De manière plus globale, nos travaux centrés sur le ZnO ont néanmoins été étendus extrêmement facilement à d'autres systèmes métalliques. Même si seuls quelques essais sur l'étain et le fer ont été tentés avec succès, même si seuls quelques mises en forme de matériaux ont été développés, il est clair que les résultats trouvés sont très encourageants et ouvrent de nouvelles voies de recherche en science des matériaux.

Perspectives

Les perspectives à ce travail de thèse sont ainsi nombreuses. Elles concernent à la fois le traitement statistique des résultats expérimentaux obtenus lors de la synthèse de nano-objets, la chimie des précurseurs, les gels, les matériaux hybrides, la mise en forme d'oxydes métalliques et leur utilisation.

Il apparait de façon évidente qu'une grande masse de données a été produite par les chimistes depuis qu'ils développent des approches de synthèse pour une maitrise et un contrôle parfait des nanoparticules. La représentation bidimensionnelle que nous avons proposée devrait permettre de revisiter ces approches et de mieux appréhender les paramètres clé permettant la croissance anisotrope des objets. Il convient pour atteindre de but de fédérer autour de ce projet les compétences des chimistes et des statisticiens.

En ce qui concerne la chimie des précurseurs, nous avons montré que le choix des complexes organométalliques était important. En particulier il conviendra d'étudier plus en détail les modifications chimiques induites par les ligands introduits dans le milieu réactionnel avant la réaction d'hydrolyse. La formation de gels est un élément essentiel pour la mise en forme des matériaux et permet d'ouvrir de nouvelles perspectives à la chimie organométallique. En effet, de façon surprenante, la formation du gel ralenti significativement la réaction d'hydrolyse de l'oligomère organométallique. Il devient aisé de le manipuler à l'air, de le mettre en forme. Pourrons-nous obtenir des matériaux à porosité contrôlée par cette approche ? Une stratégie de type « template » couramment employée en chimie sol-gel pourrait-elle être ici développée ?

Nous avons ouvert la voie vers une nouvelle chimie de coordination des précurseurs organométalliques comme intermédiaires à la formation de matériaux hybrides. La mise en forme est également un domaine qu'il nous reste à étudier. Par exemple, nous avons montré que la mise en forme des matériaux hybrides organique-inorganique donnait lieu à des fibres de type cœur-coquille.

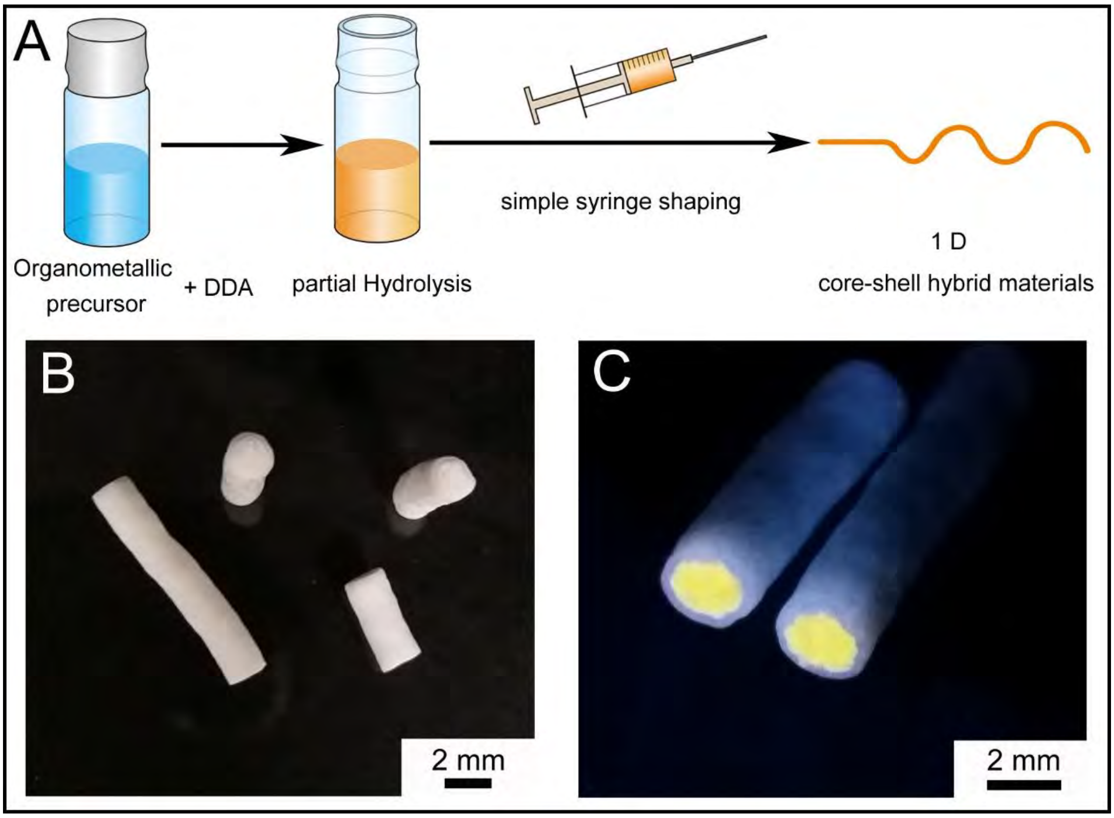

La nature du cœur est celle de l'oxyde métallique alors que celle de la coquille est uniquement organique comme l'illustre parfaitement la figure ci-dessous. Cette formation de fibre de type cœur-coquille est générale.

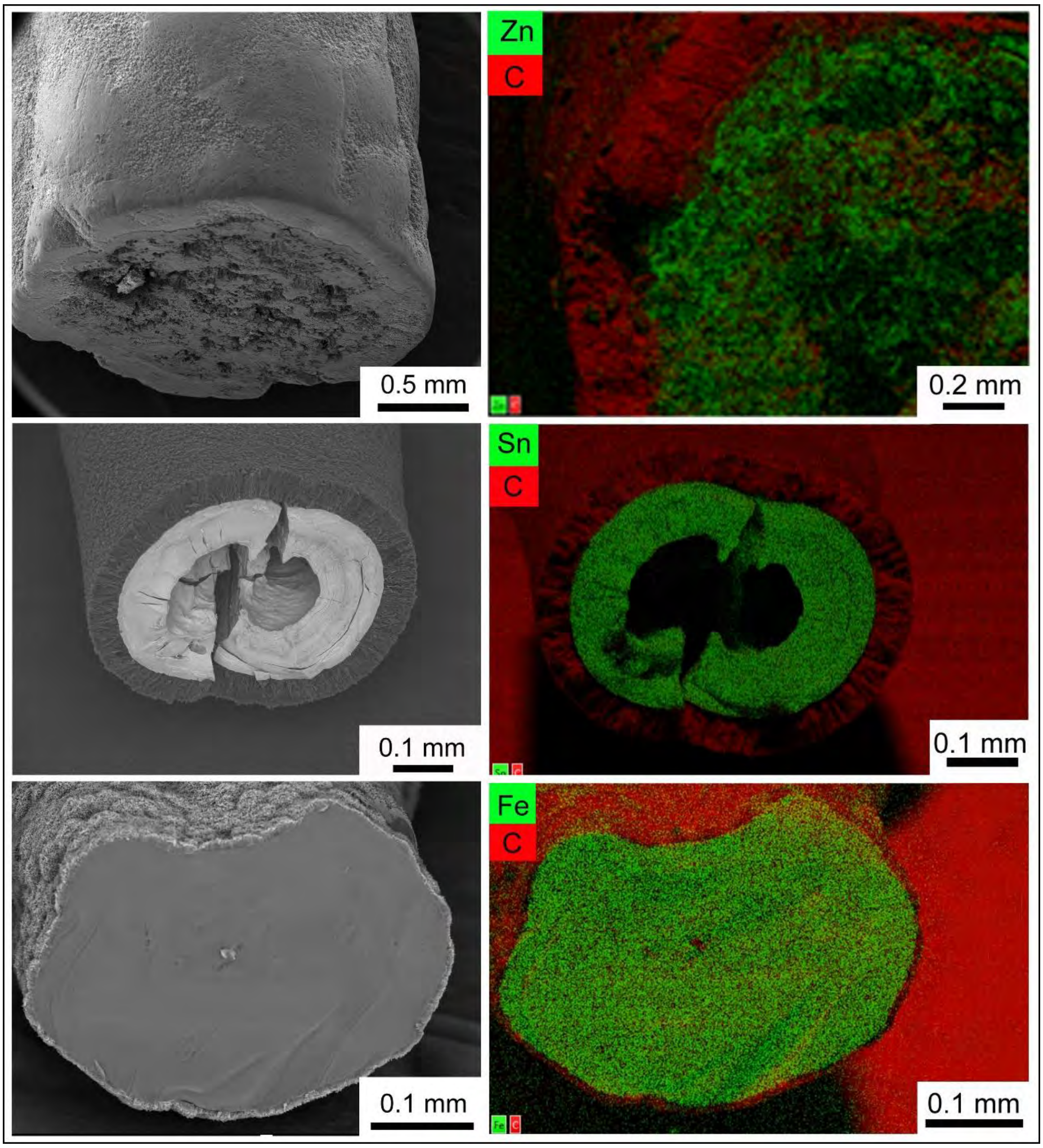

Il nous faut évidemment comprendre la formation de ces fibres de type cœur-coquille car juste après extrusion, les fibres n’ont pas cette structuration en cœur-coquille. Elles sont homogènes en composition organique-inorganique.

Après calcination, ces fibres sont très poreuses. Elles présentent des surfaces spécifiques de l’ordre de 50 $m^2.g^{-1}$. Les premiers essais que nous avons menés pour utiliser cette porosité montre des performances exceptionnelles de ces matériaux en tant que couches sensibles pour des capteurs de gaz. Les dispositifs sont très rapidement stables, ils présentent une forte variation de leur résistance en présence de différents gaz.

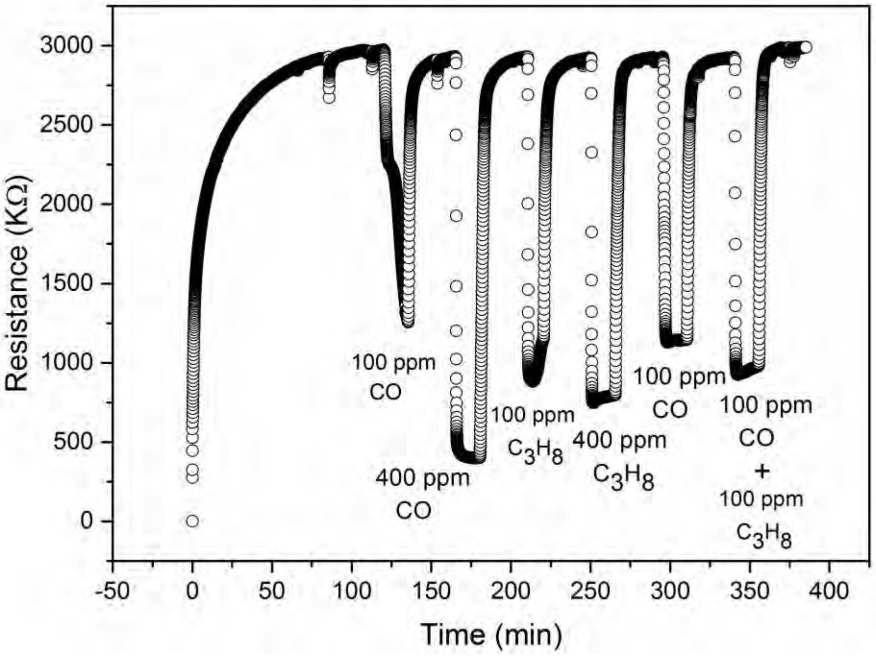

Néanmoins, nous n'avons pas eu suffisamment de temps pour mener à bien l'étude complète de ces propriétés en particulier car la connexion de ces fibres et/ou des pates aux dispositifs reste très délicate. Il faut donc encore améliorer cet aspect pour poursuivre l'étude de ces matériaux en tant que capteur de gaz.

Outre l'aspect matériau, clairement les études faites sur le zinc, un peu l'étain et le fer doivent être également étendus à d'autres métaux ainsi qu'à d'autres ligands. Un mélange de ligands peut-il contrôler la taille des oligomères et donc les propriétés mécaniques finales du système ? Celles-ci peuvent-elles être ajustées par la présence d'insaturation ou de branchement dans les chaînes alkyls ? Quel est l'influence d'un cisaillement sur ces gels ? L'ensemble de ces questions mérite d'être abordé dans les années qui viennent afin de toujours mieux contrôler cette nouvelle voie mise en évidence pour créer des matériaux hybrides à partir de précurseurs organométalliques.

Partie expérimentale

Contenu

Experimental Section

Introduction

In this section, detailed synthetic procedures used in this thesis will be presented. All the apparatus for characterization will be also explained. At last, the information of all the reagents used in this thesis will be listed.

Synthestic Procedures

Procedures for products listed below are represented according to their order of appearance in their respective chapters of this manuscript. All the metal precursors were purchased from NANOMEPS, and all the synthesis before hydrolysis were performed in an MBraun Inert Gas System.

Procedures: Chapter II

Figure II.4 gives the shape analysis of ZnO nanoparticles which were prepared through the following procedure: in the glove box, 92.7 mg of dodecylamine (DDA, 2 equivalents) was added in a small vial to 57.9 mg of zinc precursor [$Zn(C_6H_{11})_2$]. After complete mixing, the vial was taken out of the glove box and exposed to the air. After various reaction times, part of the sample was analyzed by TEM.

Procedures: Chapter III

Synthesis of ZnO NPs. All the above synthesis was performed at ambient temperature.

Study of ZnO NPs size as a function of hydrolysis time: In a glove box, 57.9 mg of [$ZnCy_2$] was added in a 4 mL glass vial to 92.7 mg of DDA. After complete mixing (the total time in the glove box is 10 minutes), the vial was taken out of the glove box and exposed to the air. TEM analysis were then performed at different reaction times.

Influence of gelation time on ZnO NPs size: 57.9 mg of [$ZnCy_2$] was mixed in a 4 mL glass vial to 92.7 mg of DDA. After complete mixing, the mixture was aged in the glove box. Samples were taken out of the glove box at different time and exposed to the air for 3 days.

Study of ZnO NPs size as a function of temperature: In the glove box into a 4 mL vial, 57.9 mg of [$ZnCy_2$] were added to 92.7 mg DDA. After complete mixing (the total time in the glove box is 10 minutes), vials were taken out, kept at the chosen temperature (30 °C, 60 °C, 90 °C, 120 °C in oil bath) and exposed to the air for 3 days.

Study of ZnO NPs size as a function of tubes length: 57.9 mg of [$ZnCy_2$] was added in a 4 mL glass vial with different length of PTFE tubes (from 0 to 7 cm) to 92.7 mg of DDA. After complete mixing (the total time in the glove box is 10 minutes), the vial was taken out of the glove box and exposed to the air for 1 week.

Study of ZnO NPs size as a function of water content: 57.9 mg of [$ZnCy_2$] was added in a 4 mL glass vial to 92.7 mg of DDA. After complete mixing (the total time in the glove box is 10 minutes), the vial was placed into a homemade reactor that allowed the slow diffusion of water into the sample. Different amount of degassed water was injected in the reactor. After 3 days white luminescent powders were obtained and analyzed by TEM.

Procedures: Chapter IV

Synthesis for the time dependent rheological property measurement: 1 equivalent of [ZnCy$_2$] (174 mg, 0.75 mmol) was added to 2 equivalents of DDA (278 mg, 1.5 mmol) in a 4 mL glass vial, a clear homogeneous solution was resulted after gentle shaking. It was then transferred to a 3 mL syringe with a stainless needle in a closed schlenk tube flushed with argon. The solution was injected in the plate of the rheometer for the measurement under a flow of nitrogen.

Shaping and reshaping process of ZnO hybrid materials:

1D: 1 equivalent of [ZnCy2] (115 mg, 0.5 mmol) was added to 2 equivalents of DDA (185 mg, 1 mmol) in a 4 mL glass vial, a clear colorless solution was formed after gentle shaking, then was transferred to a 3 mL syringe with a flat stainless needle (25G 0.5 × 16 mm), after aging in the glove box for 4.5 to 5 hours, continuous colorless 1D gelified fibers could be obtained by simple extrusion through a needle of a syringe. The fibers could be directly deposited on the silica membrane of the device. The final ZnO hybrid 1D material is obtained by the direct exposure of the colorless 1D gelified fibers to the air.

2D: The process is very similar as the one for the 1D process. 1 equivalent of [ZnCy$_2$] (115 mg, 0.5 mmol) was added to 2 equivalents of DDA (185 mg, 1 mmol) in a 4 mL glass vial, a clear colorless solution was formed after gentle shaking. After aging the solution for 4.5 to 5 hours in the glove box, several drops of the viscous solution was deposited on a glass substrate. A glass slide was then used to spread the droplets and homogeneously covered the glass substrate. A 3.0 x 3.0 cm stamp with “CNRS” pattern was used. The final ZnO hybrid 2D material is obtained by the direct exposure of the colorless 2D pattern to the air.

3D: The process is very similar as the one for the 1D process. 1 equivalent of [ZnCy$_2$] (115 mg, 0.5 mmol) was added to 2 equivalents of DDA (185 mg, 1 mmol) in a 4 mL glass vial, a clear colorless solution was formed after gentle shaking. The clear colorless solution was transferred to an Eiffel Tower mold. After aging in the glove box for 10 hours, a transparent solid with an Eiffel Tower shape was obtained after demolding. The final ZnO hybrid 3D material is obtained by the direct exposure of the colorless 3D object to the air.

Reshaping process: The prepared ZnO hybrid material was melted at 90°C and transferred to another mold, after cooling down, the hybrid materials was reshaped.

Shaping process of tin oxide hybrid materials: 1 equivalent of [Sn(NMe$_2$)$_2$]$_2$ (414 mg, 1 mmol) was added to 2 equivalents of DDA (371 mg, 2 mmol) in a 4 mL glass vial with a cap, a clear yellow solution was obtained after gentle shaking. Opening of the vial for 10 minutes leads to the formation of a highly viscous yellow compound. This latter was transferred to a 3 mL syringe with a flat stainless needle (21G 0.8 × 40 mm). Continuous yellow 1D gelified fibers could be obtained by simple extrusion through a needle of a syringe.

Shaping process of 1D iron oxide hybrid materials: 1 equivalent of [(Fe{N(SiMe$_3$)$_2$}$_2$)$_2$] (377 mg, 0.5 mmol) was added to 2 equivalents of DDA (186 mg, 1 mmol) in a 4 mL glass vial with a cap, a clear black solution was obtained after a gently shaking. After aging in the glove box for 6 days, the highly viscous black compound was transferred to a 3 mL syringe with a flat stainless needle (21G 0.8 × 40 mm). Continuous black gelified fibers could be obtained by simple extrusion through a needle of a syringe.

Sintering: The as-prepared fibers were calcined from room temperature to 350 °C (for Zn and Fe) and 450 °C (for Sn) at a rate of 1 °C/min, and kept at the target temperature for 6 hours.

Characterization Methods

Some characterization techniques were used so as to understand the physical or chemical properties of the prepared materials in this work. The details about the apparatus of those techniques will be shown below, and some programs about the software to analyze the size of nanoparticles will also be discussed.

Transmission Electron Microscopy (TEM): Samples for TEM studies were prepared by slow evaporation of droplets of THF solution deposited on carbon-coated copper grids. The samples were then carefully dried overnight under a pressure of 5.10^{-5} mbar with a BOC Edward turbomolecular pump. The TEM experiments were performed on a Hitachi 7700 transmission electron microscope operating at 120 kV with a resolution of 2.04 Å.

Field-emission scanning electron microscopy (FESEM): SEM images were obtained using an FEG FEI Quanta 250 microscope operating at 5 kV.

Differential scanning calorimetry (DSC): DSC experiments were performed by using a Mettler Toledo DSC1 STARe System thermal analysis calorimeter equipped with a gas controller GC200 and a HSS8 ceramic sensor. For the thermogram analysis, onsets of the various peaks were extracted at various scan speed and extrapolated at null speed.

Polarized optical microscopy (POM): Characterization of liquid crystalline phases was performed by using a laboratory made hot-stage under a polarized light optical microscope BX50 from Olympus.

Photoluminescent Spectra: Emission and excitation spectra were measured using a Horiba Jobin Yvon Fluoromax-4 spectrofluorometer equipped with a xenon lamp.

NMR spectroscopy: Liquid state 1D and 2D NMR experiments were recorded on a Bruker Avance 500 spectrometer equipped with a 5 mm triple-resonance inverse Z-gradient probe. All of the samples were prepared in Toluene-d8. 2D NOESY measurements were performed with a mixing time of 200 ms. All diffusion measurements were made by using the stimulated echo pulse sequence with bipolar gradient pulses.

Solid-state NMR experiments were recorded on a Bruker Avance III 400 spectrometer. Samples were packed into 4 mm zirconia rotors inside a glove box. The rotors were spun at 8 kHz at 293K. For 13C MAS with Direct-Polarization (DP), a small flip angle of 30° was used with a recycle delay of 10 s. 13C MAS with Cross-Polarization (CP) were recorded with a recycle delay of 2 s and a contact time of 2 ms. 13C MAS with Insensitive Nuclei Enhanced by Polarization Transfer (INEPT) were recorded with a recycle delay of 3 s.

All of the chemical shifts are relative to TMS.

WAXS experiments: WAXS measurements were performed on a dedicated two-axis diffractometer at molybdenum wavelength (0.071069 nm). Measurement time was 64h for a data set including 457 points equally spaced in reciprocal space. Pure sample was sealed inside a thin-walled glass capillary 1.5 mm in diameter. Intensity was corrected from absorption and polarization effects, reduced by subtraction of components independent of the structure, and then Fourier transformed. A data collection of 500 s/point was used to get data of good quality (see plot below):

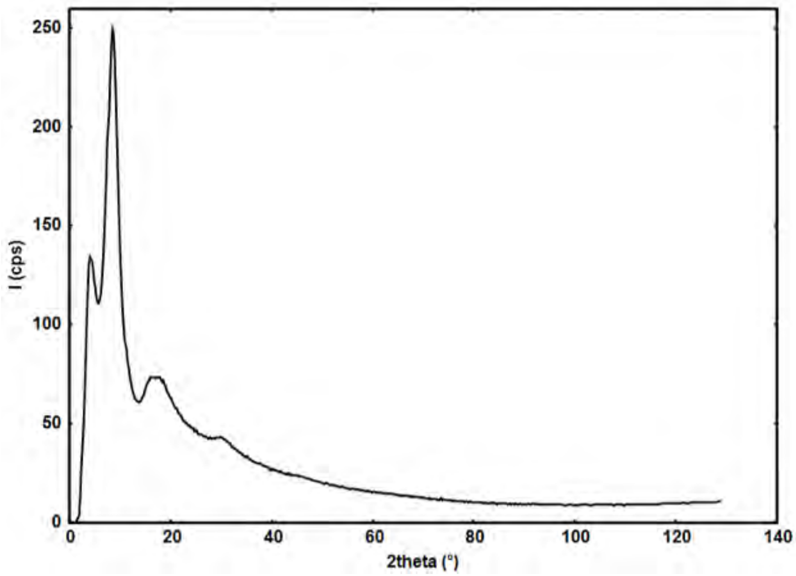

Scattering intensity of the Zinc organometallic gel before hydrolysis.

Conventional procedures for data reduction (i.e. reduced intensities) and Fourier Transform (i.e. Radial Distribution Function, RDF) were used.

X-ray diffraction: Powder X-ray diffraction (PXRD) measurements were conducted at room temperature on a SEIFERT XRD 300 TT diffractometer operated under Cu Kα radiation, fitted with a diffracted beam graphite monochromator. The data were collected between 5 and 80 θ with a 0.017 Å step and a 400 s per step counting time (200 s for tin oxide). Average crystallite size values (FWHM) were calculated by Debye–Scherrer formula with PANalytical HighScore Plus program.

Molecular simulation: Geometries were fully optimized at various levels of calculation using Gaussian09 [1]. Vibrational analysis was performed at the same level as the geometry optimization. Gibbs free energies were calculated at 298.15 K. Solvent effects of octylamine (ε=3.1) [2], were included using the polarizable continuum model (PCM) implemented in Gaussian09.

Rheological property measurement: The elastic modulus (G') and viscous modulus (G") were monitored with an AR1000 (TA Instrument). A flush of nitrogen (0.2 Bar) was provided within the oven during the entire experiment. The measurement was made with a 25 mm plate-plate aluminum geometry and the gap was set at 500 µm. An extra plastic cylinder is placed around the geometry to avoid drying of the sample due to the gas flow. The temperature was 23 °C.

Compressive test: The 1D material was cut straight to provide a series of small cylinders. The diameters were measured with a vernier caliper and were equal to ca 2.40 mm. The lengths varied between 3.50 and 4.50 mm. The cylinders were subjected to an uniaxial compression until breaking, from 0 to 1.5 mm at 1 mm/s, with a Bose Electroforce 3100 mechanical testing machine. From the corresponding curves, the slope at the origin enabled us to calculate the compressive Young Modulus (by dividing the slope by the cylinder surface and multiplying by the total length). The ultimate compressive strength was calculated from the maximum strength on the curves, before the material failed, divided by the section of the cylinder.

Photocurrent measurements: The silicon platforms employed in this study have been provided by Microchemical Systems SA (Neuchatel, Switzerland). The die (2.3×2.3 mm) comprises a 2 µm thick insulating layer (SiOxNy). A butterfly shape polysilicon heater is embedded between the lower insulating layer and a silicon dioxide passivation top layer. The back side of the silicon die is etched by KOH chemical bath in order to release the dielectric membrane for thermal insulation purpose. Top electrical contacts (Pt/Ti/Cr sandwich) for resistance measurement of the deposited fiber are deposited on the passivation layer. These electrical contacts are relayed by gold wires with the underneath legs of the chip.

Single ZnO fiber are directly deposited on the top of the die. The device was then exposed to the air for 3 days, and transferred to a tube furnace for calcination. The calcined fiber is electrically connected to the gold wire of the die by a silver epoxy paste. The photocurrent property of ZnO fiber is obtained by UV exposure by a 365 nm photo diode placed at ca. 2 mm of the die.

Gas sensor measurements: The response of ZnO and SnO_2 fibers to ethanol gas is obtained by the resistance variation of the fibers placed under a 4 wires measurement station. The fibers are heated in situ by a thermal chuck at 400 °C for ZnO and 350 °C for SnO_2. The ethanol gas flow directed to the fibers causes a resistance drop and a progressive return of the fiber resistance to the initial baseline resistance value.

2-D plot analysis: Image J software [3] was used manually or with a macro in order to extract width and length of nano-objects in various micrographs. The macro is based on the PSA macro, available at http://code.google.com/p/psa-macro. Overlapping nanoparticles are automatically rejected for the statistical analysis. The results were adjusted to account for the overestimation of particle size when fitting square or rectangular shapes with ellipses, according to Igathinathane et al [4]. The software leads to a table listing for each particle of two perpendicular dimensions D1 and D2. No ordering of these values is needed since this table is doubled by listing D2 as a function of D1. Plots of D1 as a function of D2 and D2 as a function of D1 are combined in the 2D size plot analyzed in this work.

R program: 2D plot presents point clouds whose structures can be the result of different sub-populations. In order to identify these sub-populations (usually called clusters in the field of mathematical analysis), a multivariate analysis has been performed with the mixmod software (http://mixmod.org) using R package [2]. Apart from the Gaussian character of the probability densities, no assumption about the orientation, shape and volume of the different sub-populations was made during calculation. The number of sub-populations that composed the point clouds was fixed by the user or chosen numerically thanks to the BIC criterion. Each sub-population was then characterized by the mean of the two studied variables (i.e. short and long axis lengths) as well as the corresponding standard deviations. Additionally, the correlation parameter ρ between both variables was calculated. The correlation is equal to zero when the two variables are totally independent and equal to 1 when they are affinely related to each other.

The software in R program using for multivariate analysis is shown below (next page):

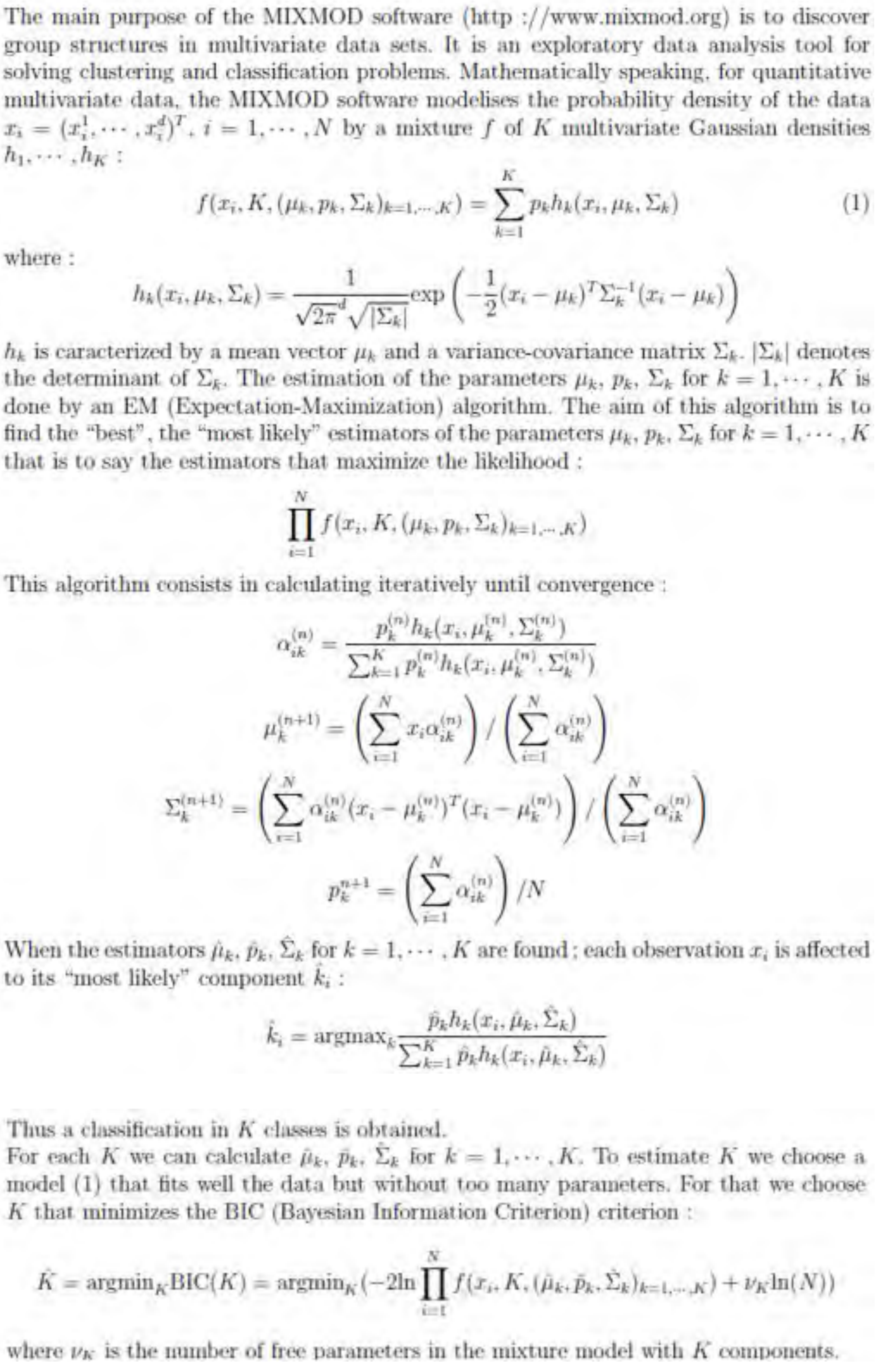

The main purpose of the MIXMOD software (http ://www.mixmod.org) is to discover group structures in multivariate data sets. It is an exploratory data analysis tool for solving clustering and classification problems. Mathematically speaking, for quantitative multivariate data, the MIXMOD software modelises the probability density of the data $x_i = (x_i^1, \cdots, x_i^d)^T$, $i = 1, \cdots, N$ by a mixture f of K multivariate Gaussian densities $h_1, \cdots, h_K$:

$$f(x_i, K, (\mu_k, p_k, \Sigma_k)_{k=1,\cdots,K}) = \sum_{k=1}^{K} p_k h_k(x_i, \mu_k, \Sigma_k) \qquad (1)$$

where :

$$h_k(x_i, \mu_k, \Sigma_k) = \frac{1}{\sqrt{2\pi}^d \sqrt{|\Sigma_k|}} \exp\left(-\frac{1}{2}(x_i - \mu_k)^T \Sigma_k^{-1} (x_i - \mu_k)\right)$$

h_k is caracterized by a mean vector μ_k and a variance-covariance matrix Σ_k. $|\Sigma_k|$ denotes the determinant of Σ_k. The estimation of the parameters μ_k, p_k, Σ_k for $k = 1, \cdots, K$ is done by an EM (Expectation-Maximization) algorithm. The aim of this algorithm is to find the "best", the "most likely" estimators of the parameters μ_k, p_k, Σ_k for $k = 1, \cdots, K$ that is to say the estimators that maximize the likelihood :

$$\prod_{i=1}^{N} f(x_i, K, (\mu_k, p_k, \Sigma_k)_{k=1,\cdots,K})$$

This algorithm consists in calculating iteratively until convergence :

$$\alpha_{ik}^{(n)} = \frac{p_k^{(n)} h_k(x_i, \mu_k^{(n)}, \Sigma_k^{(n)})}{\sum_{k=1}^{K} p_k^{(n)} h_k(x_i, \mu_k^{(n)}, \Sigma_k^{(n)})}$$

$$\mu_k^{(n+1)} = \left(\sum_{i=1}^{N} x_i \alpha_{ik}^{(n)}\right) / \left(\sum_{i=1}^{N} \alpha_{ik}^{(n)}\right)$$

$$\Sigma_k^{(n+1)} = \left(\sum_{i=1}^{N} \alpha_{ik}^{(n)} (x_i - \mu_k^{(n)})^T (x_i - \mu_k^{(n)})\right) / \left(\sum_{i=1}^{N} \alpha_{ik}^{(n)}\right)$$

$$p_k^{n+1} = \left(\sum_{i=1}^{N} \alpha_{ik}^{(n)}\right) / N$$

When the estimators $\hat{\mu}_k$, $\hat{p}_k$, $\hat{\Sigma}_k$ for $k = 1, \cdots, K$ are found ; each observation x_i is affected to its "most likely" component $\hat{k}_i$:

$$\hat{k}_i = \text{argmax}_k \frac{\hat{p}_k h_k(x_i, \hat{\mu}_k, \hat{\Sigma}_k)}{\sum_{k=1}^{K} \hat{p}_k h_k(x_i, \hat{\mu}_k, \hat{\Sigma}_k)}$$

Thus a classification in K classes is obtained.
For each K we can calculate $\hat{\mu}_k$, $\hat{p}_k$, $\hat{\Sigma}_k$ for $k = 1, \cdots, K$. To estimate K we choose a model (1) that fits well the data but without too many parameters. For that we choose K that minimizes the BIC (Bayesian Information Criterion) criterion :

$$\hat{K} = \text{argmin}_K \text{BIC}(K) = \text{argmin}_K \left(-2\ln \prod_{i=1}^{N} f(x_i, K, (\hat{\mu}_k, \hat{p}_k, \hat{\Sigma}_k)_{k=1,\cdots,K}) + \nu_K \ln(N)\right)$$

where ν_K is the number of free parameters in the mixture model with K components.

Statistical indices

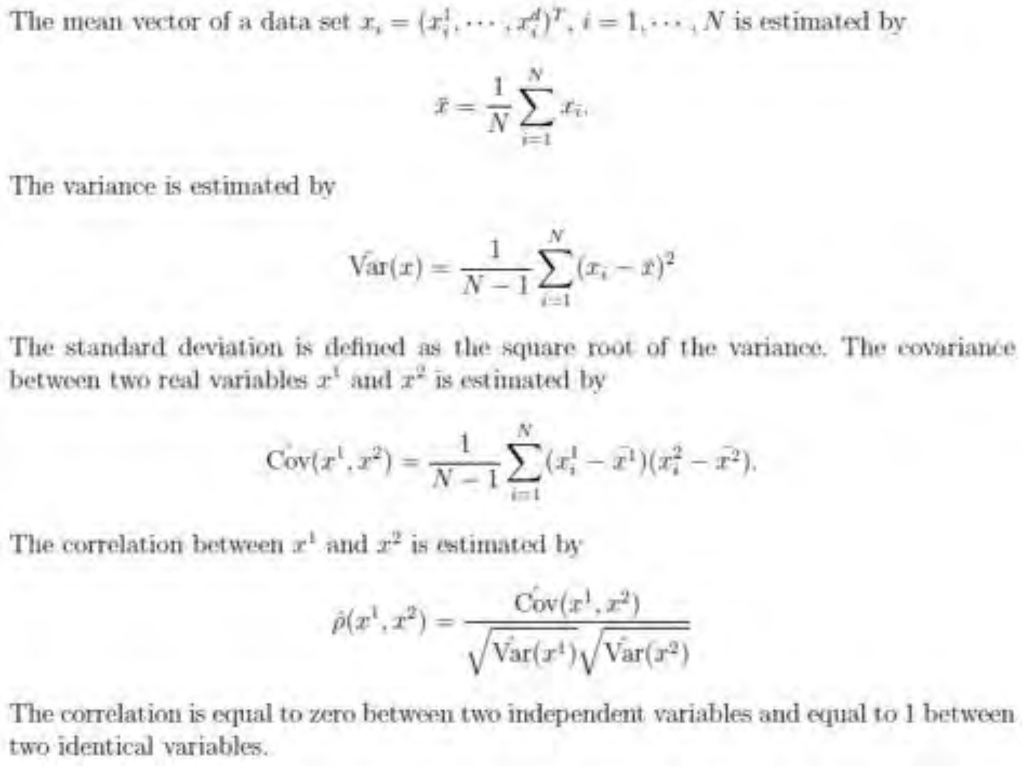

The mean vector of a data set $x_i = (x_i^1, \cdots, x_i^d)^T$, $i = 1, \cdots, N$ is estimated by

$$\bar{x} = \frac{1}{N}\sum_{i=1}^{N} x_i.$$

The variance is estimated by

$$\hat{\mathrm{Var}}(x) = \frac{1}{N-1}\sum_{i=1}^{N}(x_i - \bar{x})^2$$

The standard deviation is defined as the square root of the variance. The covariance between two real variables x^1 and x^2 is estimated by

$$\hat{\mathrm{Cov}}(x^1, x^2) = \frac{1}{N-1}\sum_{i=1}^{N}(x_i^1 - \bar{x}^1)(x_i^2 - \bar{x}^2).$$

The correlation between x^1 and x^2 is estimated by

$$\hat{\rho}(x^1, x^2) = \frac{\hat{\mathrm{Cov}}(x^1, x^2)}{\sqrt{\hat{\mathrm{Var}}(x^1)}\sqrt{\hat{\mathrm{Var}}(x^2)}}$$

The correlation is equal to zero between two independent variables and equal to 1 between two identical variables.

Modified mixmod software

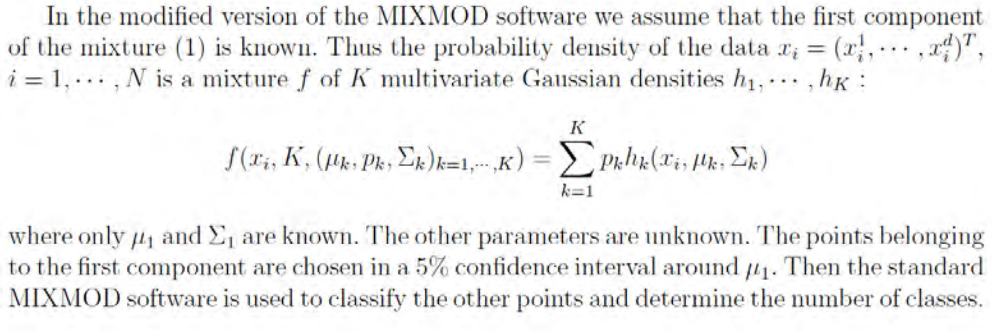

In the modified version of the MIXMOD software we assume that the first component of the mixture (1) is known. Thus the probability density of the data $x_i = (x_i^1, \cdots, x_i^d)^T$, $i = 1, \cdots, N$ is a mixture f of K multivariate Gaussian densities $h_1, \cdots, h_K$:

$$f(x_i, K, (\mu_k, p_k, \Sigma_k)_{k=1,\cdots,K}) = \sum_{k=1}^{K} p_k h_k(x_i, \mu_k, \Sigma_k)$$

where only μ_1 and Σ_1 are known. The other parameters are unknown. The points belonging to the first component are chosen in a 5% confidence interval around μ_1. Then the standard MIXMOD software is used to classify the other points and determine the number of classes.

Details about reagents

All the reagents used in this work are commercially available, were stored at -20°C in the glove box and used without any further purifications. The CAS chemical abstracts service registry numbers, molar mass (g.mol^{-1}) and supplier of those compounds are listed below.

Reagent	CAS number	Molar mass ($g.mol^{-1}$)	Supplier
Dicyclohexyl zinc [$ZnCy_2$]	15658-08-9	231.7	NanoMEPS
Bis(dimethylamido) tin [$Sn(NMe_2)_2]_2$	-	413.7	NanoMEPS
Bis(bistrimethylsilylamido) iron $\{Fe[N(SiMe_3)_2]_2\}_2$	-	753.2	NanoMEPS
Octylamine $CH_3(CH_2)_7NH_2$	111-86-4	129.24	Sigma-Aldrich
Dodecylamine $CH_3(CH_2)_{11}NH_2$	124-22-1	185.35	Sigma-Aldrich
Butylamine $CH_3(CH_2)_3NH_2$	109-73-9	73.14	Sigma-Aldrich
1-Adamantyl amine $C_{10}H_{17}N$	768-94-5	151.25	Sigma-Aldrich

References

[1] Gaussian 09, Revision D.01 (Gaussian, Inc., 2009).

[2] Chassaing, P. M. et al. Surface optical phonons as a probe of organic ligands on ZnO nanoparticles: An investigation using a dielectric continuum model and Raman spectrometry. Physical Review B 77, 153306 (2008).

[3] http://imagej.nih.gov/ij/; (b) Wojcik, P. J. Video tutorial: "How to measure nanoparticle size distribution using SEM pic". http://www.youtube.com/watch?v=D5KL40CFXqA.

[4] Igathinathane, C.; Pordesimo, L. O.; Columbus, E. P.; Batchelor, W. D.; Methuku, S. R., Shape identification and particles size distribution from basic shape parameters using ImageJ. Computers and Electronics in Agriculture 2008, 63 (2), 168-182.

Abstract

This work is focused on the better understanding of the formation of zinc oxide anisotropic nanoparticle through an organometallic synthesis. To start on this project, the development of a statistical tool to analyze nanoparticle sizes and shapes was mandatory. A simple 2D plot with a multivariate statistical analysis is proposed in order to extract, in particular, the correlation between length and width in a collection or a mixture of anisotropic particles. Compared to the usual statistics on the length associated to a second and independent statistical analysis of the width, this simple plot easily points out the various types of nanoparticles and their (an)isotropy. For each class of nano-objects, the relationship between width and length (i.e. the strong or weak correlations between these two parameters) may suggest information concerning the nucleation-growth processes. It allows one to follow the effect on the shape and size distribution of physical or chemical processes such as simple ripening. Various electronic microscopy pictures from the literature or from our own syntheses are used as examples to demonstrate the efficiency and simplicity of such an analysis.

Furthermore, following the organometallic approach, well defined crystalline zinc oxide nanorods are obtained through the hydrolysis reaction of dicyclohexyl zinc precursor without solvent in presence of primary fatty amine only. Their mechanism of formation is studied through a multivariate analysis of TEM results and an oriented attachment process is demonstrated. Taking advantage of this mechanism, the size of the ZnO nanorods can be easily adjusted tuned by controlling adjusting the hydrolysis rate, the aging time before hydrolysis, the nature of ligand, and/or the amount of water. During such experiments, a gelification of the chemical media are for the first time observed. This is the origin of the last part of our work, which put forward an original approach for outstanding processable and reshapable hybrid materials.

Indeed, we unequivocally demonstrate through various complementary experiments (rheology, NMR, TEM, theoretical calculation, WAXS…) the formation of oligomeric structures in a mixture of fatty amine with organometallic compounds. This oligomerization reaction between the metallic centers induces the formation of a gel

which can be processed into fibers, stamped patterns or molded pieces. Metal oxide hybrid materials are obtained merely by hydrolysis of the organometallic gel, which are furthermore liquid crystal. This unprecedented route towards easily processable hydrid and metal oxide materials is demonstrated for zinc oxide and extended to other metal oxides such as tin oxide and iron oxide, proving the universality of the method and paving the way, for example, to new sensitive gas sensors layers.

Résumé

Ce travail de thèse porte sur une meilleure compréhension de la croissance de nanoparticules d'oxyde de zinc élaborées à partir d'une approche organométallique. Au cours de ce travail, une analyse de la taille des nanoparticules en utilisant un outil simple basée sur une représentation bidimentionnelle couplée à une analyse statistique multivariée. Elle permet d'‘extraire la corrélation éventuelle entre la longueur et la largeur des nanoparticules. Cette approche permet de traiter un ensemble de nanoparticules homogène ou hétérogène en taille et en forme. Comparée à l'approche statistique usuelle qui analyse individuellement la distribution de la longueur et celle de la largeur, notre démarche met très facilement en évidence les différents types de nanoparticule et leur anisotropie (ou non). Pour chaque classe de nano-objets considérée, la relation entre la longueur et la largeur, c'est-à-dire les corrélations fortes ou faible entre ces deux paramètres, fourni des informations concernant le(s) mécanisme(s) de nucléation-croissance des nanoparticules. Par exemple, cette approche permet de suivre l'effet sur la taille et la forme de nanoparticules préparées par différents procédés (chimiques ou physique). A partir de différentes images de microscopie électronique extraites de la bibliographie ou de nos travaux de recherche, nous avons démontré l'efficacité et la simplicité de cette approche.

De plus, nous avons pu revisiter la synthèse organométallique de nanoparticules de ZnO à la lumière de cette nouvelle méthode de traitement des données. Les nanoparticules anisotropes obtenues par hydrolyse du dicyclohexyl zinc comme précurseur organométallique en présence d'alkyl amine uniquement ont donc été analysées. Le mécanisme de formation a été étudié par analyse systématique des images de microscopie électroniques à transmission et une croissance par attachement orienté a pu être mise en évidence. De plus, nous avons montré que la taille des nanabatonnets d'oxyde de zinc peut être facilement contrôlée en modulant la vitesse d'hydrolyse, le temps de maturation du mélange précurseur organométallique et ligand alkyl amine avant le début de l'hydrolyse, la nature du ligand et la quantité d'eau introduite. Enfin, pendant ce travail, nous avons observé la gélification des milieux réactionnels. L'étude

de ce phénomène a permis de développer une approche originale permettant de mettre en forme des matériaux hybride organique-inorganiques.

En effet, à partir d'un ensemble d'expériences utilisant la rhéologie, la RMN, la MET, des calculs théoriques, le WAXS … nous avons pu mettre en évidence une réaction d'oligomérisation entre le précurseur organométallique et les ligands alkyl amine. Cette oligomérisation entre les centres métalliques conduit à la formation de gels, qui peuvent être mise en forme en utilisant des seringues, des tampons ou encore des moules. Des matériaux hybrides d'oxydes métalliques sont ensuite obtenus par hydrolyse du gel. Cette nouvelle approche a été développée pour l'oxyde de zinc puis a été étendue aux oxydes d'étain et de fer. Il s'agit donc d'une approche générale qui ouvre des perspectives intéressantes dans l'utilisation de ces matériaux notamment comme couches sensibles pour des capteurs de gaz.